



**FRIEDRICH-SCHILLER-
UNIVERSITÄT
JENA**

**Characterization of laser-driven
proton acceleration with
contrast-enhanced laser pulses**

DISSERTATION
zur Erlangung des akademischen Grades
DOCTOR RERUM NATURALIUM (DR. RER. NAT.)

Vorgelegt dem Rat der
PHYSIKALISCH-ASTRONOMISCHEN FAKULTÄT
FRIEDRICH-SCHILLER-UNIVERSITÄT JENA

von **Georg Alexander Becker**
geboren am 04.09.1987 in Marburg (Lahn)

Gutachter:

1. Prof. Dr. Malte C. Kaluza
Institut für Optik und Quantenelektronik
Friedrich-Schiller-Universität, Jena
2. Priv.-Doz. Dr. Paul Neumayer
GSI Helmholtzzentrum für Schwerionenforschung GmbH, Darmstadt
3. Univ.-Doz. Dr. Matthias Schnürer
Max-Born-Institut, Berlin

Tag der Disputation: 08.07.2021

Abstract

In this thesis, various novel aspects of laser-driven ion acceleration with contrast-enhanced laser pulses have been characterized.

The maximum ion energies' dependence on the pulse energy and the foil thickness was investigated in a campaign at the POLARIS laser using a plasma mirror for contrast enhancement. The steepest increase of the ion energies depending on the pulse energy was measured for a 5 nm thin foil and linear polarization. Above a certain pulse energy, the onset of the foil's transparency correlated with a stop of the ion energies' increase. Consequently, additional enhancements of the temporal intensity contrast (TIC) and higher laser pulse intensities are required to exploit ion acceleration with such thin foils.

The ring-like beam profile formed by protons with low kinetic energy, which originated from submicron thick plastic foils, was characterized. Simulations support the explanation that such structures are a consequence of the proton density's spatial distribution during the acceleration with the target normal sheath acceleration mechanism (TNSA). These findings deepen the understanding of ion acceleration with thin foils and may help to distinguish features of other acceleration mechanisms in the beam profile from those attributed to TNSA.

In an experiment with water microdroplets, the effects of the laser's TIC and the incidence angle in the polarization plane were investigated. It was found that both parameters have a significant influence on the kinetic energy of the accelerated protons. An optical probe laser was used to observe the plasma expansion on a picosecond timescale. A correlation between the expansion and the maximum proton energy was found. The proton beam profile exhibited a reproducible net-like pattern depending on the irradiation geometry as well. The results show that the use of microdroplets irradiated with frequency-doubled laser pulses and optically probed gives new insights into laser-plasma interaction.

Zusammenfassung

In Rahmen dieser Dissertation wurden verschiedene neue Aspekte der lasergetriebenen Ionenbeschleunigung mit kontrastverbesserten Laserpulsen charakterisiert.

Die Abhängigkeit der maximalen Ionenenergien von der Pulsenergie und der Foliendicke wurde in einem Experiment am POLARIS-Laser untersucht, dessen Kontrast mit einem Plasmaspiegel verbessert wurde. Der stärkste Anstieg der Ionenenergien mit der Pulsenergie wurde für eine 5 nm dünne Folie und lineare Polarisierung gemessen. Oberhalb einer bestimmten Pulsenergie stoppte dieser Anstieg, was mit der einsetzenden Folientransparenz zusammenfiel. Dies macht weitere Verbesserungen des zeitlichen Intensitätskontrastes (TIC) bei gleichzeitiger Erhöhung der Laserintensität notwendig, um effektiv Ionen mit solchen dünnen Folien zu beschleunigen. Außerdem wurde das ringförmige Strahlprofil untersucht, welches von Protonen mit niedriger Energie gebildet wird, die von submikrometer dünnen Folien beschleunigt werden. Wie Simulationen nahelegen, bilden sich solche Strukturen bei der Beschleunigung mit dem Target Normal Sheath Mechanismus (TNSA) als eine Folge der Form der Protonendichteverteilung. Diese Erkenntnisse vertiefen das Verständnis über die Ionenbeschleunigung mit dünnen Folien und können dabei helfen Merkmale anderer Beschleunigungsmechanismen von denen des TNSA-Mechanismus zu unterscheiden.

In einem Experiment mit Wasser-Mikrotropfen wurden die Einflüsse des TIC und der Einfallsgometrie des Lasers in der Polarisierungsebene untersucht. Es hat sich gezeigt, dass beide Parameter einen großen Effekt auf die Energie der beschleunigten Protonen haben. Mithilfe eines optischen Lasers wurde die Plasmaexpansion auf einer Pikosekundenzeitskala beobachtet. Hier wurde eine Korrelation zwischen Expansion und maximaler Protonenenergie festgestellt. Das Strahlprofil der Protonen zeigte ein reproduzierbares, netzartiges Muster, welches ebenfalls von der Einfallsgometrie abhängt. Die Resultate zeigen, dass sich mit Mikrotropfen als Targets für frequenzverdoppelte Laserpulse und optischer Beobachtung neue Erkenntnisse über die Laser-Plasma Interaktion gewinnen lassen.

Contents

1. Introduction	3
2. Basics	6
2.1. Ionization of matter	6
2.2. Interaction of the laser field with a single electron	8
2.2.1. The ponderomotive force	11
2.3. Laser-plasma interaction	13
2.3.1. Plasma properties	13
2.3.2. Laser absorption and electron heating	15
2.4. Laser-driven ion acceleration	19
2.4.1. Target normal sheath acceleration	20
2.4.2. Ion acceleration with thin foils	28
2.4.3. Radiation pressure acceleration	29
2.5. Particle-in-cell simulations	33
3. Ion acceleration with thin foils	37
3.1. Ion diagnostics	37
3.1.1. The Thomson parabola spectrometer	38
3.1.2. Measurement of the proton beam profile	41
3.2. Experimental setups	42
3.2.1. Setup with plasma mirror	42
3.2.2. Setup with frequency-doubled laser pulses	46
3.3. Ion acceleration with nanometer thin foils	47
3.3.1. Results	48
3.4. Ring-like proton beam profile	57
3.4.1. Experimental results	59
3.4.2. Simulations and interpretation	61
3.5. Summary and discussion	68

4. Ion acceleration with water microdroplets	70
4.1. Experimental setup	71
4.2. Plasma expansion	73
4.3. Influence of target position and pre-plasma formation on proton acceleration	77
4.4. Simulations and interpretation	83
4.5. The proton beam profile	89
4.5.1. Experimental results	89
4.6. Summary and discussion	97
5. Summary	99
A. Appendix	101
A.1. The JETI 40 laser system	101
A.1.1. The optical probe laser	102
A.2. The POLARIS laser system	103
A.3. Estimation of the proton number detected with the TP in the water droplet experiment	105
References	107
Publications	129
Danksagung	132
Ehrenwörtliche Erklärung	133

1. Introduction

Different measurements of protons with kinetic energies in the tens of megaelectronvolts range (MeV) around the turn of the millennium have raised scientific interest in laser-driven ion acceleration [1–4]. These proton beams were generated by focusing high-power laser pulses onto micrometer-thick foils, reaching intensities well above 10^{19} W/cm² in the focal spot. Achieving these high intensities became only possible with the invention of the chirped pulse amplification (CPA) scheme for lasers [5] (Nobel Prize in 2018). Matter irradiated by such laser pulses is rapidly ionized and electrons exposed to the laser field reach velocities close to the speed of light. Due to the much higher mass of ions, an intensity exceeding 10^{24} W/cm² would be necessary to accelerate them directly to relativistic speeds. Since the highest intensity achieved so far is about $5.5 \cdot 10^{22}$ W/cm² [6, 7], laser-driven ion acceleration to MeV energies must therefore be an indirect process. The fundamental physics underlying most experimental and theoretical work is based on the target normal sheath acceleration (TNSA) mechanism [8]. TNSA works in principle as follows. A laser is focused usually onto a solid-state target, e.g., a foil, thus creating a plasma. Electrons from this plasma are accelerated through the foil and form an electron sheath beyond the foil’s rear surface. As a result, an electric field with a strength in the order of TV/m arises between the positively charged foil and the electrons. This field ionizes atoms from the target’s rear side and subsequently accelerates the generated ions, while protons are accelerated most efficiently due to their highest charge to mass ratio. The energy spectrum of the protons is usually thermal exhibiting a distinct cut-off. Depending on the experimental parameters, more than 10^{12} – 10^{13} protons can be accelerated [2, 9]. Other properties of the proton beam are a duration close to the source in the range of a few picoseconds [10], an energy-dependent source size from a few tens to well over a hundred micrometers, and an energy-dependent divergence [11, 12]. Motivated by these characteristics, numerous experimental and theoretical investigations have been carried out in this field [13, 14].

One main goal of this research is the realization of laser-driven ion sources as a com-

compact part of multi-purpose high-intensity laser facilities for various applications as a complement to conventional accelerator facilities. In contrast to the field strengths of TV/m that can be realized in a plasma, the electric field on the surface of highly polished stainless steel electrodes is limited to a strength of about 10 MV/m since electrons are emitted and accelerated from the surface for higher field strengths [15]. Thus, conventional particle accelerators are usually large structures whose size scales with the energy of the accelerated ions.

Currently available laser-driven proton sources have been successfully tested for stress testing of materials [16], the analysis of cultural heritage [17], as a source of crystal synthesis [18], for bi-modal imaging (with x-rays) of small biological or technical objects [19], or to probe electromagnetic fields [20, 21]. It was also possible to use laser-accelerated protons or deuterons to generate neutron pulses [22, 23] or accelerated protons to create warm dense matter [24, 25].

Laser-accelerated protons, or heavier ions, are also under consideration for fast ignition in fusion science [26, 27]. Another sophisticated and possible future application, proposed shortly after the emergence of the research field, is cancer therapy with laser-accelerated protons [28, 29]. In vitro irradiations of biological samples have already been performed [30–32], and there are efforts to realize treatments with laser-accelerated protons [33–35]. Special beam gantries are designed to optimize the properties of laser-driven proton sources for such treatments and other applications [36, 37]. Parts of a proton beam have already been (re-)compressed and focused using conventional accelerator technology [38–41]. However, protons with kinetic energies between 70 MeV and 250 MeV are necessary for tumor treatment (depending on the tumor's location), whereas the highest measured kinetic energy of laser-accelerated protons is around 100 MeV [42]. Besides, laser-driven proton beams lack the stability, and the control over the output parameters necessary for such sophisticated applications has not yet been reached. Consequently, fundamental research is needed to increase the depth of understanding of the physics involved in the acceleration process, with the long-term goal of improving control over laser-driven proton sources. To this end, various aspects of laser-driven ion acceleration have been investigated in the context of this thesis.

It was investigated whether higher maximum ion energies can be achieved with nanometer-thin foils in the context of radiation pressure acceleration (RPA) [43, 44]. Promising experimental results have been obtained with Ti:sapphire laser systems [45–48], which provided pulse durations of 30 fs or 45 fs. Such an investigation was

not yet performed with a laser system delivering pulses with a duration longer than 100 fs [49, 50] but much shorter than pulses from typical flashlamp-pumped laser systems [51, 52] (see Fig. 9 in [53]). In an experimental campaign at the POLARIS laser system employing a plasma mirror (PM) [54], the foil thickness could be decreased from 500 nm down to 5 nm for linearly and circularly polarized laser pulses to investigate the transition from TNSA dominated acceleration to thicknesses, for which RPA is expected to become relevant (see Secs. 3.2.1 and 3.3).

In addition to the measurement of the ion energies, the investigation of the proton beam's spatial profile is essential since this allows to deepen the understanding of the acceleration process and is also relevant for the subsequent transport of the accelerated protons to applications. In the context of this thesis, submicron thin foils were irradiated with frequency-doubled laser pulses, and the spatial distribution of the protons accelerated with the TNSA mechanism was characterized [55] (see Secs. 3.2.2 and 3.4).

Experimental statistics and many potential applications would benefit from increasing the repetition rate of laser-driven proton sources. This repetition rate depends on the minimum possible time between two consecutive laser pulses and the time required to replace an irradiated and thus destroyed target. The realization of a high replacement rate for thin foils is a sophisticated and expensive task, whereas the fastest demonstrated rate is 0.5 Hz [56]. Besides, after the prepared number of targets has been shot, the target holder needs to be restocked. This procedure takes time and includes letting up and pumping down the target chamber. Additionally, a foil's lateral extension allows electrons to leave the interaction region along the foil's surface [57]. This may reduce the electric field responsible for proton acceleration. Therefore, targets with a limited spatial extent that can be delivered at low cost, arbitrary numbers, and high repetition rate are highly desirable. A type of target fulfilling these conditions are liquid droplets with micrometer diameters. In the course of this thesis, proton acceleration from such microdroplets has been studied for different irradiation geometries, and the effect of an optional pre-pulse was investigated [58]. A synchronized optical probe was used to observe the plasma expansion [59–61], and complementary measurements of the proton beam profile were performed. These results are presented in Chapter 4.

This thesis starts in Chapter 2 with the basics of laser-plasma interaction and ion acceleration, while in Sec. 3.1 the used ion diagnostics are described. After the results (Chapters 3 and 4) the thesis closes with a short summary (Chapter 5).

2. Basics

This chapter describes the basics of the interaction of high-intensity laser pulses with plasmas and introduces the principles of laser-driven ion acceleration. Plasma is generally ionized matter whose components interact with and through electromagnetic fields. Firstly, the processes leading to the generation of plasmas, namely ionization processes, will be introduced. Then, the interaction of the laser fields with a single electron will be discussed, followed by the optical properties of a plasma as well as the transfer of laser energy to plasma electrons. Subsequently, the physical principles leading to the acceleration of ions will be described, and various acceleration mechanisms and models are presented. Finally, this chapter ends with a short explanation of the principles of particle-in-cell (PIC) simulations that were used to interpret the experimental results presented within this thesis.

2.1. Ionization of matter

Before ions can be accelerated as a consequence of the interaction of a laser pulse with matter, a plasma has to be generated via ionization of this matter. Atoms can absorb photons from an incident light wave via different processes, which can lead to the emission of an electron, which was initially bound to this atom. The atom's absorption of a single photon leading to the emission of an electron is called the photoelectric effect. When a photon's energy $E_{\text{ph}} = h\nu_{\text{L}} = hc/\lambda_{\text{L}}$ is equal to or higher than the material dependent ionization energy E_{ion} , the electron can leave the atom where the difference of photon and ionization energy is carried away by the electron as kinetic energy. Here, h is Planck's constant. ν_{L} and λ_{L} are the laser's frequency and wavelength, respectively. c is the speed of light in vacuum.

In the experiments presented in this thesis, water droplets, plastic foils, and diamond-like-carbon foils (DLC) were used as targets to study laser-driven ion acceleration. The ionization energies of the most weakly bound electrons from atoms of

these materials are $E_{\text{ion,H}^+} = 13.6 \text{ eV}$ (hydrogen), $E_{\text{ion,O}^+} = 13.6 \text{ eV}$ (oxygen), and $E_{\text{ion,C}^+} = 11.3 \text{ eV}$ (carbon). For the most strongly bound electrons the ionization energies are $E_{\text{ion,O}^{8+}} = 871 \text{ eV}$ and $E_{\text{ion,C}^{6+}} = 490 \text{ eV}$ [62].

The lasers used in these experiments have wavelengths of $\lambda_L = 0.4 \mu\text{m}$ and $\lambda_L = 1.0 \mu\text{m}$ corresponding to photon energies of $E_{\text{ph}} = 3.1 \text{ eV}$ and $E_{\text{ph}} = 1.2 \text{ eV}$. Consequently, a single laser photon cannot ionize any of the above mentioned atoms.

However, if the laser intensity is increased, an electron may absorb n photons to overcome the ionization energy. This multiphoton ionization (MPI) process is relevant for intensities $I_L > 10^{10} \text{ W/cm}^2$ [63].

At even higher intensities, the magnitude of the laser's electric field E_L is strong enough to significantly deform the atomic Coulomb potential. The potential (energy) of the system experienced by the electron is [63]

$$V(x) = -\frac{1}{4\pi\epsilon_0} \cdot \frac{Ze^2}{|x|} - exE_L. \quad (2.1)$$

ϵ_0 is the vacuum permittivity, Z is the ion charge number, and e is the elementary charge. x is parallel to the electric field. It is possible that an electron tunnels through the generated Coulomb barrier and then gets accelerated in the laser field. This mechanism is called tunnel ionization (TI).

The limit of TI is called over-the-barrier (OBT) or barrier-suppression (BS) ionization. In this case, the laser's electric field lowers the potential barrier up to the electron's energy level, then releasing this electron into the vacuum. The threshold intensity for this process is [63]

$$I_{\text{OBT}} = \frac{c\pi^2\epsilon_0^3}{2Z^2e^6} (E_{\text{ion}})^4 \approx 4.0 \cdot 10^9 \frac{\text{W}}{\text{cm}^2} \left(\frac{E_{\text{ion}}}{\text{eV}} \right)^4 \cdot \frac{1}{Z^2}. \quad (2.2)$$

For the most weakly bound electrons this gives $I_{\text{C}^+} \approx 6.5 \cdot 10^{13} \text{ W/cm}^2$, $I_{\text{O}^+} = I_{\text{H}^+} \approx 1.4 \cdot 10^{14} \text{ W/cm}^2$, and for the most strongly bound electrons $I_{\text{C}^{6+}} \approx 6.4 \cdot 10^{18} \text{ W/cm}^2$, $I_{\text{O}^{8+}} \approx 3.6 \cdot 10^{19} \text{ W/cm}^2$. This means that laser pulses of the JETI 40 and POLARIS laser systems (see Secs. A.1 and A.2) with peak intensities exceeding 10^{19} W/cm^2 can fully ionize these target materials.

The intensity of a laser pulse does not increase instantaneously from zero to its maximum value, with the result that the maximum ionization state of an atom is not reached immediately. Instead, each laser pulse with a duration on the femtosecond timescale is preceded by a picosecond long rising edge. The ratio of this

time-dependent laser intensity to the maximum is called temporal intensity contrast (TIC). The TIC of the POLARIS laser system is shown in [54] (Figs. 45 and 48). There, it can be seen that the intensity is $\approx 10^{14}$ W/cm², between 8 ps and 4 ps before the laser pulse's peak arrives with $I_L \approx 10^{20}$ W/cm². Therefore, the ionization of the target begins several picoseconds before the pulse peak's arrival, leading to the formation of a plasma.

2.2. Interaction of the laser field with a single electron

Although the laser interacts with a plasma, which has an electron number density on the order of 10^{21} /cm³ in a laser-driven ion acceleration experiment, it is useful to first study the interaction of a single electron with an electromagnetic wave. This interaction is determined by the Lorentz force

$$\frac{d\vec{p}}{dt} = \dot{\vec{p}} = -e (\vec{E} + \vec{v} \times \vec{B}). \quad (2.3)$$

$\vec{p} = m_e \vec{v} \gamma$ denotes the electron's relativistic momentum with the rest mass m_e , the electron's velocity \vec{v} , and the gamma factor $\gamma = (1 - v^2/c^2)^{-1/2} = (1 + (p/m_e c)^2)^{1/2}$. \vec{E} and \vec{B} are the electric field and the magnetic field of the wave, respectively. Different derivations of the resulting electron trajectories can be found, for example, in [63–65]. This section mainly refers to the book of Gibbon [63].

An elliptically polarized plane wave traveling along the z -axis in vacuum can be described by the vector potential

$$\vec{A} = \left(\delta A_0 \cos(\phi), (1 - \delta^2)^{1/2} A_0 \sin(\phi), 0 \right), \quad (2.4)$$

with the amplitude A_0 . $\phi = \omega_L t - k_L z$ is the phase with frequency $\omega_L = 2\pi c/\lambda_L$ and the magnitude of the wave vector $|\vec{k}_L| = k_L = 2\pi/\lambda_L$. $\delta = 0, \pm 1$ is for a linearly and $\delta = \pm 1/\sqrt{2}$ for a circularly polarized wave. The electric and the magnetic field components of the wave can be derived from \vec{A} as

$$\vec{E} = -\partial \vec{A} / \partial t = \left(\delta A_0 \omega_L \sin(\phi), - (1 - \delta^2)^{1/2} A_0 \omega_L \cos(\phi), 0 \right), \quad (2.5a)$$

$$\vec{B} = \nabla \times \vec{A} = (-E_y/c, E_x/c, 0). \quad (2.5b)$$

The intensity of the plane wave corresponds to the cycle-averaged absolute value of the Poynting vector,

$$I_L = \overline{S} = \varepsilon_0 c^2 \overline{|\vec{E} \times \vec{B}|} = \frac{1}{2} \varepsilon_0 c (A_0 \omega_L)^2 = \frac{1}{2} \varepsilon_0 c E_0^2. \quad (2.6)$$

Here, the amplitude of the normalized vector potential $a_0 := eA_0 / (m_e c)$ is introduced. Using Eq. (2.6), one obtains a relation to the laser intensity,

$$a_0 = \frac{eA_0}{m_e c} = \sqrt{\frac{I_L \lambda_L^2}{1.37 \cdot 10^{18} \text{ W}\mu\text{m}^2}}. \quad (2.7)$$

Note that for circular polarization a_0 is often defined as $a_0 = eA_0 / (\sqrt{2} m_e c)$ [13] (see $\delta = \pm 1/\sqrt{2}$ in Eq. (2.4)).

For linear polarization and $v \ll c$, the influence of the magnetic field in Eq. (2.3) can be neglected, and the electron carries out a simple oscillatory motion caused by the electric field (e.g., $\delta = 0$, assuming that the electron is at rest for $\phi = 0$). In this classical case, the ratio of the maximum speed of the oscillating electron $v_{0,\text{class}} = eA_0/m_e$ to the speed of light c corresponds to $a_0 = v_{0,\text{class}}/c$. Hence, for $a_0 \ll 1$, the electron's motion can be treated classically.

For $a_0 > 1$, the motion must be treated relativistically since the effect of the magnetic field becomes comparable to the one of the electric field. To obtain the electron's trajectory in the relativistic case, the time derivatives of the transverse momentum components $\dot{p}_{x,y}$ in Eq. (2.3) can be rewritten with the total temporal derivative of the vector potential components $dA_{x,y}/dt = (-E_{x,y}) \pm B_{y,x} (dz/dt)$ as $dp_{x,y}/dt = e (dA_{x,y}/dt)$. Integration yields

$$\hat{p}_{x,y} - \frac{e}{m_e c} A_{x,y} = \hat{p}_{x,y}(t=0) - \frac{e}{m_e c} A_{x,y}(t=0) =: C_{x,y} \quad (2.8)$$

In these two equations, the momentum components have been normalized $\hat{p}_i = p_i / (m_e c)$ ($i = x, y, z$). To derive a relation for the longitudinal momentum \hat{p}_z , one starts from Eq. (2.3) and replaces the magnetic field with the electric field using Eq. (2.5b) and the velocity with the momentum using $v_i = c\hat{p}_i/\gamma$. By eliminating the electric field components and using the temporal derivative of the gamma factor $\dot{\gamma}\gamma = \hat{p}_x \dot{\hat{p}}_x + \hat{p}_y \dot{\hat{p}}_y + \hat{p}_z \dot{\hat{p}}_z$, one obtains the simple equation $\dot{\hat{p}}_z = \dot{\gamma}$. Integration yields

$$\hat{p}_z - \gamma = \hat{p}_z(t=0) - \gamma(t=0) =: C_z. \quad (2.9)$$

C_x , C_y , and C_z in Eqs. (2.8) and Eq. (2.9) are constants of motion defined by the conditions at $t = 0$. \hat{p}_z can be connected with \hat{p}_x and \hat{p}_y by using $\gamma = \sqrt{1 + \hat{p}_x^2 + \hat{p}_y^2 + \hat{p}_z^2}$ in Eq. (2.9) giving

$$\hat{p}_z = \frac{1 + \hat{p}_x^2 + \hat{p}_y^2 - C_z^2}{-2C_z}. \quad (2.10)$$

Consider the special case of an electron starting at $\vec{r}(t = 0) = 0$ at rest yielding $C_x = \delta a_0$, $C_y = 0$, and $C_z = -1$. The electron's momentum can now be obtained by inserting these constants and Eqs. (2.4) and (2.7) in Eqs. (2.8) and (2.10) as

$$\hat{p}_x = \delta a_0 (\cos(\phi) - 1) \quad (2.11a)$$

$$\hat{p}_y = (1 - \delta^2)^{1/2} a_0 \sin(\phi) \quad (2.11b)$$

$$\hat{p}_z = \frac{a_0^2}{4} \left[(2\delta^2 + 1) - 4\delta^2 \cos(\phi) + ((2\delta^2 - 1) \cos(2\phi)) \right]. \quad (2.11c)$$

The corresponding electron trajectory in the lab frame can be derived from these three equations by using $d\phi/dt = \partial\phi/\partial t + (\partial\phi/\partial z) \cdot (dz/dt) = \omega_L/\gamma$ and integrating the equations for $v_i = c\hat{p}_i/\gamma$ over the phase ϕ as

$$x = \frac{c}{\omega_L} \delta a_0 (\sin \phi - \phi) \quad (2.12a)$$

$$y = \frac{c}{\omega_L} (1 - \delta^2)^{1/2} a_0 (1 - \cos \phi) \quad (2.12b)$$

$$z = \frac{c}{\omega_L} \frac{a_0^2}{4} \left[(2\delta^2 + 1) \phi - 4\delta^2 \sin(\phi) + (\delta^2 - 1/2) \sin(2\phi) \right]. \quad (2.12c)$$

The motion along z includes a displacement that can be associated with a drift-velocity $\bar{v}_z = ca_0^2(2\delta^2 + 1)/(4 + a_0^2(2\delta^2 + 1))$. Depending on the polarization and initial conditions, the electron may also drift along the other two axes, as is here the case for the x -axis with $\bar{v}_x = -c\delta 4a_0/(4 + 3a_0^2)$. For linear polarization, the electron's motion in a system moving with the drift velocity has the shape of the figure eight [64].

The second term in Eq. (2.12c) that describes an oscillation with ϕ is a consequence of $C_x \neq 0$ and vanishes if $\delta = 0$, or if the electron has an initial momentum $\hat{p}_{x,0} = eA_{x,0}/(m_e c)$. The last term which describes an oscillation with 2ϕ can be suppressed by using circularly polarized laser pulses. This term plays a role for ion acceleration with few nanometer thin foils (see Secs. 2.4.3 and 3.3).

A laser pulse can be described by multiplying a time-dependent amplitude, for example, a Gaussian-shaped one, to the vector potential \vec{A} . This means at the end of the laser pulse, the vector potential is zero again. Hence, from Eqs. (2.8) and Eq. (2.10) follows that the electron is at rest again or moves with the (initial) momentum determined by the constants of motion.

Consequently, it would not be possible to accelerate electrons or other charged particles with lasers. But to reach intensities with $a_0 > 1$, the laser has to be focused down to a cross section of a few square micrometers. Thus, the spatial intensity profile of the laser leads to a lateral intensity gradient that results in a force. This ponderomotive force (PF) can accelerate electrons, as shown in the next section.

2.2.1. The ponderomotive force

In this section, the derivation of the PF for the classical case by Chen will be presented [66] because it arrives at a similar result as the various more sophisticated relativistic derivations [67–69].

A linearly polarized light wave with an electric field with a spatially dependent amplitude $\vec{E}_s(\vec{r})$ can be written as $\vec{E}(\vec{r}, t) = \vec{E}_s(\vec{r}) \cdot \cos(\omega_L t)$. For the first-order solution of the Lorentz equation (Eq. (2.3)) around the point \vec{r}_0 , the $\vec{v} \times \vec{B}$ -term can be neglected. The resulting first-order solutions for the electron's velocity \vec{v}_1 and displacement $\delta\vec{r}_1$ are:

$$\vec{v}_1 = -\frac{e}{m_e \omega_L} \vec{E}_s(\vec{r}_0) \sin(\omega_L t), \quad (2.13a)$$

$$\vec{r}_1 - \vec{r}_0 = \delta\vec{r}_1 = \frac{e}{m_e \omega_L^2} \vec{E}_s(\vec{r}_0) \cos(\omega_L t). \quad (2.13b)$$

To find the second-order solution of Eq. (2.3), the electric field's spatial variation is expanded up to the first order: $\vec{E}_s(\vec{r}_1) \approx \vec{E}_s(\vec{r}_0) + ((\delta\vec{r}_1) \cdot \nabla) \vec{E}_s(\vec{r})|_{\vec{r}_0}$. The magnetic field has now to be considered as well and can be obtained by integrating Faraday's law $\nabla \times \vec{E} = -\partial\vec{B}/\partial t$. This gives $\vec{B}_1 = -\frac{1}{\omega_L} \nabla \times \vec{E}_s(\vec{r})|_{\vec{r}_0} \cdot \sin(\omega_L t)$. Inserting the first-order electric and the magnetic field together with Eqs. (2.13) in the equation of motion yields for the second-order force

$$m_e \frac{d\vec{v}_2}{dt} = -\frac{e^2}{m_e \omega_L^2} \left[\cos^2(\omega_L t) \left(\vec{E}_s(\vec{r}_0) \cdot \nabla \right) \vec{E}_s(\vec{r})|_{\vec{r}_0} + \sin^2(\omega_L t) \left(\vec{E}_s(\vec{r}_0) \right) \times \left(\nabla \times \vec{E}_s(\vec{r})|_{\vec{r}_0} \right) \right]. \quad (2.14)$$

Using the identities $\sin^2(\omega_L t) = (1 - \cos(2\omega_L t))/2$, $\cos^2(\omega_L t) = (1 + \cos(2\omega_L t))/2$, and $\vec{E}_s \times (\nabla \times \vec{E}_s) = \frac{1}{2} \nabla \vec{E}_s^2 - (\vec{E}_s \cdot \nabla) \vec{E}_s$ one obtains

$$m_e \frac{d\vec{v}_2}{dt} = -\frac{e^2}{4m_e \omega_L^2} \left[\nabla (\vec{E}_s^2) - \cos(2\omega_L t) \nabla (\vec{E}_s^2) \right]. \quad (2.15)$$

The quasi-static ponderomotive force is the first part of this equation since the second term vanishes when averaging over one laser cycle, thus

$$\vec{F}_{\text{pond}} := m_e \left\langle \frac{d\vec{v}_2}{dt} \right\rangle = -\frac{e^2}{4m_e \omega_L^2} \nabla (\vec{E}_s^2). \quad (2.16)$$

Since \vec{E}_s^2 is proportional to the laser's intensity profile, the ponderomotive force accelerates electrons away from regions of high intensity. The relativistic derivation yields a similar expression with an additional factor of $\bar{\gamma}^{-1}$ [67], where $\bar{\gamma}$ is the cycle-averaged relativistic gamma factor of the electron. With the relation $\vec{F}_{\text{pond}} = -\nabla \Phi_{\text{pond}}$, the force can be connected to a potential, which is the quiver energy of electrons in the laser field and given as [69]

$$\Phi_{\text{pond}} = m_e c^2 (\bar{\gamma} - 1). \quad (2.17)$$

Wilks *et al.* [70] found with the help of simulations that the thermal energy or temperature $k_B T_e$ (k_B is Boltzmann's constant and T_e is the electron temperature) of hot electrons in a high-intensity laser-plasma interaction scales with this ponderomotive potential as

$$k_B T_e = m_e c^2 \left(\sqrt{1 + a_0^2} - 1 \right) = 0.511 \text{ MeV} \cdot \left(\sqrt{1 + \frac{I_L \lambda_L^2}{1.37 \cdot 10^{18} \text{ W} \mu\text{m}^2}} - 1 \right). \quad (2.18)$$

The scaling of $k_B T_e$ with the ponderomotive potential was experimentally confirmed, for example, in [71, 72]. Here, it is $\bar{\gamma} = \sqrt{1 + a_0^2}$ [70, 71].¹

¹ There are slight differences in literature for $\bar{\gamma}$ and the ponderomotive potential. E.g., $\bar{\gamma}$ is defined in [13, 68, 69] as $\bar{\gamma} = \sqrt{1 + \langle a^2 \rangle} = \sqrt{1 + a_0^2/2}$ for linear polarization and $\bar{\gamma} = \sqrt{1 + a_0^2}$ for circular polarization with the respective definition for a_0 .

2.3. Laser-plasma interaction

In this section, the properties of a plasma and the transfer of a laser pulse's energy to plasma electrons will be discussed.

2.3.1. Plasma properties

A plasma consists of electrons and different ion species, as well as neutral atoms. It reacts collectively since the charged particles' motion is determined by the Lorentz force and not mainly by collisions as in a neutral gas.

2.3.1.1. Debye shielding

Although a plasma consists of positively and negatively charged particles, it appears (quasi-)neutral on long distances since the electrons (and ions) can arrange themselves to shield electric fields. Consider a positive charge, for example, a point charge q with the corresponding electric potential $\phi_{\text{vac}}(\vec{r}) = q/(4\pi\epsilon_0|\vec{r}|)$ in vacuum. This charge is now placed within a plasma that consists of electrons and ions with particle densities n_e and n_i . As a consequence, the electrons start to move towards the positive charge, modifying the potential to $\phi = \phi_{\text{vac}}(\vec{r}) \exp(-|\vec{r}|/\lambda_D)$ [73].

$$\lambda_D = \sqrt{\frac{\epsilon_0 k_B T_e}{n_e e^2}} \quad (2.19)$$

is the so-called Debye length which defines the distance over which a potential is reduced additionally due to the plasma shielding by e^{-1} (Euler's number) [66, 73]. The shielding is usually caused by electrons only because they are more mobile than ions due to their lower mass. In a typical laser-driven proton acceleration experiment, λ_D is usually on the order of $1 \mu\text{m}$ [74]. Debye shielding only works if the number N_e of electrons in a sphere with the radius λ_D is large enough: $N_e = (4/3)\pi n_e \lambda_D^3 \gg 1$. If this condition is fulfilled, the plasma appears neutral on distances $L \gg \lambda_D$.

2.3.1.2. Light propagation in a plasma

If electrons are displaced in a plasma, a restoring charge separation field builds up between the displaced electrons and the much heavier, stationary ions. This field pulls the electrons back to their initial position. Due to their inertia, the electrons

will overshoot and start to oscillate. The frequency of this oscillation is called the plasma frequency [63, 66]

$$\omega_p = \sqrt{\frac{n_e e^2}{\varepsilon_0 m_e \bar{\gamma}}}. \quad (2.20)$$

Here, $\bar{\gamma}$ is averaged over the time and over the local electron population. ω_p is part of the dispersion relation for an electromagnetic wave propagating in a plasma with no additional external magnetic field present,

$$\omega_L^2 = \omega_p^2 + k_L^2 c^2. \quad (2.21)$$

Consider a plane wave described by $\vec{E} = \vec{E}_0 \exp(i(k_L z - \omega_L t))$. For $\omega_L > \omega_p$, Eq. (2.21) gives $k_L = c^{-1} \sqrt{\omega_L^2 - \omega_p^2}$, meaning that the wave can propagate within the plasma. But for $\omega_L < \omega_p$, the wave number becomes imaginary since $k_L = ic^{-1} \sqrt{\omega_p^2 - \omega_L^2}$. One obtains $\exp(ik_L z) =: \exp(-z/\delta)$, with the skin depth

$$\delta = \frac{c}{\sqrt{\omega_p^2 - \omega_L^2}}, \quad (2.22)$$

which is the distance over which the laser's electric field is attenuated by e^{-1} .

The phase velocity and the group velocity in a plasma are given due to Eq. (2.21) by $v_{\text{ph}} = \omega_L/k_L =: c/\eta$ and $v_{\text{gr}} = \partial\omega_L/\partial k_L =: \eta c$, respectively. η is the plasma's refractive index [13, 63],

$$\eta = \sqrt{1 - \left(\frac{\omega_p}{\omega_L}\right)^2} = \sqrt{1 - \frac{n_e}{\bar{\gamma} n_c}}. \quad (2.23)$$

n_c is the so-called critical density in the classical, low-intensity limit, for which $\omega_L = \omega_p$ with $\bar{\gamma} = 1$. Therefore, n_c divides a plasma in transparent, called underdense, for $n_e < n_c$ and in opaque, called overdense, for $n_e > n_c$. It is

$$n_c = \frac{\varepsilon_0 m_e \omega_L^2}{e^2} \approx \frac{1.1 \cdot 10^{21} \text{ } \mu\text{m}^2}{\lambda_L^2 \text{ cm}^3}. \quad (2.24)$$

Since the plasma frequency and the refractive index depend on the electron's relativistic mass $m_e \bar{\gamma}$, an initially opaque plasma can become transparent during the interaction with a high-intensity laser because the electrons gain kinetic energy. This effect is called relativistic transparency (RT) [75].

2.3.1.3. Plasma expansion

Consider a planar plasma in vacuum that consists of a single ion species with density n_{i0} and electrons with density $n_{e0} = Zn_{i0}$ with a temperature $k_B T_e$ at $t = 0$. Caused by the thermal motion or kinetic pressure, the plasma starts to freely expand into the vacuum. This expansion shall be considered as isothermal and one-dimensional, whereby the ions are no longer treated as stationary but as a fluid. Then, the density profile of the plasma can be described by an exponential function as [73]

$$n_e \approx Zn_i = n_{e0} \exp\left(-\frac{z}{L}\right). \quad (2.25)$$

L is the plasma's scale length and is defined as $L = c_s t$, with the ion sound speed,

$$c_s = \sqrt{\frac{Zk_B T_e}{m_i}} \approx 3 \cdot 10^5 \frac{\text{m}}{\text{s}} \cdot \sqrt{\frac{k_B T_e}{\text{keV}} \cdot \frac{Z}{A}}. \quad (2.26)$$

m_i is the mass of one single ion, and A is the atomic mass number. For a laser with a constant intensity of 10^{16} W/cm^2 and $\lambda_L = 0.4 \mu\text{m}$, the electron temperature may be estimated via the ponderomotive scaling as $k_B T_e \approx 0.3 \text{ keV}$. If the ions are protons, the sound velocity takes a value of $c_s \approx 0.16 \mu\text{m/ps}$, and the plasma's scale length after an expansion time of $t \approx 5 \text{ ps}$ is $L \approx 0.8 \mu\text{m}$. This is only twice the experimentally deduced scale length for the experiment with water droplets (see Sec. 4.2). In that case, however, the laser-intensity profile was not constant and the (spherical) geometry differed from the above-assumed 1D planar geometry.

If this (pre-)plasma is irradiated by a high-intensity laser pulse, the exponential density profile will be deformed by the PF [70] already during the rising edge of the laser pulse on a ps-timescale. That will eventually lead to shorter scale lengths when the pulse peak arrives. Due to the spatially varying intensity in the laser's focus, the plasma's surface will be bent. This effect has consequences for the absorption of energy by the plasma.

2.3.2. Laser absorption and electron heating

To accelerate a (classically described) proton with mass m_p to the speed of light it would be necessary to achieve $a_0 = m_p/m_e \approx 1836$, which corresponds to a laser intensity of about $5 \cdot 10^{24} \text{ W/cm}^2$ ($\lambda_L = 1 \mu\text{m}$). This intensity cannot be reached with current laser systems [6, 7]. Therefore, ions cannot be accelerated to MeV energies

directly by the laser field. The acceleration of ions is thus due to the energy transfer from electrons that have previously absorbed laser energy.

2.3.2.1. Collisional absorption

Laser energy can be absorbed by plasma electrons if they interact (collide) with the ions' electric field. This process is called inverse bremsstrahlung or collisional absorption and depends on the electron-ion collision frequency estimated as [73]

$$\nu_{ei} = \frac{e^4}{3(2\pi)^{3/2} \varepsilon_0^2 m_e^{1/2} (k_B T_e)^{3/2}} \frac{Z n_e \cdot \ln \Lambda}{\text{cm}^3} \approx 3 \cdot 10^{-6} \cdot \frac{\ln \Lambda \cdot Z n_e \text{ cm}^3}{(k_B T_e)^{3/2} \text{ eV}^{-3/2}} \text{ s}^{-1}. \quad (2.27)$$

$\ln \Lambda$ is the Coulomb logarithm, where Λ is the quotient of λ_D and the shortest distance between an electron and an ion. The value of $\ln \Lambda$ for laser-plasmas lies between 2 and 5 [69]. The frequency of collisions between electrons ν_{ee} is comparable to ν_{ei} . In [76], it is given as $\nu_{ee} \approx 2\nu_{ei}$. The time $\tau \gg \tau_{ee} = 1/\nu_{ee}$ can be considered as the time required by an electron plasma to reach thermal equilibrium by collisions [69]. To approximate ν_{ei} as a function of the laser's intensity, the electron temperature in Eq. (2.27) may be estimated via the ponderomotive scaling Eq. (2.18). Using $n_e = n_c$ ($\lambda = 0.4 \mu\text{m}$), $\ln \Lambda \approx 5$, and $Z = 1$, ν_{ei} varies in an intensity range between 10^{12} W/cm^2 and 10^{18} W/cm^2 from $\nu_{12} \approx 2 \cdot 10^7 \text{ ps}^{-1}$ to $\nu_{18} \approx 2 \cdot 10^{-2} \text{ ps}^{-1}$. The inverse $1/\nu_{18}$, i.e., the time between collisions at relativistic intensities, is much longer than the FWHM-duration of the pulses of the JETI 40 and POLARIS laser systems. Consequently, collisions are negligible for the interaction of the laser pulse's peak with a target and thus for the generation of hot electrons. The electrons perform collective motions, in this case, and collisionless absorption mechanisms become dominant, which will be sketched in the following sections. Nevertheless, during the rising edge of the laser pulse on the ps-timescale, collisional absorption will contribute to the generation and heating of a pre-plasma.

2.3.2.2. Resonance absorption

Consider a p-polarized laser beam that is obliquely incident under an angle θ on a foil, with a pre-plasma with scale length L on the front surface. This configuration leads to a component of the laser's electric field pointing into the foil.

The laser is continuously refracted during its propagation inside the plasma, where the density at the reflection point (i.e., the point of closest approach) of the laser

is given by $n_{\text{er}} = n_c \cos^2 \theta$ [73]. This means that for $\theta > 0^\circ$ the laser is always reflected before reaching the critical density. But since the electric field strength within the plasma decreases exponentially (see Sec. 2.3.1.2 and Eq. (2.22)), the field can still excite an electron plasma oscillation at the region of the critical density, where $\omega_L = \omega_p$. Hence, this oscillation is driven resonantly and will eventually break, accelerating hot electrons into the foil. For the case $k_L L \gg 1$, the fraction of absorbed laser light can be estimated as [63]

$$f = \frac{1}{2} \left(2.3\xi \exp\left(-2\xi^3/3\right) \right)^2, \quad (2.28)$$

where $\xi = (\omega_L L/c)^{1/3} \sin \theta$. Thus, the absorption of energy only depends on the scale length and the angle of incidence but not on the laser's intensity. Eq. (2.28) can take values $> 80\%$, whereas in simulations values $> 50\%$ were obtained for laser intensities $\approx 10^{14}$ – 10^{16} W/cm² [77, 78].

Since the estimated absorption coefficient does not directly depend on the intensity, one may assume that resonance absorption will be a dominant process when the laser pulse's peak arrives. But when the intensity increases, the pressure on the pre-plasma due to the PF also increases, which will eventually steepen the plasma before the pulse peak's arrival, leading to a different heating mechanism.

2.3.2.3. Brunel heating

Brunel-heating or vacuum-heating is a mechanism responsible for electron heating in the case of steep density gradients with $a_0 > Lk_L$ [79]. The principle of this mechanism can be explained with a one-dimensional capacitor model [63]. The oscillating electric field component, which is parallel to the target normal direction, pulls during one laser half-cycle electrons out of the very short pre-plasma into the vacuum. As a result, a charge separation field between target and electron layer arises. When the laser field changes its direction, it accelerates, together with the charge separation field, the electron layer back into the target. Since the overdense plasma screens the electrons from the laser field, they have remaining kinetic energy. Simulations for irradiances $I_L \lambda_L^2 \approx 10^{14}$ – 10^{18} W $\mu\text{m}^2/\text{cm}^2$ and for scale lengths of $L/\lambda_L = 0.04$ and $L/\lambda_L = 0.1$ exhibit a scaling of the hot electron energy with $(I_L \lambda_L^2)^{1/3-1/2}$ [80]. For $I_L \lambda_L^2 \approx 10^{18}$ W $\mu\text{m}^2/\text{cm}^2$, the fraction of absorbed laser light takes values about ≈ 10 – 15% depending on L .

2.3.2.4. $\vec{j} \times \vec{B}$ -heating

In contrast to the two previous heating mechanisms, $\vec{j} \times \vec{B}$ -heating is dominant for normal laser incidence and gains importance for relativistic intensities since the heating is a consequence of the $\vec{v} \times \vec{B}$ -term in the Lorentz equation Eq. (2.3) [81]. This term drives oscillations with twice the laser frequency along the target's normal direction for a linearly polarized laser, as seen in Eq. (2.11c), Eq. (2.12c), and Eq. (2.15). Consequently, electron bunches, separated by half a laser wavelength, are accelerated into the target. For circularly polarized laser pulses, $\vec{j} \times \vec{B}$ -heating will be suppressed (see Eqs. (2.11c) and (2.12c) for $\delta = \pm 1/\sqrt{2}$).

The heating process at a target with a steep plasma density gradient can be described similarly to the Brunel heating mechanism [63]. The force due to the standing wave's magnetic field (incident plus reflected laser) pulls electrons away from the target, twice per laser cycle. When the $\vec{v} \times \vec{B}$ -term changes its direction in the following quarter cycle, the magnetic and the charge separation field accelerate electrons into the target. Inside the plasma, the electrons are shielded from the laser field and thus are effectively accelerated. The absorption process is intensity-dependent and takes values of $\approx 15\%$ for an irradiance of $\approx 10^{18} \text{ W}\mu\text{m}^2/\text{cm}^2$ [81]. The temperature of the accelerated electrons scales as the ponderomotive potential [70].

2.3.2.5. Remark on the generation of hot electrons

The heating of electrons is a complex process and depends on many parameters, like the laser's intensity or the TIC. To model ion acceleration, it is often necessary to estimate the temperature of the hot electrons and the fraction of absorbed energy. Many authors use the ponderomotive potential (see Eq. (2.18)) to estimate the temperature for their models or to compare their experimental findings with theory [82–86]. This scaling was first found with the help of simulations [70] and later experimentally confirmed [71, 72].

However, it was also experimentally found by Beg *et al.* that the electron temperature may scale with $k_B T_e \propto (I_L \lambda_L^2)^{1/3}$ [87]. This scaling could later be reproduced over an intensity range of $10^{18} \text{ W}/\text{cm}^2$ up to $10^{21} \text{ W}/\text{cm}^2$ for pulse durations between 400 fs and 5 ps, and different incidence angles between 0° and 40° , while the intensity was varied by changing the pulse energy [88, 89]. This difference to the ponderomotive scaling was attributed to the pre-plasma modification at the laser-plasma interaction region close to the critical density. Here, the high-intensity laser

pulse sweeps electrons out of the underdense region, thus reducing the electron density, while the PF steepens the near-critical interaction region [70, 90]. As stated by Haines *et al.* [91], accelerated electrons would not gain the energy equivalent to the ponderomotive potential because they would have propagated a distance into the target that is larger than the skin depth (Eq. (2.22)) before they experienced the maximum possible acceleration by the laser field. Their model is close to $k_{\text{B}}T_{\text{e}} \propto (I_{\text{L}}\lambda_{\text{L}}^2)^{1/3}$ and given by

$$k_{\text{B}}T_{\text{e}} = m_{\text{e}}c^2 \left\{ \left[1 + \frac{2}{m_{\text{e}}c} \left(\frac{m_{\text{e}}I_{\text{L}}}{n_{\text{c}}c} \right)^{1/2} \right]^{1/2} - 1 \right\}. \quad (2.29)$$

A disadvantage of this model is that it does not converge to the ponderomotive potential for non-relativistic intensities, as stated by Kluge *et al.* [92]. They developed a model that converges to the ponderomotive scaling for $a_0 \ll 1$ (with $\bar{\gamma} = \sqrt{1 + a_0^2/2}$), but shows a weaker scaling for large a_0 . It is given by

$$k_{\text{B}}T_{\text{e}} \approx m_{\text{e}}c^2 \cdot \frac{a_0^2}{4}, \quad (a_0 \ll 1), \quad (2.30\text{a})$$

$$k_{\text{B}}T_{\text{e}} \approx m_{\text{e}}c^2 \cdot \left(\frac{\pi a_0}{2 \ln 16 + 2 \ln a_0} - 1 \right), \quad (a_0 \gg 1). \quad (2.30\text{b})$$

The fraction f of absorbed energy by hot electrons was measured for intensities up to 10^{20} W/cm² [93, 94]. f increases with rising intensity from $f \lesssim 20\%$ at 10^{17} – 10^{18} W/cm² to $f \gtrsim 60\%$ at $\approx 10^{20}$ W/cm² for normal or near-normal laser incidence. For an incidence angle of 45° and intensities between $\approx 10^{17}$ W/cm² and $\approx 5 \cdot 10^{19}$ W/cm², a roughly constant absorption fraction of 50% was measured. For $I_{\text{L}} \gtrsim 10^{20}$ W/cm², f takes values $\gtrsim 80\%$. Additionally, simulations indicate that f depends also on the amount of pre-plasma present [90, 93].

2.4. Laser-driven ion acceleration

Laser-driven ion acceleration is an indirect process. The laser pulse accelerates the plasma electrons via different processes (see Sec. 2.3.2) that leads to a charge separation between electrons and ions. This charge separation generates slowly varying electric fields (compared to the oscillation period of laser light), eventually leading to an acceleration of ions. Different ion acceleration mechanisms exist, including target normal sheath acceleration (TNSA), radiation pressure acceleration (RPA),

and breakout afterburner (BOA) (see Macchi *et al.* [13] or Daido *et al.* [14] for reviews). Of these mechanisms, TNSA is the dominant one in most experiments performed, and several theoretical models have been developed to describe the process and predict the experimental results.

2.4.1. Target normal sheath acceleration

Although laser-driven ion acceleration was already observed early in the second half of the 20th century [95], it became a topic of renewed active research around the turn of the millennium [1–4]. Due to the use of CPA-laser systems [5], laser pulses could be focused to relativistic intensities ($a_0 > 1$), eventually leading to the acceleration of protons to kinetic energies of several megaelectronvolts from micrometer thick foils. These protons had their origin in contaminants on the foils' surfaces [96]. By using a wedged target [1, 2] or removing the contaminants from either the target front (laser-illuminated surface) or the target rear surface [97], it could be determined that the protons originated from the latter. A theoretical framework was developed to explain this proton acceleration process, which is called TNSA [8]. Ion acceleration via TNSA works in principle as follows (see Fig 2.1).

Firstly, a laser pulse is focused onto, for example, a μm thin metal or plastic foil. Since high-intensity lasers have a rising edge on the ps-timescale, ionization starts at least several ps before the pulse peak arrives via different mechanisms (see Sec. 2.1). During the ps-duration of the rising edge, the freed electrons are heated, ionization continues, and a pre-plasma is formed (see Sec. 2.3.1.3 and Sec. 2.3.2). When the main pulse arrives, it accelerates electrons through the foil. These electrons form a sheath in the vacuum at the rear surface of the foil. Between the electron sheath and the positively charged foil, an electric field builds up that has a strength in the order of $\text{MV}/\mu\text{m}$. Electrons with high kinetic energy may escape the interaction region, while most are held back by this electric field. However, for a foil with a transverse extent much larger than the interaction region, electrons may also leave the sheath-region along the foil's surface [57].

The electric field ionizes atoms on the rear side of the target and accelerates the ions to MeV energies. Consequently, the ion and electron distributions expand as a quasi-neutral plasma, preceded by an electron sheath, into the vacuum. This plasma expansion, respectively ion acceleration, also starts from the foil's front surface towards the direction of the incident laser [4, 98, 99].

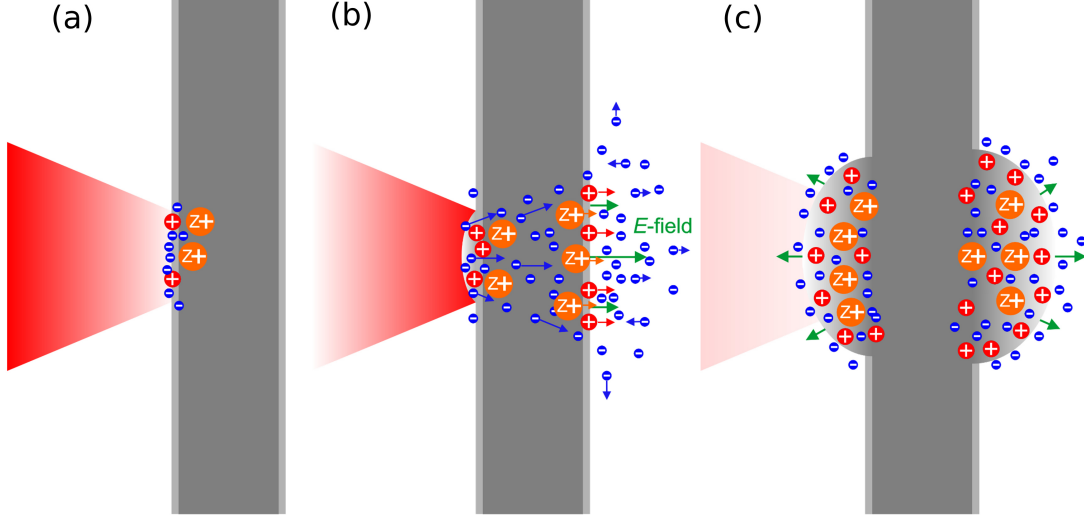


Figure 2.1.: The three images sketch the principle of the TNSA-mechanism using a μm thick foil as the target (dark gray), with contaminants on both surfaces (light gray). In (a), the laser is focused onto the foil. The rising edge ionizes the foil, and thus a pre-plasma is formed. (b) shows how hot electrons are accelerated through the foil by the pulse peak and form a sheath on the foil's rear surface. Due to the charge separation, an electric field builds up, accelerating preferably protons from the contaminant layer. Protons (and heavy ions) gain kinetic energy due to the acceleration process. Their spatial distributions expand, together with the electrons, as a quasi-neutral plasma into the vacuum, as seen in (c). See the main text for more details. Note that hole-boring also takes place at the foil's front surface (see Sec. 2.4.3.1), but was not included in these drawings for the sake of clarity.

2.4.1.1. Electron transport

Before the electrons can set up the sheath, they have to travel through the target, e.g., a foil or a droplet. The number of the generated hot electrons can be estimated by an energy balance relation $N_e \approx fE_L / (k_B T_e)$, where E_L is the laser pulse energy [13]. Assuming that the electrons are accelerated during the laser pulse duration τ_L , the induced hot electron current is $I \approx N_e e / \tau_L$ [63]. The hot electron temperature can be approximated by the ponderomotive scaling (see Eq. (2.18)). For example, for an intensity of $I_L \approx 4 \cdot 10^{19} \text{ W/cm}^2$ (parameters from the experiment with water droplets, see Sec. 4.1) and a wavelength of $\lambda_L = 0.4 \mu\text{m}$, it is $k_B T_e \approx 0.7 \text{ MeV}$. The absorption fraction will be assumed as $f \approx 0.6$ according to the results of Ping *et al.* and Gray *et al.* [93, 94] (see Sec. 2.3.2.5). With $E_L \approx 18 \text{ mJ}$ contained in the full-width-at-half-maximum (FWHM) focal spot, the number of hot electrons is $N_e \approx$

$1.0 \cdot 10^{11}$. Using $\tau_L \approx 42$ fs, these electrons correspond to a current of approximately $I \approx 0.4$ MA. In vacuum, such a current could not propagate due to self-generated magnetic fields. In the target, it is additionally affected by electric fields induced by the charge separation. However, when the target becomes an ionized plasma during the interaction (or is a metallic conductor), enough free electrons are present that the generation of these magnetic fields can induce a compensating, cold return current [100, 101]. Hence, the hot electrons can propagate through the target and set up a sheath on the target's rear surface. To approximate the sheath density directly at the target surface, it is assumed that the electrons propagate ballistically within a cone with the half-opening angle θ . For a laser beam focused under normal incidence into a focal spot with radius $r \approx 0.6 \mu\text{m}$, the density of the electrons at the target's rear surface can be approximated as [84]

$$n_{e0} \approx \frac{N_e}{c\tau_L\pi R^2}, \quad (2.31)$$

wherein $R = (r + d \tan \theta)$ is the radius of the sheath, and d is the target thickness. Here, it was assumed that the electron bunch has a length of $c\tau_L$. The full divergence angle 2θ was measured as a function of the laser intensity ([102] and refs. therein), with Ovchinnikov *et al.* [103] stating, due to their simulated results, that the intensity dependence is actually a scale length dependence. For an intensity of $I_L \approx 4 \cdot 10^{19} \text{ W/cm}^2$, 2θ was experimentally determined to be between 30° and 40° [102]. That is consistent with the simulations [103] for scale lengths $L \leq 1 \mu\text{m}$. Using $\theta \approx 18^\circ$ and a target thickness of $d \approx 20 \mu\text{m}$ (diameter of the droplets used as targets in the droplet experiment, see Sec. 4.1), it is $R \approx 7 \mu\text{m}$, and the estimated electron density is $n_{e0} \approx 5 \cdot 10^{19} \text{ cm}^{-3}$. This value is about two orders of magnitude below the critical density for $\lambda_L = 0.4 \mu\text{m}$ (see Eq. (2.24)). These hot electrons set up the sheath responsible for ion acceleration. However, one should keep in mind that these derived numbers are estimates. Additional effects can influence the hot electron density like electron recirculation [104], electrons can leave the interaction region along a foil's surface [57], or the generation of a confined surface current can increase the electron density (see Sec. 4.4).

2.4.1.2. TNSA modelling

Usually, theoretical models use an electrostatic approximation ($\partial \vec{B} / \partial t = 0$ and $\nabla \times \vec{E} = 0$) to describe the TNSA process, thus the electric field \vec{E} can be expressed

by a potential via $\vec{E} = -\nabla\phi$ [13]. This potential then satisfies the Poisson equation

$$\nabla^2\phi = \frac{e}{\varepsilon_0} \left(n_e - \sum_i Z_i n_i \right). \quad (2.32)$$

ϕ is, therefore, defined by the density distribution of electrons n_e and different ion species n_i . Consider one spatial dimension (z -axis) and treat the problem quasi-statically [13]. The latter means that the target consists of immobile heavy ions (one species with charge number Z), and that protons on the target's rear surface are treated as test particles and do not influence the electric potential. Also, the electrons are treated as isothermal. The electron density is given by the sum of hot and cold electrons $n_e = n_{e,h} + n_{e,c}$. Assuming a Boltzmann distribution for the hot electrons

$$n_{e,h} = n_{e0} \exp(e\phi(z)/(k_B T_e)), \quad (2.33)$$

and neglecting thermal effects for the cold electrons, the cold electrons and the ions have a uniform density for $z < 0$, given as $n_{e,c} = n_{e0,c}$ and $Zn_i = Zn_{i0} = n_{e0,c} + n_{e0}$. Then Eq. (2.32) yields $\partial^2\phi/\partial z^2 = e\varepsilon_0^{-1}n_{e0}(\exp(e\phi(z)/(k_B T_e)) - \Theta(-z))$. Θ is the Heaviside step function. The integration for $z > 0$ yields the potential that can be used to calculate the electric field at the target's rear surface [105]:

$$\phi(z) = \frac{k_B T_e}{e} \left[-2 \ln \left(1 + \frac{z}{\sqrt{2} e_N \lambda_{D0}} \right) - 1 \right], \quad (2.34a)$$

$$E(z=0) = \sqrt{\frac{2}{e_N} \frac{k_B T_e}{e \lambda_{D0}}} = \sqrt{\frac{2}{e_N} \sqrt{n_{e0} k_B T_e / \varepsilon_0}} =: \sqrt{\frac{2}{e_N}} E_0. \quad (2.34b)$$

A problem with this simple quasi-static approach is that protons would be accelerated infinitely due to the divergence of $\phi(z)$. Nevertheless, one may estimate the maximum electric field and the kinetic energy that a proton can gain during the acceleration process if a certain acceleration length is assumed. Using the previous estimates, the Debye length is (Eq. 2.19) $\lambda_{D0} \approx 0.9 \mu\text{m}$, leading to an electric field of $E(z=0) \approx 0.7 \text{ MV}/\mu\text{m}$. With λ_{D0} as an acceleration length, the maximum proton energy can be approximated as $E_{\text{max}} \approx -e(\phi(\lambda_{D0}) - \phi(0)) \approx 0.5 \text{ MeV}$. This value is slightly below the average maximum proton energy measured in the experiment with water droplets and high TIC for normal laser incidence (see Fig. 4.4 in Sec. 4.3). If a plasma density gradient with $L > \lambda_{D0}$ at the target's rear surface is

present during the main pulse arrival, λ_{D0} in Eq. (2.34b) has to be replaced by L [106] leading to a reduced electric field and thus to a less effective proton acceleration process.

With Eq. (2.18) as an estimation for $k_B T_e$ and λ_{D0} as the acceleration length, it is $E_{\max} \propto (I_L \lambda_L^2)^{1/2}$. Such a scaling was measured, e.g., by [4, 9, 107, 108].

2.4.1.3. Plasma expansion model

The ion acceleration process is often treated as a one-dimensional expansion of an isothermal plasma into the vacuum. This theoretical problem was already investigated in the 20th century, before the acceleration of MeV ion beams with CPA laser systems, for example, in [105, 109–111] and was further developed within the context of ion acceleration with lasers by Mora [112]. Here, only one ion species is considered, again occupying $z < 0$ and only hot electrons described by Eq. (2.33) for all times t . A solution of Eq. (2.32) for $t = 0$ leads to Eqs. (2.34). Due to the electron temperature and the associated pressure, the electrons start to expand. They pull the ions along so that both begin to propagate into the vacuum for $t > 0$. The ions are treated as an isothermal fluid and their expansion with the velocity v_i is described by the following equations:

$$\frac{\partial v_i}{\partial t} + v_i \cdot \frac{\partial}{\partial z} v_i = -\frac{Z_i e}{m_i} \frac{\partial}{\partial z} \phi, \quad (2.35a)$$

$$\frac{\partial n_i}{\partial t} + \frac{\partial}{\partial z} (n_i v_i) = 0. \quad (2.35b)$$

If one assumes quasi-neutrality, a self-similar solution of these equations for $z > -L$ is

$$n_e(z, t) = Z n_i(z, t) = n_{e0} \exp(-z/L - 1) \quad (2.36a)$$

$$v_i = c_s + z/t \quad (2.36b)$$

$$E = k_B T_e / (eL) = E_0 / (\omega_{pi} t). \quad (2.36c)$$

$\omega_{pi} = \sqrt{n_{e0} Z e^2 / (m_i \varepsilon_0)}$ is the ion plasma frequency of the initial ion distribution. The ion distribution in Eq. (2.36a) has no spatial limitation. Consequently, ions with infinite velocity and kinetic energy are predicted by this self-similar solution. In an experiment, however, an ion front is formed with a measurable maximum velocity. Such an ion front was also found by numerically solving Eq. (2.32), Eq.

(2.33), and Eqs. (2.35) [113]. The existence of this front is a consequence of the charge separation due to the formation of the electron sheath, which corresponds to the violation of quasi-neutrality at and around this position. That is why the self-similar solution has no relevance as long as $\omega_{\text{pi}}t < 1$ [112]. The location of the moving ion front can be estimated from the position where the local debye length $\lambda_{\text{D}} = \lambda_{\text{D0}}\sqrt{n_{\text{e0}}/n_{\text{e}}}$ equals L . This ion front carries a surface charge of $\sigma = \varepsilon_0 E$. An additional σ is carried by a rarefaction wave moving into the target at $z = -L$. Together with the surface charge -2σ of the electron sheath, the charge separation leads to an electric field that is given by an interpolation formula for $t \geq 0$ as [112]

$$E_{\text{front}} \approx 2E_0/\sqrt{2e_N + \omega_{\text{pi}}^2 t^2}. \quad (2.37)$$

By integrating $dv_{\text{front}}/dt = ZeE_{\text{front}}/m_i$ one obtains the velocity and thus the maximum kinetic energy an ion can gain,

$$E_{\text{max}} = 2Zk_{\text{B}}T_e \left[\ln \left(\tau + \sqrt{\tau^2 + 1} \right) \right]^2. \quad (2.38)$$

Here, $\tau = \omega_{\text{pi}}t/\sqrt{2e_N}$. The ions' energy spectrum up to E_{max} is given as

$$\frac{dN}{dE_i} = \frac{Zn_{\text{e0}}t}{\sqrt{2E_i}m_i} \exp \left(-\sqrt{\frac{2E_i}{Zk_{\text{B}}T_e}} \right). \quad (2.39)$$

E_i is the kinetic energy of an ion. To estimate E_{max} , the electron temperature $k_{\text{B}}T_e$ and the plasma density n_{e0} are necessary. Because these quantities are usually not directly accessible in an experiment, they have to be estimated as done before. The time t can be interpreted as an acceleration time. Since the model is isothermal, the protons would be accelerated infinitely if no time constraint would be included.

Different approximations for t can be found. Kaluza *et al.* [84] assumed that $t \approx \tau_{\text{L}}$, while Fuchs *et al.* [85] found that their experimental results are best reproduced by $t \approx 1.3 \cdot \tau_{\text{L}}$. This was later refined to $t = \alpha (\tau_{\text{L}} + 60 \text{ fs})$ [114], where α is intensity-dependent and $\alpha = 1.3$ for $I_{\text{L}} > 3 \cdot 10^{19} \text{ W/cm}^2$. For the experimental parameters of the water droplet experiment, one obtains $t \approx 133 \text{ fs}$. One can approximate $\omega_{\text{pi}} \approx 9.3 \cdot 10^{12} \text{ rad/s}$ and $\tau \approx 0.53$. Again using $k_{\text{B}}T_e \approx 0.7 \text{ MeV}$, the maximum proton energy is $E_{\text{max}} \approx 0.36 \text{ MeV}$, which is roughly half of the average energy obtained in the droplet experiment for normal laser incidence without a pre-plasma present (see Fig. 4.4 in Sec. 4.3). This model has been used successfully to interpret experimental results [84–86].

2.4.1.4. Model by Schreiber

A model that has been used to explain a linear scaling of the maximum proton energy as a function of the laser's pulse power, as measured in [99, 115], is the quasi-static model by Schreiber *et al.* [116]. With this model, Zeil *et al.* [115] could attribute the linear scaling to their short pulse duration of $\tau_L = 30$ fs. They compared their measurements to results obtained at other laser systems and could show that the scaling of the maximum proton energy with pulse power changes from linear, for short pulses, to rootlike, for longer pulses.

In this model, the target ions do not move, while ions from the surface are treated as test particles. The hot electron sheath induces a positive surface charge density at the target's rear surface, causing an electric potential and field [116]:

$$\phi(r=0, \xi) = -\frac{Rk_B T_e}{e\lambda_D} \left(1 + \xi - \sqrt{1 + \xi^2}\right), \quad (2.40a)$$

$$E(r=0, \xi) = \frac{k_B T_e}{e\lambda_D} \left[1 - \frac{\xi}{\sqrt{1 + \xi^2}}\right]. \quad (2.40b)$$

$\xi = z/R$ is the normalized distance, and R is the radius of the surface charge/electron sheath (see Sec. 2.4.1.1). The ion energy is given as a function of the distance from the surface as $E_i(\xi) = -Ze\phi(r=0, \xi) = E_{i,\infty} \left(1 + \xi - \sqrt{1 + \xi^2}\right)$, with $E_{i,\infty} = E_i(\xi \rightarrow \infty)$. This expression represents the energy that an ion could gain at an acceleration on an infinite distance and can be expressed by the laser pulse power $P_L = E_L/\tau_L$ as

$$E_{i,\infty} = 2Zm_e c^2 \sqrt{fP_L / (8.71 \text{ GW})}. \quad (2.41)$$

To get a better approximation for the experimentally measured maximum ion energies, it was assumed that the acceleration process stops after the electron pulse, with a duration τ_L , has passed. This leads to an implicit expression for the maximum ion energy [116] approximated as [115]

$$E_{\max} = E_{i,\infty} \tanh^2 \left(\frac{\tau_L}{2\tau_0} \right), \quad (2.42)$$

with the reference time $\tau_0 = R/\sqrt{2E_{i,\infty}/m_i}$, which can be interpreted as the time an ion stays in the region of the accelerating fields. This model provides a possible explanation for the difference in scaling with intensity. For the case of short

pulses $\tau_L \ll 2\tau_0$, the maximum ion energy is $E_{\max} \approx E_{i,\infty} (\tau_L / (2\tau_0))^2 \propto f E_L \tau_L R^{-2}$, showing a linear dependence on the laser energy. For long pulses $\tau_L \gg 2\tau_0$, $E_{\max} \approx E_{i,\infty} \propto \sqrt{f E_L \tau_L^{-1}}$, showing a scaling with the square root of the laser energy. Because of $\tau_0 \propto (\sqrt{f P_L})^{-1}$, the scaling will always converge to a square root scaling for high laser powers. Hence, this model could also be used successfully to interpret the results obtained at a high-energy laser system with a pulse duration of 500 fs [9]. An advantage of this model compared to the one-dimensional plasma expansion is that the maximum ion energy can be directly related to the laser parameters. However, assumptions need to be made for the conversion efficiency f and the radius R of the surface charge (see Secs. 2.3.2.5 and 2.4.1.1). Using the laser energy contained within the FWHM focal spot in the droplet experiment (see Sec. 4.1, $E_L \approx 18$ mJ, $\tau_L \approx 42$ fs), one has $P_L \approx 430$ GW, which gives $E_{i,\infty} \approx 5.6$ MeV and $\tau_0 \approx 214$ fs ($f \approx 0.6$ and $R \approx 7$ μm as in Sec. 2.4.1.1). The maximum proton energy is $E_{\max} \approx 0.05$ MeV, which is an order of magnitude below the measured values. A possible explanation would be that the high intensity in the experiment was achieved due to strong focusing and not by high pulse energy, which is not included in this model. Also, R could be smaller than the estimated value due to a confinement of electrons close to a droplet's surface (see Sec. 4.4), which would lead to a smaller value of τ_0 and thus to a higher E_{\max} .

2.4.1.5. Plasma expansion model for spheres

Most of the theoretical models for TNSA consider planar geometries. However, Murakami and Basko have also investigated the one-dimensional, self-similar plasma expansion in spherical geometry [117]. In contrast to the isothermal plasma expansion model by Mora [112], the hydrodynamic equations for the electron fluid were solved along with those for the ion fluid instead of assuming a Boltzmann distribution for the electrons. If the hot (relativistic) electrons are treated adiabatically, the maximum ion energy in spherical geometry is given by [117]

$$E_{i,\max} = 2Zk_B T_e \xi_f^2. \quad (2.43)$$

ξ_f is the normalized position of the ion front. It depends on the normalized initial plasma size $\Lambda = R_0 / \lambda_{D0}$, where R_0 is the initial plasma radius. λ_{D0} is the initial Debye length evaluated in the center of the radially symmetric plasma. For large plasmas with $\Lambda \gg 1$, ξ_f^2 is given by $\xi_f^2 \approx W[\Lambda^2/2]$, and for the case of

very small plasmas $\Lambda \ll (Zm_e/m_i)^{3/4}$, which would undergo a Coulomb explosion, $\xi_f^2 \approx \frac{1}{2}W\left[\frac{\pi^{1/3}}{2(Zm_e/m_i)}\Lambda^{4/3}\right]$. $W(x)$ is the Lambert W function and can be approximated as $W(x) \approx \ln(x/\ln x)$ for $x \gg 1$. The approximation for very small plasmas is close to the numerical solution for $10^{-3} \lesssim \Lambda \lesssim 50$, while the approximation for $\Lambda \gg 1$ is close to the numerical solution for $50 \lesssim \Lambda \lesssim 10^7$ (see Fig. 1 in [117]).

In this model, the initial hot electron distribution is given as $n_e \approx n_{e0} \exp\left(-\frac{r^2}{R_0^2}\right)$, with r being the radial coordinate. Consequently, this would lead to an isotropic expansion of ions. Such an expansion behavior could not be identified in the simulations for the droplet experiment (see Fig. 4.8 in Sec. 4.4). Since the high intensity in this experiment was achieved by a very small focus (see Sec. 4.1), the droplets were not uniformly heated, and thus the hot electron density would not follow such a radially symmetric distribution.

However, the estimation of the maximum proton energy comes, nevertheless, close to the measured values. Using the radius of a water droplet (see Sec. 4.1) as the plasma radius ($R_0 \approx 10 \mu\text{m}$) and the previously estimated number of hot electrons $N_e \approx 1.0 \cdot 10^{11}$ (see Sec. 2.4.1.1), one can calculate a theoretical hot electron density at $r = 0$ with $N_e \approx 4\pi \int_0^\infty n_e r^2 dr$. This gives $n_{e0} \approx 1.8 \cdot 10^{19} \text{cm}^{-3}$ and thus $\lambda_{D0} \approx 1.5 \mu\text{m}$. Although $\Lambda = 7 > 1$, the approximation for small plasmas comes closer to the numerical solution, as mentioned before, hence this will be used to estimate the maximum proton energy, which is then $E_{p,\text{max}} \approx 5.3 \text{MeV}$. This value is less than a factor of 2 higher than the highest proton energies in Fig. 4.4 and Fig. 4.6 in Sec. 4.3.

2.4.2. Ion acceleration with thin foils

For experiments with foils, it was found that the foil thickness is, in several cases, a crucial parameter influencing the measured ion energies [84, 98, 99, 104, 118, 119]. The investigated foil thicknesses are usually between tens of micrometers and a few nanometers. It was found that the maximum ion energy usually increases for decreasing foil thickness. This rise can be attributed to an enhanced electron density at the target rear side due to the electrons' divergence within the target [84] or due to electron recirculation between the two target surfaces during the duration of the laser pulse [104]. However, if the foils' rear surface is affected by the laser's prepulse, the maximum ion energy decreases for foils thinner than a certain optimum foil thickness [84].

To investigate ion acceleration with very thin foils, down to a few nanometers, it is, therefore, necessary to improve the TIC. Possible methods are a plasma-mirror (PM) [120, 121], a double plasma-mirror (DPM) [122], or the use of second harmonic generation (SHG) [123].

In experiments with a DPM, a strong increase in the maximum energy of C^{6+} ions was observed for 10 nm thin carbon foils and circular polarization [48], whereas an earlier experiment showed an increase in the kinetic energy of protons and C^{6+} for 5 nm thin carbon foils and linear polarization [45]. This significant rise in the maximum ion energies for very thin foils cannot be explained with the previous TNSA models. One possible explanation can be given within the framework of radiation pressure acceleration (RPA) in the light-sail (LS) Regime [43, 44, 124].

2.4.3. Radiation pressure acceleration

Since the maximum proton energy within the TNSA framework scales, for most cases, with the square root of the laser energy, as previously discussed, there is a great interest in the investigation of other acceleration mechanisms. A different concept is ion acceleration via the pressure of light, the so-called radiation pressure acceleration. When light, described as a photon flux dN/dt , is reflected by a perfectly reflective surface, it exerts a force on the surface. This force is given by the change in momentum as $dp/dt = 2h\nu/c \cdot dN/dt$, wherein $2h\nu/c$ is the momentum change of a single reflected photon. If this force acts on a surface element dA , it applies the pressure $p_{\text{rad}} = 2I_L/c$.

2.4.3.1. Hole-boring

If a high-intensity laser interacts with an overdense plasma, the radiation pressure is exerted by the quasistatic PF acting on the plasma electrons. A normally incident laser can travel up to the position of the critical density, where it gets partially reflected or absorbed. Here, the PF pushes the plasma electrons towards regions of higher density. This process creates a charge separation between the pushed electrons and the ions left behind (see Fig. 2.2 (b) and (c)). The resulting electric field holds the electrons back but at the same time pulls the ions along. This plasma layer, which consists of ions and electrons, is continuously pushed by the light pressure into the target. This process is called hole-boring (HB) and the plasma layer is called HB-front in the following.

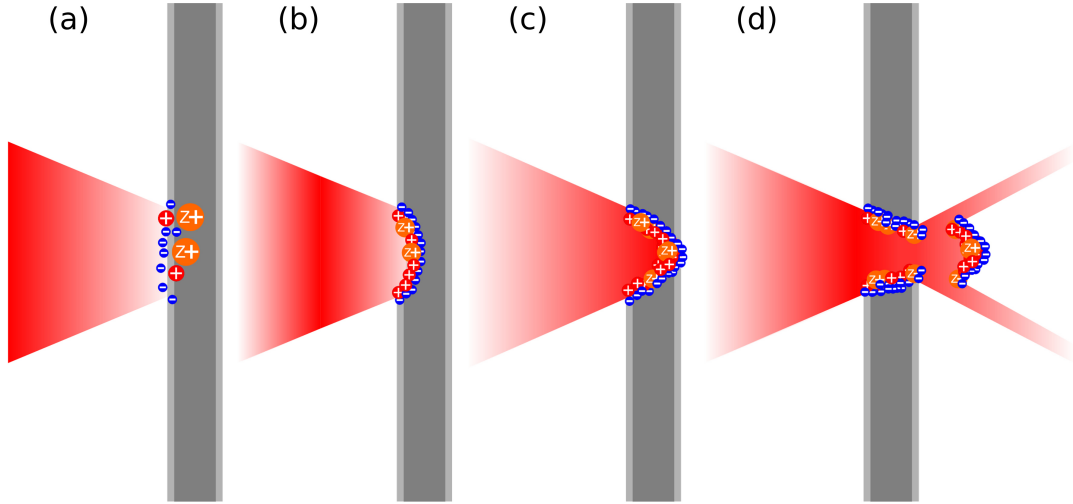


Figure 2.2.: The four images sketch the principle of RPA with a nanometer-thin foil (dark gray). Proton-containing natural contaminants are indicated in light gray. In (a), the laser is focused onto the foil, ionization starts, and a pre-plasma is formed. Then, the laser's PF pushes the electrons into the foil, creating a charge separation between the electrons and the remaining ions, as shown in (b). Due to the arising electric field, the electrons are held back while the ions follow the electrons. This layer is pushed into the target by the laser. If the foil is thin enough, the laser can drill a hole through the entire foil, which is shown in (c), and separate a part of the layer from the foil, as sketched in (d). This separated layer is accelerated like a light-sail or flying mirror. More details are in the text. Note that TNSA takes also place (see Sec. 2.1) but was not included in these drawings for the sake of clarity.

Consider a laser with a constant intensity I_L that is irradiating a plasma with a uniform density (one ion species). The velocity of the HB-front v_B can be obtained via the relativistic pressure balance in the frame of the HB-front [125, 126]:

$$p_{\text{rad}} = \frac{2I_L}{c} \frac{1 - \beta_B}{1 + \beta_B} = 2\gamma_B^2 m_i n_i v_B^2. \quad (2.44)$$

Here, it is $\beta_B = v_B/c$ and $\gamma_B = 1/\sqrt{1 - \beta_B^2}$. The term $(1 - \beta_B)/(1 + \beta_B)$ is a consequence of the relativistic Doppler shift. Solving this equation for v_B yields

$$v_B = \frac{\sqrt{B}}{1 + \sqrt{B}} c, \quad (2.45)$$

whereas $B = I_L \cdot (m_i n_i c^3)^{-1} = \alpha Z a_0^2 n_c m_e / (m_i n_e)$ with $n_e = Z n_i$. Here, it is $\alpha = 1$

for circular polarization and $\alpha = 1/2$ for linear polarization (see Sec. 2.2 for the polarization dependency of a_0). The ions with the highest kinetic energy are the ones that are initially at rest in the laboratory frame and ahead of the HB-front. These ions get accelerated by the electric field of the HB-front (reflected in the frame of the HB-front) and thus have a velocity of $v_i/c = 2\beta_B / (1 + \beta_B^2)$ (relativistic addition of two times v_B). Hence, the kinetic energy is

$$E_{\text{kin}} = 2m_i c^2 \left[\frac{B}{1 + 2\sqrt{B}} \right]. \quad (2.46)$$

For $B \ll 1$, Eq. (2.46) can be approximated as $E_{\text{kin}} \approx 2m_i c^2 B$. The maximum kinetic energy is then directly proportional to the laser's intensity. For increasing B , the scaling converges to a square-root scaling as for TNSA. Another characteristic of $E_{\text{kin}} \approx 2m_i c^2 B$ is the inverse proportionality to the electron density. This could be exploited by accelerating protons with a CO₂ laser ($\lambda_L = 10 \mu\text{m}$) that was focused into hydrogen gas [127]. Such a gas is underdense for a laser with a wavelength of $1 \mu\text{m}$ and cannot be used for proton acceleration. However, due to the longer wavelength of $10 \mu\text{m}$, the critical density is reduced by a factor of 100 and the target becomes overdense (see Eq. 2.24 and Sec. 2.3.1.2). Hence, such a gas becomes a target with few times the critical density usable for proton acceleration.

A different derivation for HB that yields the same result is given by Macchi *et al.* [128]. Their simulations show that the ions are accelerated with velocity $2v_B$ due to the breaking of the steepened ion density at the HB-front for the case of circular polarization. For this explanation, the ions with the highest velocity originate from within the HB-front, whereas for the derivation here presented, the ions with the highest velocity are reflected by the HB-front.

2.4.3.2. Light-sail

The HB-process is independent of the target thickness. But if an irradiated foil is thin enough, the hole drilled into the foil by the laser may go all the way through the foil during the interaction (Fig. 2.2 (c) and (d)). In this case, the laser may push out a part of the foil and accelerate it further as long as this layer's density is higher than the critical density. This plasma layer behaves like a light-sail or flying mirror, whereby the reflected light undergoes a redshift. Such an acceleration scheme was shown in simulations [43].

The simple model of a flying mirror can be applied to estimate the energy of accelerated ions as a function of the laser parameters. The relativistic momentum of the plasma layer is $p = Mc\beta\gamma$, with $M = \rho Ad = m_i n_i Ad$ as the entire mass of the layer with the mass density ρ . A is the area of the pushed-out layer, which can be interpreted as the laser's focal spot area. Under the assumption that the foil is perfectly reflective, the force accelerating it due to the light pressure is $dp/dt = 2AI_L/c \cdot (1 - \beta)/(1 + \beta)$. The equation of motion for the layer in the laboratory frame is [44, 124]

$$\frac{d(\beta\gamma)}{dt} = \gamma^3 \frac{d\beta}{dt} = \frac{2I_L}{m_i n_i d c^2} \frac{1 - \beta}{1 + \beta}. \quad (2.47)$$

I_L is a function of the retarded time $t - z/c$, where z is the position of the layer. The velocity of the foil as a function of the laser's fluence can be obtained from this equation as

$$\beta = \frac{(1 + D)^2 - 1}{(1 + D)^2 + 1}. \quad (2.48)$$

$D = 2F/(m_i n_i d c^2)$, with F being the fluence of the laser pulse. Assuming a flat-top intensity profile and circular polarization (see difference in definition of a_0 in Sec. 2.2 and Eq. (2.7)), F can be approximated as $F \approx I_L \tau_L = m_e c^3 n_c a_0^2 \tau_L$. That yields

$$D \approx 2\pi \frac{Z m_e c a_0^2 \tau_L}{m_i \zeta \lambda_L}. \quad (2.49)$$

ζ is the normalized areal density and defined as [129]

$$\zeta = \frac{\omega_p^2 d}{2\omega_L c} = \pi \frac{n_e d}{n_c \lambda_L}. \quad (2.50)$$

ζ divides the foil in intrinsically fully transparent for $\zeta \ll 1$ and opaque for $\zeta \gg 1$. It was found that $a_0 \approx \zeta$ corresponds to the threshold of transparency due to relativistic effects (for $\zeta \gg 1$) and yields an optimum foil thickness for ion acceleration in the light-sail regime [44, 45, 124, 130] (Eq. (2.50) is given without the prefactor π in [45, 130]). Esirkepov *et al.* [131] obtained a comparable relation from PIC-simulations. For the POLARIS laser and a fully ionized diamond-like-carbon (DLC) target with $\rho \approx 2.15 \text{ g/cm}^3$ (Micromatter Technologies Inc. [132]) respec-

tively $n_e \approx 600 n_c$, the condition $a_0 \approx \zeta$ yields

$$d \approx (0.55 \cdot a_0) \text{ nm.} \quad (2.51)$$

The maximum energy of an ion of the plasma layer can be calculated by Eq. (2.48) as [124]

$$E_{\text{ion}} = m_i c^2 (\gamma - 1) = A m_p c^2 \left(\frac{D^2}{2(D+1)} \right). \quad (2.52)$$

This equation gives the scaling of the maximum ion energy as a function of the laser's fluence. For the case $a_0 \approx 1$, it is $D \ll 1$ and E_{ion} starts with a quadratic dependence on the laser's fluence that changes to a linear scaling for $D \gg 1$. An important condition for LS acceleration is that the charge separation layer remains stable. This requires that the laser only acts via the quasistatic PF (Eq. (2.16)) on the electron layer and that the generation of hot electrons is significantly reduced. As a consequence, normal laser incidence and circular laser polarization are beneficial. Recent experiments and simulations show indeed that circular polarization yields higher ion energies than linear polarization [48] and that there exists an optimal target thickness, which is smaller for circular polarization.

The LS phase may stop as soon as the plasma layer's density gets underdense, and the laser breaks through. However, the laser may now additionally heat the electrons, thus yielding higher ion energies. This acceleration regime is called the "breakout afterburner" (BOA) [133–136].

2.5. Particle-in-cell simulations

Analytical models for describing laser-driven proton acceleration, such as those briefly described in the previous sections, provide valuable insight into the acceleration process. With few known laser parameters like pulse energy, pulse duration, and focus size, these models allow to estimate the maximum proton energy and provide information on how the proton energy scales with the laser parameters for the different acceleration mechanisms (TNSA, RPA). In an experiment, however, there are further parameters that can influence the outcome and are not included in such models. Such parameters are the laser's polarization, the angle of incidence on the target, the TIC of the laser pulse, and others. Moreover, with such models,

it is not possible to interpret all experimental observations, like the spatial profile of the proton beam.

Consequently, simulations are used as a tool for the interpretation of complex experiments. Thereby, the fundamental physical laws describing the evolution of the system under consideration are solved by a computer. Due to a large number of particles in a plasma, this is not straightforward. For example, consider a plasma with $n_e = 10n_c$ (Eq. (2.24) for $\lambda_L = 1\ \mu\text{m}$) in a volume of $10^3\ \mu\text{m}^3$. Then one has $\approx 10^{13}$ electrons plus the corresponding ions. This number of particles is too large to describe each particle individually.

Hence, for the simulation of plasmas with a feasible computational effort, the particle-in-cell (PIC) method was developed [137, 138]. The simulations that were used to interpret the experiments presented within this thesis were performed with the PIC code EPOCH [139–141]. A significant reduction of the computational time is achieved by combining a large number of particles (e.g., millions of electrons) to one macroparticle, which represents the mass and the charge of all these particles. The electric and magnetic fields generated by these macroparticles are calculated via the laws of Ampère and Faraday:

$$\nabla \times \vec{B} = \mu_0 \varepsilon_0 \partial \vec{E} / \partial t + \mu_0 \vec{j}, \quad (2.53a)$$

$$\nabla \times \vec{E} = -\partial \vec{B} / \partial t. \quad (2.53b)$$

The fields are used to calculate the change in position and velocity caused by the Lorentz force (Eq. 2.3). Maxwell's Equations are solved numerically using a finite-difference time-domain scheme (FDTD) in EPOCH, with the fields being defined on a Yee grid [142]. The simulated space is divided into blocks (in 3D) with volume $\Delta x \Delta y \Delta z$, whereas a cell (center) is specified with the indices $(i, j, k) := (i\Delta x, j\Delta y, k\Delta z)$ [139–141]. The electric and magnetic field variables are defined on such a cell's surface as $\vec{E}^n = (E_{x_{i+1/2,j,k}}^n, E_{y_{i,j+1/2,k}}^n, E_{z_{i,j,k+1/2}}^n)$ and $\vec{B}^n = (B_{x_{i,j+1/2,k+1/2}}^n, B_{y_{i+1/2,j,k+1/2}}^n, B_{z_{i+1/2,j+1/2,k}}^n)$. The subscripts denote the spatial coordinates of the field components, while the superscript $n := n\Delta t$ is the index of the simulated time with the discrete time step Δt . Unlike the fields, the macroparticles can take any position within the simulated space. Therefore, it is necessary to transfer the fields defined on the grid to the location of the particles. Likewise, the particle properties required to calculate the current density on the grid must be transferred to it. One possibility would be to treat a macroparticle as a point

and use the nearest field values to calculate the force on the particle. However, this would lead to discrete changes in force when a particle crosses the boundary of a cell. Thus, macroparticles are defined to have a finite shape corresponding to a particle density distribution. Such macroparticles are treated as charge clouds, which means that several of them can overlap. The fields that accelerate a macroparticle are derived by calculating the overlap of the particle with the different fields, which are described as rectangular functions centered around the corresponding grid point. To obtain the particle properties, on the other hand, the macroparticles' overlap with the cell under consideration is calculated.

After the initialization of the simulation, the changes in the fields and particle properties are calculated. Eqs. (2.53) are used to calculate the fields' change for a half time step $n \rightarrow n + 1/2$, hence [140, 141]

$$\vec{E}^{n+1/2} = \vec{E}^n + \frac{\Delta t}{2} \left(c^2 \nabla \times \vec{B}^n - \frac{\vec{j}^n}{\epsilon_0} \right), \quad (2.54a)$$

$$\vec{B}^{n+1/2} = \vec{B}^n - \frac{\Delta t}{2} (\nabla \times \vec{E}^{n+1/2}). \quad (2.54b)$$

With the fields defined on the Yee grid, the first lines of these equations are explicitly written out as

$$\begin{aligned} E_{x_{i+1/2,j,k}}^{n+1/2} &= E_{x_{i+1/2,j,k}}^n + (\Delta t/2) \cdot c^2 \left(B_{z_{i+1/2,j+1/2,k}}^n - B_{z_{i+1/2,j-1/2,k}}^n \right) / \Delta y \\ &- (\Delta t/2) \cdot c^2 \left(B_{y_{i+1/2,j,k+1/2}}^n - B_{y_{i+1/2,j,k-1/2}}^n \right) / \Delta z - (\Delta t/2) \cdot \left(j_{x_{i+1/2,j,k}}^n / \epsilon_0 \right), \\ B_{x_{i,j+1/2,k+1/2}}^{n+1/2} &= B_{x_{i,j+1/2,k+1/2}}^n - (\Delta t/2) \left(E_{z_{i,j+1,k+1/2}}^n - E_{z_{i,j,k+1/2}}^n \right) / \Delta y \\ &- (\Delta t/2) \left(E_{y_{i,j+1/2,k+1}}^n - E_{y_{i,j+1/2,k}}^n \right) / \Delta z. \end{aligned}$$

Thus, the spatial derivatives to determine the new field components were replaced by the differences of the direct neighbors on the Yee grid. After these calculations by EPOCH's field solver, EPOCH's particle pusher calculates the new position and momentum for each macroparticle as

$$\vec{r}^{n+1/2} = \vec{r}^n + \frac{\Delta t}{2} \vec{v}^n, \quad (2.56a)$$

$$\vec{p}^{n+1} = \vec{p}^n + q \Delta t \left[\vec{E}^{n+1/2}(\vec{r}^{n+1/2}) + \frac{\vec{p}^{n+1/2} \times \vec{B}^{n+1/2}(\vec{r}^{n+1/2})}{m \gamma^{n+1/2}} \right], \quad (2.56b)$$

$$\vec{r}^{n+1} = \vec{r}^{n+1/2} + \frac{\Delta t}{2} \vec{v}^{n+1}. \quad (2.56c)$$

Here, it is $\vec{p}^{n+1/2} = (\vec{p}^{n+1} + \vec{p}^n) / 2$. \vec{p} , \vec{v} , and γ are connected as in Sec. 2.2. Eq. (2.56b) is split according to the effects of the electric and magnetic fields [141] using the Boris rotation algorithm [143].

Solving this equation requires, as already mentioned, that the fields defined on the grid have to be evaluated at each macroparticle's position $\vec{r}^{n+1/2}$. For the calculation of the current density \vec{j}^{n+1} [144, 145], the particles' position for the next half time step $n + 3/2$ is calculated but then discarded [140]. With \vec{j}^{n+1} , $\vec{E}^{n+1/2}$, and $\vec{B}^{n+1/2}$, the fields at $n + 1$ are calculated as

$$\vec{B}^n = \vec{B}^{n+1/2} - \frac{\Delta t}{2} (\nabla \times \vec{E}^{n+1/2}), \quad (2.57a)$$

$$\vec{E}^{n+1} = \vec{E}^{n+1/2} + \frac{\Delta t}{2} \left(c^2 \nabla \times \vec{B}^{n+1} - \frac{\vec{j}^{t+1}}{\varepsilon_0} \right). \quad (2.57b)$$

Afterward, the entire process is repeated for the next time step. Simulations are often limited to two (or one) spatial dimensions to reduce the computational effort. The simulations used to interpret the experiments presented in this thesis were performed in 2D, which means that the particles are restricted to one plane. For the determination of all field components, however, the particles are still assigned a momentum in the third dimension.

To further reduce the computational effort, the extension of the simulated interaction area is usually limited to tens of micrometers in each considered dimension, and the runtime of a simulation is in the order of hundreds of femtoseconds or few picoseconds. Consequently, effects due to the tens of picoseconds long rising edge of the TIC of the laser or due to additional pre-pulses must be included as initial conditions in the simulation, if necessary. In the water droplet experiment, the pre-plasma due to the pre-pulse was measured, and an idealized pre-plasma profile was added in the simulation (see Sec. 4.2). Instead of measuring the pre-plasma, it can also be simulated with a hydrodynamic simulation code like MULTI-fs [146]. This fluid code can simulate the plasma expansion on longer timescales for intensities below 10^{17} W/cm^2 .

3. Ion acceleration with thin foils

In this chapter, the results of two experiments performed at the POLARIS laser system (see Sec. A.2 for a brief description of the laser system) with submicron thin foils are presented. To prevent such thin foils from being destroyed or becoming underdense before or when the main laser pulse peak arrives, the temporal intensity contrast (TIC) of POLARIS had to be enhanced.

In an experiment with a plasma mirror (PM), the change in the kinetic energy of the accelerated ions as a function of foil thickness, laser pulse energy, and polarization was investigated.

To investigate the characteristics of the proton beam profile originating from plastic foils with thickness d between 100 nm and 800 nm, the TIC improvement was achieved by frequency-doubling the laser pulses. The experimental results could be reproduced and explained with the help of 2D-PIC simulations.

This chapter starts with the devices that were used to detect the accelerated ions in the experiments, followed by the setups in the target chamber of POLARIS. After the presentation of the results, the chapter concludes with a detailed discussion of the results.

3.1. Ion diagnostics

This section presents the diagnostics used to investigate laser-driven ion acceleration. To measure the spectrum of accelerated ions and determine their maximum kinetic energy, a Thomson parabola (TP) spectrometer was used. Measurements of the proton beam's spatial profile were performed using either nuclear track detectors (CR-39) or a time-of-flight spectrometer consisting of a plastic scintillator in combination with a gateable CCD camera (G-CCD).

3.1.1. The Thomson parabola spectrometer

In a typical laser-driven ion acceleration experiment, several different ion species are accelerated. For example, if water droplets are the target, protons and oxygen ions with different charge states and kinetic energies are emitted from the droplets. For a certain ion species, like protons, particles with different kinetic energies are temporally but not spatially separated. Additionally, these ions may overlap in time and space with the other ion species. To measure the kinetic energy spectrum of a certain ion species it is, therefore, necessary to separate the ions with respect to their species and kinetic energies. A spectrometer widely used in laser-plasma physics for this purpose is the TP [147–150].

In principle, a TP consists of the following four components (Fig. 3.1 (a)): an entrance aperture to reduce the ion beam's diameter, an electric and a magnetic field region, the fields being aligned parallel (or antiparallel for the TP used here) to each other and perpendicular to the incoming ion beam, and a particle detector. The TP, used in the experiments presented in this thesis, was constructed at the IOQ in Jena [151]. It is equipped with a micro-channel plate detector (MCP) by Scientific Instruments (MCP-Detector S3810-25-I-PS) with a phosphor screen, which is imaged onto a charge-coupled device (CCD) camera. This detector allows data acquisition only limited by the laser's repetition rate or the time to place a target into the laser's focal region. A drawback of the MCP is that it does not provide an absolute number of protons, but a bit-count per camera pixel depending on the detector and camera settings.

To determine the kinetic energy of an ion, it is sufficient to measure the deflection by the magnetic field only, as long as the different ion species are well separated by an electric field. When an ion enters a homogeneous magnetic field ($\vec{B} \parallel \vec{x}$) with a velocity perpendicular to the field lines ($\vec{v} \parallel \vec{z}$), it is deflected by the Lorentz force (Eq. (2.3)) on a circular orbit with the Larmor radius

$$R = \frac{m_i v}{qB} = \frac{\sqrt{2E_{\text{kin}} m_i}}{qB}. \quad (3.1)$$

Here, the classical relation for the ion's kinetic energy $E_{\text{kin}} = m_i v^2/2$ has been used. Since R is larger than the length of the magnetic field region L_B , the ion's deflection along the y -axis at the end of the magnetic field region is $R - \sqrt{R^2 - L_B^2}$. After the ion leaves the magnetic field, it travels ballistically until it hits the detector, which

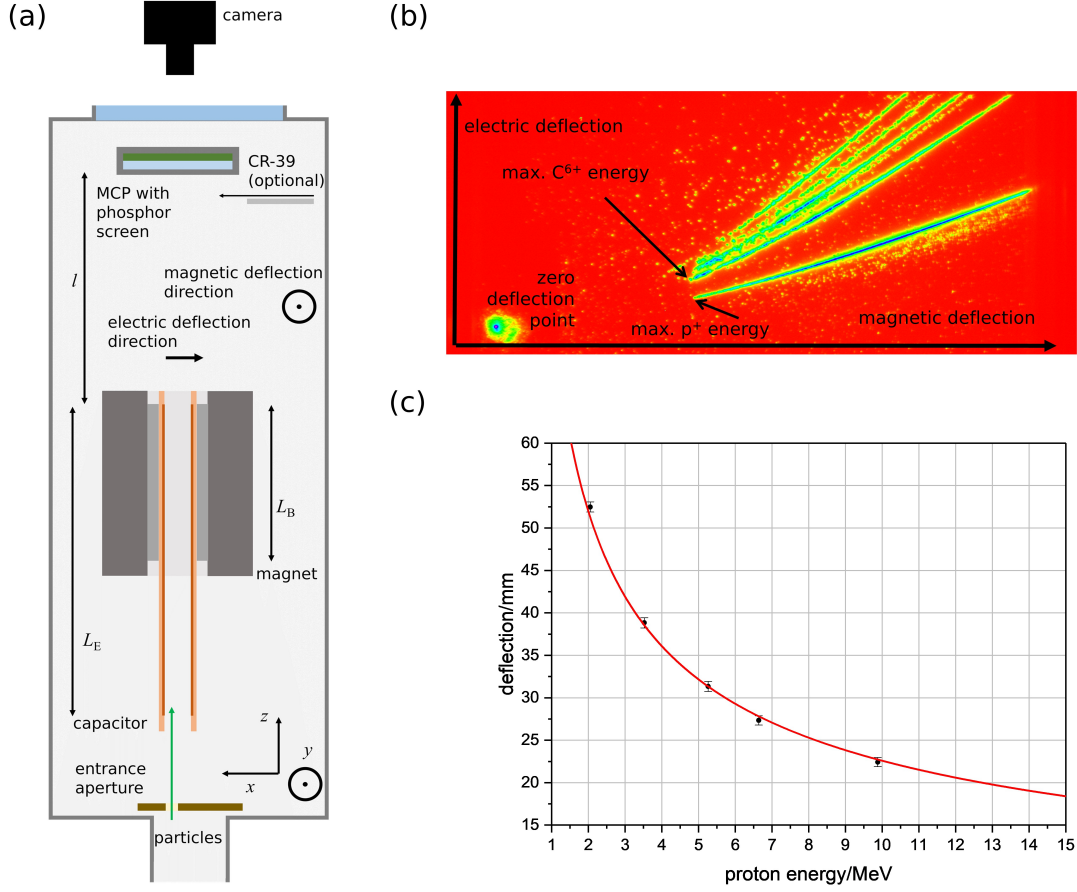


Figure 3.1.: (a) shows the sketch of the used TP (not to scale). (b) shows a false-color image of the MCP's phosphor screen captured during the campaign with the PM for a shot onto a 5 nm thin DLC foil with a circularly polarized laser pulse (see Sec. 3.2.1 for the experimental setup). (c) is the calibration curve for determining the TP's effective magnetic field.

is placed at a distance l to the end of the magnetic field. The total deflection of the ion is then given by

$$y = R - \sqrt{R^2 - L_B^2} + \frac{L_B l}{\sqrt{R^2 - L_B^2}}. \quad (3.2)$$

Eq. (3.2) can be simplified for the case of $R \gg L_B$. When an electric field with strength E and length L_E is applied, the different ion species can be separated. Under the influence of both fields, the different ion species form parabolic traces on the detector's surface, as seen in Fig. 3.1 (b). The protons with the highest kinetic energy have the shortest distance to the zero deflection point, as marked

in the image. The simplified equations describing the positions of the ions on the detector's surface are [150, 152]:

$$y = \frac{qBL_B}{mv} \left(\frac{L_B}{2} + l \right), \quad (3.3a)$$

$$x = -\frac{qEL_E}{mv^2} \left(\frac{L_E}{2} + l \right), \quad (3.3b)$$

$$x = -\frac{m}{q} \frac{E}{B^2} \frac{L_E}{L_B^2} \frac{(L_E/2 + l)}{(L_B/2 + l)} \cdot y^2. \quad (3.3c)$$

If the ion source's size is much smaller than the diameter of the entrance aperture, the energy resolution of the TP is determined by the aperture's projection (diameter s) on the detector's surface. The resolution of the detector for a particular ion energy $E_{\text{kin}}(y)$ is $\Delta E_{\text{kin}}/E_{\text{kin}}(y) = (E_{\text{kin}}(y + s/2) - E_{\text{kin}}(y - s/2))/E_{\text{kin}} \approx 2s/y$ [149].

To assign a proton or ion energy to a measured value of y , it is necessary to determine the magnetic field B . This can be done by measuring y for protons of known kinetic energy. Since protons generated by a laser-driven source are not monoenergetic, it is necessary to filter out a particular energy. The filtering can be realized by blocking protons below a certain energy with aluminum foils of different thickness. As the detector, single CR-39 plastic plates (Tastrack) were used for this purpose inside the TP in front of the MCP [153]. When irradiated by protons, the molecular binding of this polymer is destroyed locally. After etching in hot sodium hydroxide (6.25 molar lye, 85° C), a crater is formed at each point of impact, which can then be detected under an optical microscope.

The threshold energy blocked by the aluminum foil of a certain thickness can be calculated with SRIM [154]. After the irradiation and etching of such a CR-39, one obtains a proton trace with a low-energy cutoff. The distance y between this cutoff and the TP's zero deflection point depends on B .

In Fig. 3.1 (c), y is shown as a function of E_{kin} for five different proton energies corresponding to five illuminated CR-39 detectors. The red line is a fit to this data points with Eq. (3.2) for the values $l = 0.1295$ m, $L_B = 0.1$ m, and the proton's mass and charge. This fit delivers an effective magnetic field strength of $B \approx 0.57$ T.

To obtain an estimate of the number of protons contained in the spectra measured with the MCP (as done for the experiment with droplets for the spectra in Figs. 4.4 and 4.6, see Sec. A.3), the MCP's pixel counts can be compared to the number of proton craters on CR-39 detector plates with a grating structure as used in [155, 156].

The CR-39s used for the water droplet experiment have slits with a width of 3 mm and a grating constant of 6 mm and were placed in front of the MCP.

3.1.2. Measurement of the proton beam profile

Two methods for a qualitative investigation of the proton beam profile were used in the experiments presented in this thesis. First, CR-39 detector plates were placed several centimeters behind the irradiated target. By shielding the CR-39s with aluminum foil of varying thickness, only protons above a certain kinetic energy can damage the CR-39. Additionally, heavy ions are blocked by the aluminum foil. A 15 μm thick aluminum foil blocks carbon ions with $E_{\text{kin}} \leq 17 \text{ MeV}$, oxygen ions with $E_{\text{kin}} \leq 25 \text{ MeV}$, and protons with $E_{\text{kin}} \leq 1.0 \text{ MeV}$ (calculated with SRIM [154]). After etching the exposed CR-39, the proton beam profile becomes visible. In Fig. 4.13 in Sec. 4.5 is a photo of a CR-39 shown together with images of the proton craters taken with an optical microscope. A disadvantage of using CR-39s is that after each exposure, a detector plate has to be replaced by a new, non-exposed one.

The second diagnostic allows for an online measurement of the beam profile for each laser shot and is based on a plastic scintillator [157]. These devices were already successfully implemented in different diagnostics for laser-driven ion acceleration [158, 159]. A scintillator emits light when it is hit by ionizing radiation, like x-ray photons, electrons, protons, or heavy ions. Since in a typical laser-ion acceleration experiment all of these particles are emitted, it is necessary to filter them before they can reach the scintillator or to distinguish between the different scintillator signals. The latter can be done by using the fact that these particles travel with different velocities and reach the scintillator at different times. For example, if a scintillator is placed at a distance of 34.5 cm from the target, hot electrons, x-ray photons, and laser light need 1.15 ns to reach the scintillator, while a proton with a kinetic energy of 2.0 MeV would need 17.6 ns. Note that within this thesis, the energy intervals given to the measured beam profiles were always calculated for the distance between the scintillator's center and the target. For different positions on the scintillator's surface, this distance changes slightly, and so does the time-of-flight for a proton with a given kinetic energy. The scintillator model used here is a BC-422Q (Saint Gobain) with a thickness of 5 mm. The rise time and the decay time of a signal emitted by the scintillator are 110 ps and 700 ps, while the FWHM pulse width of the emitted signal is 360 ps, with a spectrum centered around 376 nm.

Consequently, the signal caused by ions is separated in time from the signal produced by particles traveling with the speed of light. To detect the ion signal, the scintillator was imaged on one (or two) G-CDD camera (4 PICOS, Stanford Computer Optics) with a minimal gate time, i.e., exposure time, of 1 ns. A schematic of this setup can be found in Sec. 3.2.2 in Fig. 3.5. The basic setup is similar for each experiment presented within this thesis. The scintillator is attached to a light-tight housing with an opening aperture of $191 \times 191 \text{ mm}^2$, which is tilted about 20° (downwards for the experiments at POLARIS and upwards for the experiment at JETI) and imaged from behind onto the G-CCD. Due to the tilt, the full horizontal opening angle covered by the scintillator changes slightly as a function of height. Additionally, the vertical opening angle above the horizontal plane differs slightly from the one below. To shield the scintillator from scattered light, low-energy electrons, and heavy ions, its front surface was covered with $15 \mu\text{m}$ thick aluminum foil. To use the TP simultaneously with the proton beam profile measurement, the scintillator has a hole in the center. This hole is connected by a black tube to the TP's vacuum chamber to prevent the G-CCD from direct light exposure through the hole.

To detect protons within a certain energy interval, it is necessary to know the time of the laser pulse's arrival at the target position relative to the electronic trigger signal applied to the G-CCD. This can be done in two ways. If a target is irradiated by the laser, one can search for a strong scintillator signal caused by electrons moving with a velocity close to the speed of light. It is also possible to observe the laser itself on the scintillator when a part of the scintillator is not covered by the aluminum foil. The arrival time of protons with a certain kinetic energy at the scintillator with respect to the electronic trigger signal can be calculated with this zero-point signal.

3.2. Experimental setups

3.2.1. Setup with plasma mirror

The setup in the target chamber for the experiment with a PM and thin foils can be seen in Fig. 3.2. The laser pulses entering the target chamber were focused with a 6° off-axis parabola with a focal length of $f = 90 \text{ cm}$ ($\approx f/6$). For the experimental results shown in this thesis, the PM's surface was positioned about 1.0 cm behind the laser focus. As the PM, substrates with an antireflective coating with residual reflectivity of $R \leq 0.1\%$ were used. A detailed characterization of the PM can be

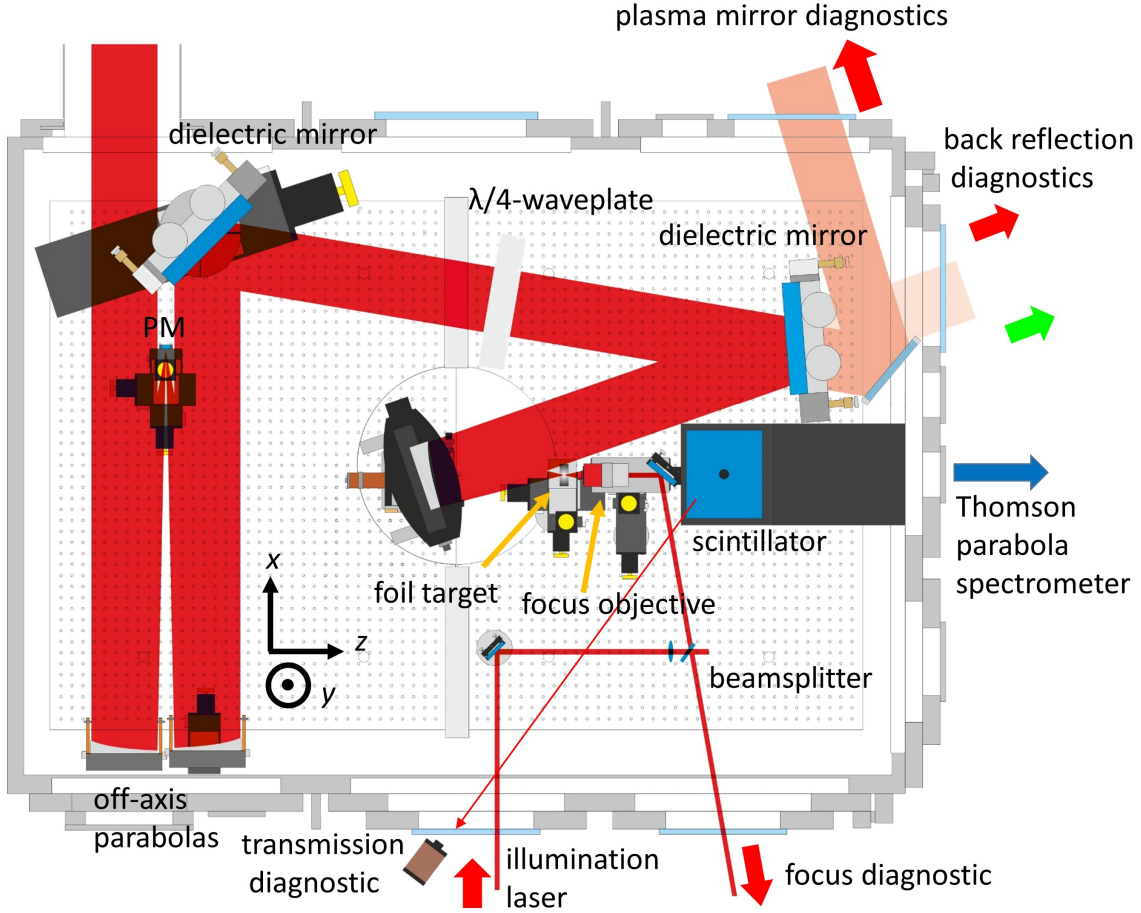


Figure 3.2.: The schematic shows the target chamber with the essential components for the experiment with a PM and DLC foils (not to scale). The setup is described in the main text.

found in [54] with contrast curves in Figs. 45 and 48. After reflection by the PM, the laser pulses were collimated by a parabola of the same type as the first one. To generate circularly polarized laser pulses, a $\lambda/4$ -waveplate could be placed in the beam path, if necessary. Afterward, the laser pulses were focused by a 19° silver, off-axis parabola ($f = 30$ cm, $\approx f/2$) under normal incidence onto the target foils. The full width at half maximum (FWHM) pulse duration in this experiment was around $\tau_L \approx 140$ fs and the focal spot had an area of about $A \approx 8 \mu\text{m}^2$. Within this spot, which contained an energy fraction of $q \approx 0.18$, the laser's intensity was higher than half of its maximum. During this campaign, the laser's intensity was varied by changing the laser pulse's energy.

To detect protons and C^{6+} ions emitted from the DLC foils in laser-forward direction,

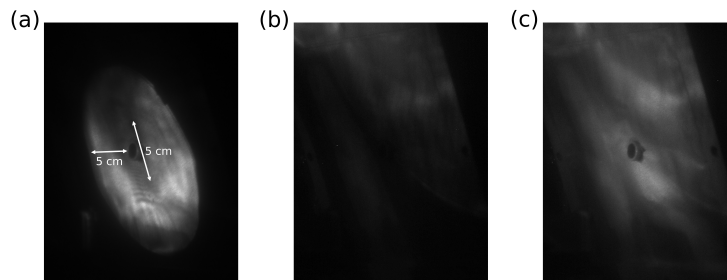


Figure 3.3.: Images captured with the transmission diagnostic are shown (see Fig. 3.2, screen is tilted with respect to the camera). (a) shows the nearfield of the laser for a pulse with an energy of 5 J since no target was placed in the laser’s focus region. (b) shows the background signal for a shot with 8 J onto a 500 nm thin DLC foil, which remains opaque during the interaction. In (c), the transmitted laser light for a shot with 8 J onto a 5 nm thin DLC foil is shown. Note that for (b) and (c), the brightness of the images was increased by a factor of 5 concerning (a) to increase the visibility of the signal on the images.

the TP was used (see Sec. 3.1.1). The distance from the foils to the entrance aperture of the TP in this experiment was about 135 cm, where the distance between the aperture and the MCP was 43 cm. As the entrance aperture, a pinhole with a diameter of $d \approx 0.3$ mm was used. This gives an acceptance angle of the spectrometer of about $\Omega \approx 0.04$ μ sr and a relative energy resolution of $\Delta E_{\text{kin}}/E_{\text{kin}} \approx 0.03$ for protons with $E_{\text{kin}} = 8$ MeV. The plastic scintillator (tilted downwards by 20° , see Fig. 3.5), together with one G-CCD, was installed in the setup (see Sec. 3.1.2).

The aluminum foil, which covered the scintillator’s front surface, was imaged onto a filtered CCD camera to detect the directly transmitted laser light. Three images captured with this diagnostic are presented in Fig. 3.3. In Fig. 3.3 (a), no target was present in the focal region. In Fig. 3.3 (b) the “background” signal is shown. Here, a 500 nm thin DLC foil was placed at the laser’s focus position. This foil did not become transparent during the time of interaction with the laser pulse. The background signal is likely a consequence of weak laser reflections on rear surfaces of optics (back surface of PM, debris shieldings in front of the focusing parabolas, ...). For a 5 nm thin foil (Fig. 3.3 (c)), a fraction of roughly $T \approx 0.11$ of the laser pulse was transmitted.

The light that was reflected from the target and collimated by the parabola was partly transmitted through a dielectric mirror. Outside the target chamber, a screen was placed in the path of the transmitted light. This screen was imaged onto two different CCD cameras filtered to 1ω and 2ω . Images captured with these back

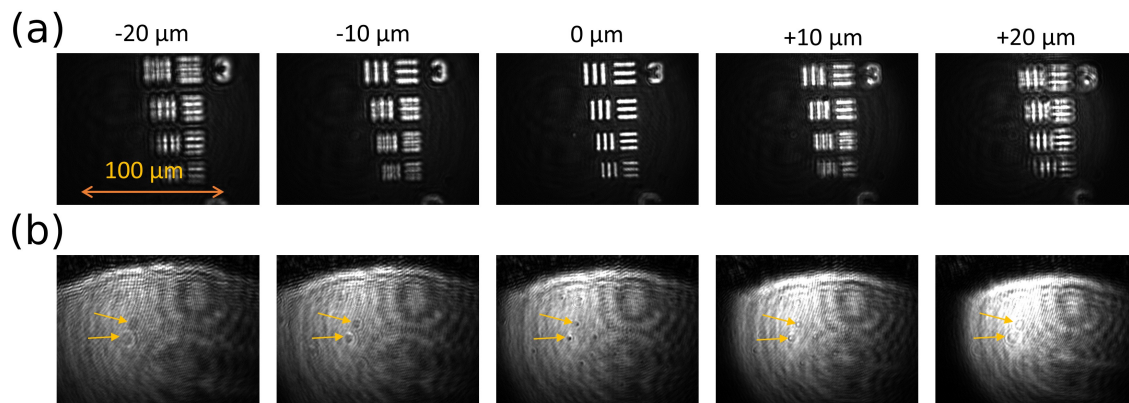


Figure 3.4.: (a) shows images of a USAF 1951 test target (seventh group, third to the sixth element) captured with the focus diagnostic. The test target was moved in steps of $10\ \mu\text{m}$ along the z -axis. (b) shows images of a $20\ \text{nm}$ thin DLC foil. The upper curved edge is the target holder. The orange arrows point to small dust particles on the foil surface.

reflection diagnostics are shown in Fig. 3.8.

To image the laser's focus onto a CCD camera outside the target chamber, an objective with a focal length of $f_1 = 50\ \text{mm}$ ($\approx f/1.2$) was used. This objective was later replaced by an objective with $f_2 = 10\ \text{mm}$ ($\approx f/1.25$) and an additional 3-inch lens with $f_L = 50\ \text{cm}$, the latter being placed outside the target chamber.

The focus diagnostic could also be used to determine the position of a target foil relative to the laser focus along the laser-forward direction (z -axis). That was realized by coupling a CW-laser, with a wavelength of $1030\ \text{nm}$, with a beamsplitter into the path between the focus objective and the camera. Consequently, the foil's rear surface was illuminated and could be imaged through the focus objective prior to the actual interaction. For uniform illumination of the foil, it is necessary to separate the CW-laser's focus position from the position where a sharp image of the foil is produced. Hence, the divergence of the CW-laser had to be adjusted with an additional lens. Images taken with this diagnostic are shown in Fig. 3.4. To get an impression of the image quality of this diagnostic, a test target was used (USAF 1951, Fig. 3.4 (a)). The elements of the target's seventh group below the third element were imaged. The target was moved in steps of $10\ \mu\text{m}$ along the z -axis. For $z = 0\ \mu\text{m}$ all the lines and the number of the third element are sharp. The linewidth of the smallest lines is $2.2\ \mu\text{m}$. The structures became blurry when the target was moved out of this position in steps of $10\ \mu\text{m}$ in both directions. Fig. 3.4 (b) shows images of a $20\ \text{nm}$ thin DLC foil. Since such foils do not have regular structures,

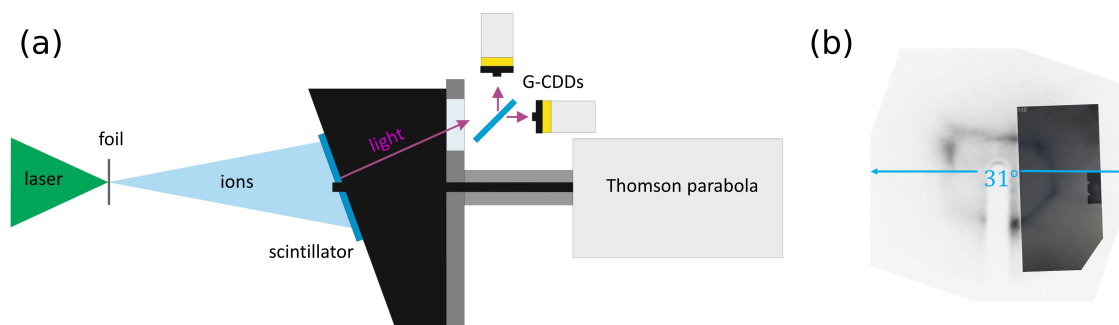


Figure 3.5.: In (a), a sketch of the ion diagnostic setup is shown (not to scale). In (b), the beam profile of protons with $E_{\text{kin}} \geq 1.0$ MeV, which were accelerated from a 100 nm thin plastic foil, is presented. The left part of the beam profile was measured with the scintillator and the G-CDD, while for the measurement of the beam’s right part, a piece of CR-39 was put directly in front of the scintillator. High proton flux is displayed darker for both detectors.

the sharpness of small dust particles present on the foil surfaces was used to determine a foil’s position with an accuracy of $\Delta z \approx \pm 10 \mu\text{m}$. This is comparable to the Rayleigh length of the laser of $z_{\text{R}} \approx 10 \mu\text{m}$.

3.2.2. Setup with frequency-doubled laser pulses

To significantly improve the TIC of the laser pulses, they were frequency-doubled with a KDP crystal to a spectrum centered around 515 nm. A detailed description of the entire setup with a characterization of the 515 nm-pulses can be found in [123, 160]. To filter out the remaining fundamental from the main beam path, two dichroic mirrors were positioned between the KDP crystal and the focusing parabola. The linearly polarized laser pulses had an energy of $E_{\text{L}} \approx 2.8$ J and a pulse duration of $\tau_{\text{L}} \approx 135$ fs. For focusing these pulses under normal incidence onto a foil, a 19° silver, off-axis parabola with $f = 30$ cm ($\approx f/2$) was used. $q \approx 40\%$ of the laser pulse energy was contained within a spot of size $A \approx 9 \mu\text{m}^2$. This yields an approximate intensity within the focal spot of $I \approx 9 \cdot 10^{19}$ W/cm² corresponding to $a_0 \approx 4.2$ (Eq. 2.7).

For the investigation presented in this thesis, the beam profiles of proton distributions emitted from plastic foils with thicknesses between 100 nm and 800 nm were examined.¹ A sketch of the setup is shown in Fig. 3.5 (a). To measure the proton beam profile, the combination of plastic scintillator and G-CDD, as described

¹The foils were produced within the SFB-TR 18 by the group of J. Schreiber, LMU Munich.

in Sec. 3.1.2, was used. Here, the scintillator's rear surface was imaged onto two G-CCD cameras. The distance between the scintillator's center and the laser's focus position was 34.5 cm. Hence, the scintillator covered a full horizontal opening angle of $\approx 31^\circ$. The settings of one G-CCD were adjusted to measure the beam profile for protons with $E_{\text{kin}} \geq 1.0$ MeV. An example of such a beam profile can be seen in Fig. 3.5 (b). Here, one part of the beam profile was measured with the G-CCD, and the right, smaller part was measured with a CR-39 detector, shielded with a 15 μm thick aluminum foil, for a single shot to verify the scintillator signal. The second G-CCD was used to measure the beam profile formed by protons of different energy intervals (see Fig. 3.10).

The physical origin of this ring-like proton beam profile will be discussed in Sec. 3.4. As a supporting measurement, the maximum proton energy emitted in the laser's forward direction was measured with the TP (see Sec. 3.1.1). To position the target foils with respect to the laser's focus position, they were imaged on the same CCD camera with the same objective as the laser's focus (see Sec. 3.2.1 for a description). In contrast to the experiment with the plasma mirror, the plastic foils were illuminated in transmission with a CW-laser at 532 nm, and an objective with a focal length of $f = 20$ mm ($\approx f/1.8$) was used.

3.3. Ion acceleration with nanometer thin foils

Although laser-driven proton acceleration has seen a lot of research during the last two decades, the maximum proton energy of about 60 MeV achieved in the first experiments [1, 2] has only been increased to values between 85 MeV and 100 MeV during that time period [9, 42, 47, 161].

A possible path to higher ion energies is described by the acceleration of ions via RPA from few nanometer thin foils (see Sec. 2.4.3). Experiments with Ti:sapphire laser systems with pulse durations of 30 fs and 45 fs reported a significant increase of the ion energies for foil thicknesses between 5 nm and 20 nm compared to thicker foils [45–48]. Kim *et al.* [47] and Scullion *et al.* [48] measured a significant enhancement of the ion energies when using circular polarization (CP), while Henig *et al.* [45] observed a significant increase only for linear polarization (LP). For LP, Scullion *et al.* [48] measured only a weak thickness dependence, while Kim *et al.* [47] measured a significant thickness dependence with a lower increase of the maximum proton energy than for the case of CP. Kim *et al.* [46, 47] measured the maximum

proton energies also as a function of the intensity for the thinnest foils. They found either a linear [46] or a quadratic scaling of the proton energies [47]. In all of these experiments, a DPM was used for the enhancement of the TIC.

In an experiment performed at the VULCAN laser with a pulse duration of 700 fs and a single PM, 15 shots were performed on foils with thicknesses between 5 nm and 500 nm [162]. In contrast to the previously mentioned experiments, no difference between CP and LP could be observed except for the 5 nm thin foil for which CP yielded an enhancement and LP a reduction of the maximum proton energies. For the foils between 10 nm and 100 nm, no thickness dependence of the maximum proton energy was found, while 500 nm yielded a slightly lower proton energy. The authors stated that the accelerated ions gained most of their energy during the phase of relativistic transparency.

Due to limitations of the laser pulse energy and thus the intensity (see Sec. A.2), POLARIS is not able to produce proton energies as high as mentioned in the first paragraph. However, because of the higher repetition rate when compared to laser systems like PHELIX or VULCAN [9, 51, 52, 162], it is possible to investigate the behavior of the maximum ion energies for a comprehensive parameter scan with laser pulses with a pulse duration of more than 100 fs. In this parameter scan, the target thickness was varied between 5 nm and 500 nm, LP and CP were used, and the laser energy was varied. Such a parameter scan may pave the road to higher ion energies or reveal obstacles that have to be overcome to reach higher ion energies and was not yet done for laser pulses with $100 \text{ fs} < \tau_L \ll 500 \text{ fs}$ (see Fig. 9 in [53]).

3.3.1. Results

In this section, the dependencies of the maximum proton and carbon ion energies on the laser's pulse energy E_L , the foil thickness d , and the polarization are presented. Fig. 3.6 (a) shows the measurements for LP and $d = 500 \text{ nm}$, 50 nm , 5 nm , while (b) displays the maximum ion energies for CP and $d = 100 \text{ nm}$, 10 nm , 5 nm as a function of the laser's pulse energy. The energy axis represents the total energy contained in a laser pulse impinging on a foil. However, the energy within the area where the intensity is higher than half of the maximum was about one-fifth of these values. The graphs are displayed on a double logarithmic scale. The trend lines are thus power functions. If only the proton energy is displayed for a laser shot of a certain energy, then no significant carbon signal could be detected for this shot.

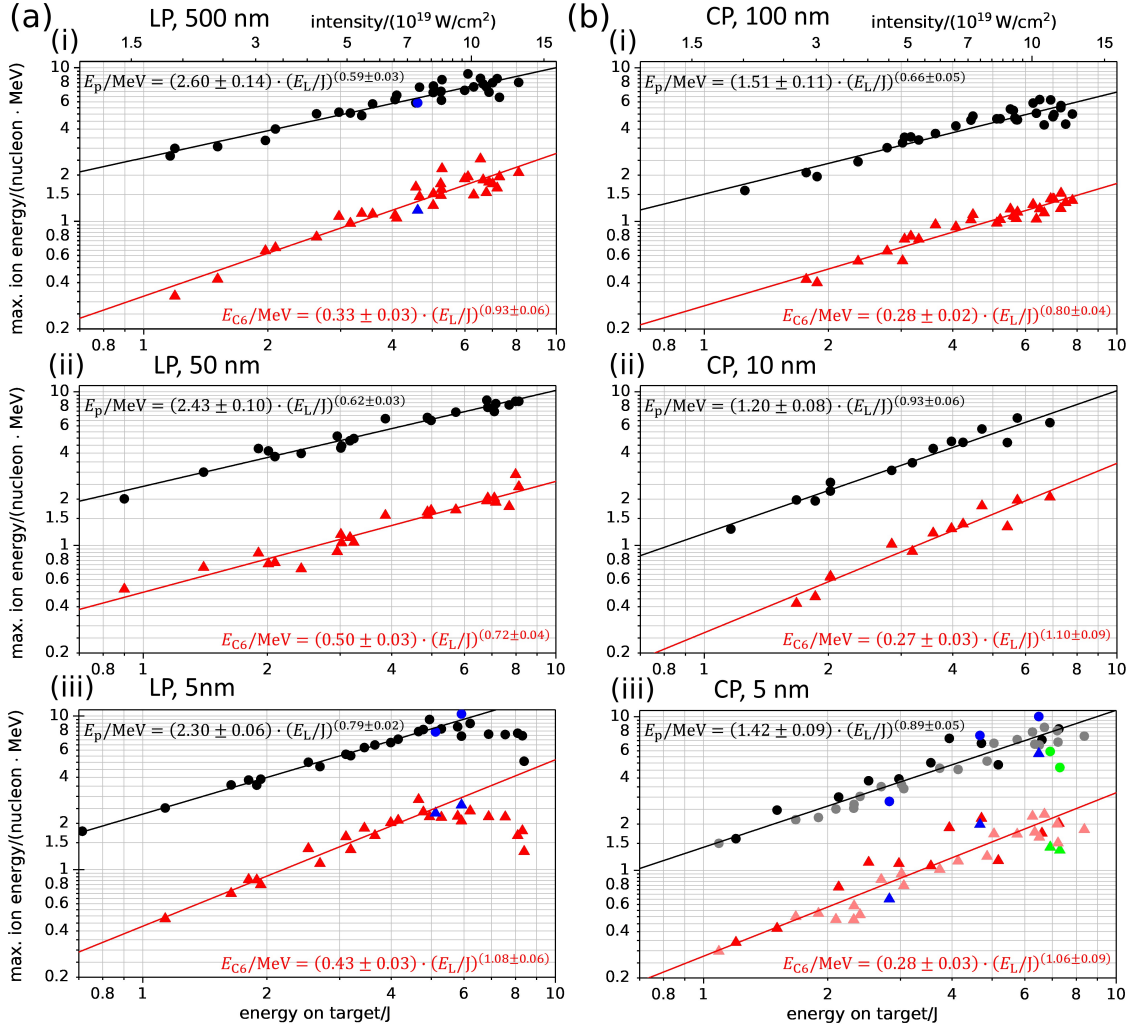


Figure 3.6.: The figure shows the maximum ion energies as a function of the laser energy for LP (a) and CP (b) for different foil thicknesses. The black dots are the maximum proton energies, and the red triangles are the maximum C⁶⁺ energies per nucleon. The average intensity, given in the top horizontal axis of the two upper graphs, was calculated for a pulse duration of ≈ 140 fs and a focal spot with size $\approx 8 \mu\text{m}^2$ that contains $\approx 18\%$ of the pulse energy. Note that for (b_{iii}), the data was obtained on two different days and is thus distinguished by color. For the circles and triangles in green and blue, additional information is provided in Fig. 3.8 and in the main text.

For the 500 nm and the 50 nm thin foils (LP, (a_i) and (a_{ii})), the measured maximum proton energies as a function of the pulse energy are similar yielding identical trendlines. The exponent of $b \approx 0.6$ is close to the square root scaling for TNSA when the ponderomotive scaling of the electrons' temperature is assumed (see Sec.

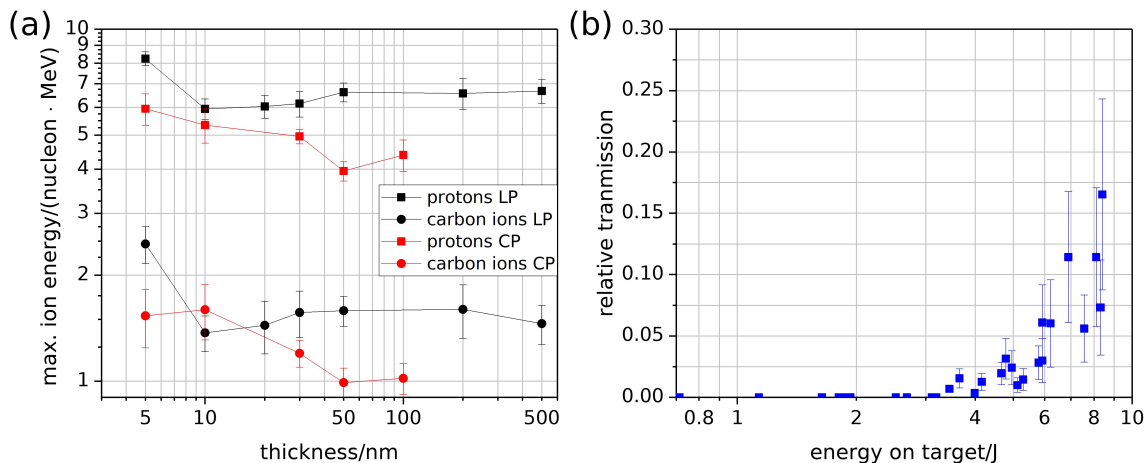


Figure 3.7.: (a) displays the maximum proton (squares) and carbon ion energies (circles) for LP (black) and CP (red) as a function of the foil thickness. The ion energies correspond to the values given by the trendlines in Fig. 3.6 for $E_L = 5$ J. (b) shows the relative transmission of laser light for the 5 nm thin foil and LP as a function of E_L .

2.4.1.2). Steeper scalings than the square root scaling can also be explained within the context of TNSA (see Sec. 2.4.1.4). The energies of the fastest carbon ions are also similar for $E_L > 3$ J. The steeper trendline for 50 nm (a_{ii}) compared to 500 nm (a_i) is thus a result of the measurements below 3 J. A possible explanation for the steeper scaling of the carbon ions compared to the protons, as seen in all six graphs in Fig. 3.6, could be that the carbon ions undergo a longer acceleration process since they are slower than the protons and stay longer in the region of the accelerating field. However, they are accelerated in a weaker electric field because they are shielded by the proton population ahead. The final carbon energy per nucleon is thus a factor of ≈ 4 lower than the maximum proton energy, for $E_L \approx 6-8$ J, instead of the factor of 2 if both populations would see the same electric field over the same acceleration distance. The protons, on the other hand, may leave the field region before the electric field decays (see Sec. 2.4.1.4, reference time τ_0 in Eq. (2.42)).

A significant difference to the thicker foils was measured when using a 5 nm foil (Fig. 3.6 (a_{iii})). Up to $E_L \approx 5-6$ J, both trend lines exhibit a steeper scaling for this foil thickness. Additionally, in Fig. 3.7 (a) are the maximum proton energy (squares) and the carbon energy (circles) plotted as a function of the foil thickness for $E_L = 5$ J. It can be seen that for LP (black), both are significantly higher for the 5 nm thin foil compared to the otherwise similar values for all the other foil thicknesses. Such

thickness independence, except for the thinnest foil, was observed in [162], as written in the introduction of this section. The thickness of 5 nm corresponds roughly to the optimal foil thickness for LS-RPA (Eq. (2.51)) for an intensity of $\approx 1 \cdot 10^{20}$ W/cm². As written in Sec. 2.4.3.2, this optimal foil thickness corresponds to the threshold of relativistic transparency.

For increasing laser energy ($E_L \gtrsim 6$ J), the ion energies stop to increase for the 5 nm foil (Fig. 3.6 (a_{iii})) until they are similar or slightly below the energies obtained with the other two thicknesses for $E_L \approx 8$ J as seen in Fig. 3.6 (a). Here, a correlation to the onset of laser transmission around 5–6 J can be seen as displayed in Fig. 3.7 (b). The significant light transmission indicates that the plasma became underdense during the interaction, which may have led to a less effective ion acceleration process for the conditions in this experiment. That significant transmission of laser light correlates with reduced maximum proton energies was also observed in [42].

A weak dependence of the maximum ion energies on the target thickness was also observed by Poole *et al.* [53]. In that experiment, the angle of incidence of the p-polarized laser pulses was 45°. A single PM was used, and the laser pulses were focused onto a liquid crystal target with thicknesses between $d > 1$ μ m and $d \approx 10$ nm. The accelerated ions were detected under the target's normal direction. Between $d = 300$ nm and thinner foils, the ion energies stayed relatively constant except for $d \approx 10$ nm that yielded higher energies, but also larger shot to shot fluctuations. For $d > 1$ μ m, the energies were about 50 % lower. Poole *et al.* interpreted the weak thickness dependence in the context of TNSA. The target thickness influences the maximum proton energies due to a change in the electron density as a consequence of the electron divergence (see Sec. 2.4.1.1). For a target thickness variation much smaller than the focus size, this effect is small, as estimated below. For $d < 40$ nm, they also measured an increase in the amount of transmitted light. However, they state that the fluctuations of the transmitted light did not correlate strongly with the fluctuations of the maximum proton energy or the spatial distribution of the protons with low kinetic energy.

Since the generation of hot electrons should be reduced for the investigation of RPA (see Sec. 2.4.3), the POLARIS laser pulses were converted to CP. In Fig. 3.6 (b), the dependence of the maximum ion energies as a function of E_L for the thicknesses $d = 100$ nm, 10 nm, 5 nm is presented, whereas in Fig. 3.7 (a) the maximum ion energies for $E_L = 5$ J as a function of the foil thickness are plotted (red squares and circles for CP). The use of CP has led, in general, to a reduction

in the maximum ion energies compared to the case of LP, especially for the thicker foils ($d = 50$ nm, 100 nm). That indicates that the generation of hot electrons, essential for the effective acceleration via TNSA, was indeed reduced. When the foil thickness is decreased for CP, the maximum ion energies increase continuously. For the thinnest foils, the maximum ion energies exhibit a steeper scaling with E_L , as shown in Fig. 3.6 (b_{ii}) and (b_{iii}) compared to (b_i). Within this thickness scan, the shots with the highest ion energies for CP were obtained with the 5 nm thin foil. Note that two shots below the trendline are marked green. For these points, a significant amount of transmitted laser light was measured ($T \approx 0.04$ and $T \approx 0.06$). Consequently, these points were not included in the determination of the trendlines.

A decrease of the maximum proton energy when changing the polarization from LP to CP was measured, for example, by Dollar *et al.* [163]. When decreasing the foil thickness from 1 μ m to 30 nm, they observed that the values measured with CP approached the ones obtained with LP, whereas the absolute achieved maximum energies were similar for the thinnest foils. For LP, on the other hand, they measured only a slight thickness dependence. In addition to the accelerated ions, they also measured the accelerated electrons. For the 100 nm thick foil, they observed a reduced hot electron generation for CP when compared to LP, while for $d = 30$ nm, the hot electron spectra were similar. With the help of simulations, they stated that the deformation of the thin targets led to an increased electron heating that resulted in an enhancement of ion acceleration via TNSA for CP.

Besides the main measurements of the maximum ion energies and the supporting measurements of the light transmission, additional measurements of the reflected light at 1ω and 2ω , as well as measurements of the proton beam profile, were performed. For the six shots marked in blue in Fig. 3.6, images of these diagnostics together with images of the ion traces are shown in Fig. 3.8. Concerning the position or shape of the back reflections, no significant, general correlation could be found to the (mostly small) fluctuations in the maximum ion energies. In other words, a shot with a shifted or deformed reflection pattern did not necessarily produce a maximum proton or carbon ion energy below the trend lines. Such a shifted or distorted reflection may indicate that the foil in the region where the focus was incident was possibly rippled. Poole *et al.* [53] also mentioned that they did not observe a strong correlation between the quality of the reflections and the measured maximum proton energies.

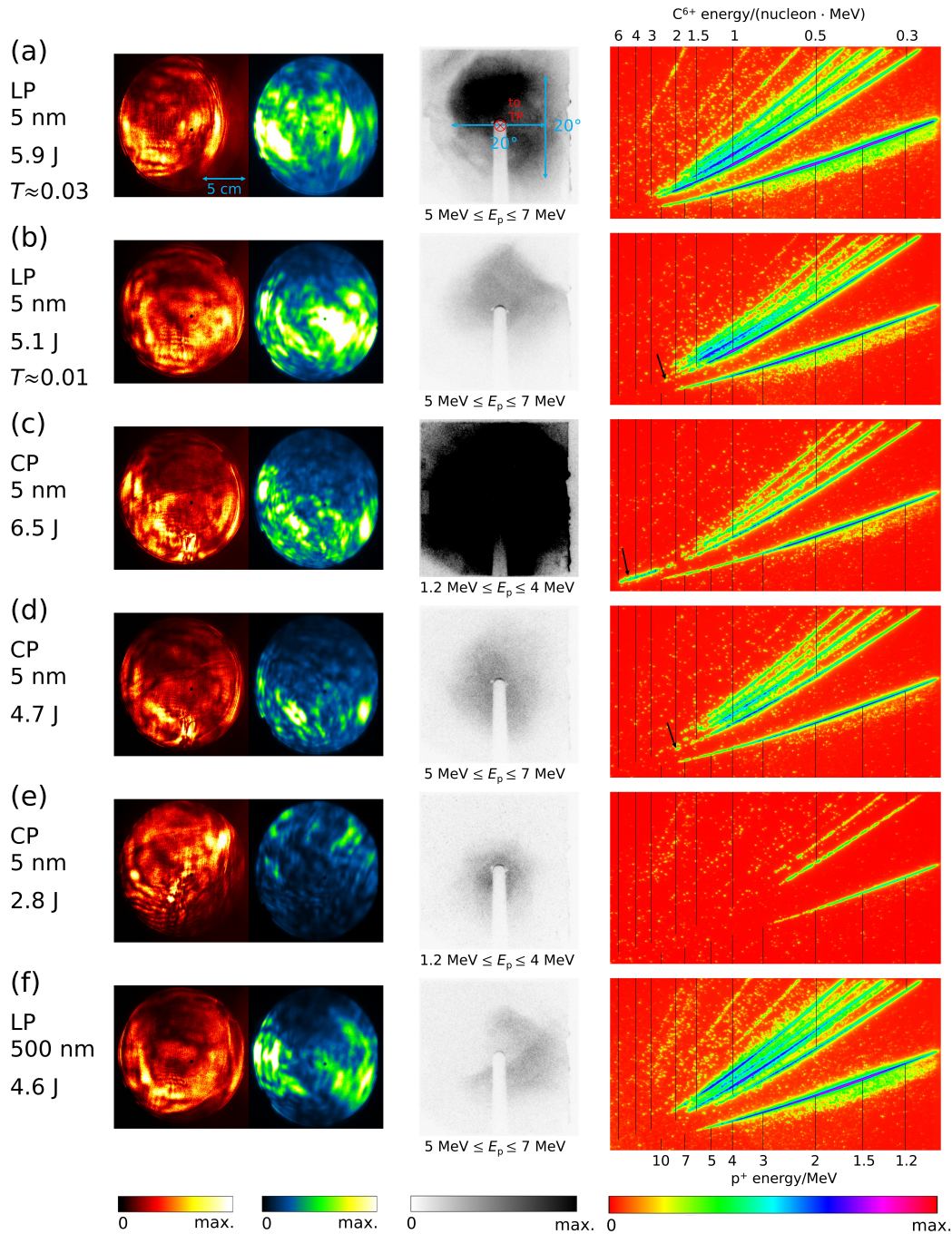


Figure 3.8.: The figure shows images of the different diagnostics for the shots marked in blue in Fig. 3.6. The two images on the left are the back reflections from the targets at 1ω (first) and 2ω (second). In the center, the proton beam profiles are presented for the energy interval indicated underneath. The images on the right are the ion traces obtained with the TP. The black lines mark the position of specific proton and carbon energies. The pixel counts of the back reflections of (e) were increased by a factor of 2 to increase visibility.

Examples for shots with shifted/distorted back reflections are given in Fig. 3.8 (a) and (d). (a) is the shot with the highest maximum proton energy for LP and $d = 5$ nm (Fig. 3.6 (a_{iii})), although both reflections are shifted compared to, for example, (b). An example of a shot for which shifted/distorted back reflections coincide with reduced maximum ion energies is (d) for $d = 5$ nm and CP (Fig. 3.6 (b_{iii})). For this shot, the maximum proton and the maximum carbon energy are below the trendline. Both reflections are distorted upwards compared to the reflections seen in Fig. 3.8 (c) and (d).

Also, between the position of the scintillator signal's maximum and the maximum ion energies, there exists no significant, general correlation. In other words, if the maximum proton signal does not overlap with the entrance of the TP's vacuum chamber, this does not necessarily mean that the maximum proton energy is below the trend line. An example is again the shot with the highest proton energy for LP, shown in (a). The region of the strongest/saturated signal is shifted vertically and does not enter the TP. Nevertheless, it cannot be excluded that the "global" maximum proton energy was higher for this shot than the maximum measured with the TP. Likewise, a more homogeneous or central scintillator signal does not necessarily mean that the measured proton energy is above the trend, as is the case for the shots shown in (b) and (e). However, there are shots with a central, homogeneous beam profile and a proton energy above the trend line, like (d). Similarly, an off-axis beam profile, like in (f) ($d = 500$ nm, LP, scan in Fig. 3.6 (b_i)) can coincide with a lower maximum proton energy.

As the signal strength of the scintillator signal is proportional to the number of protons, it correlates with the signal strength of the proton trace measured with the TP. The stronger scintillator signal close to the TP's entrance in (a) correlates with a stronger MCP signal on the corresponding part of the proton trace in comparison to the weaker signals in (b). Note that the signal strength of the scintillator signal shown in (a) and (b) cannot be compared to the other shots shown due to different settings for the energy interval or/and amplification of the G-CCD.

A unique shot is shown in Fig. 3.8 (c). This shot shows a strong carbon ion signal separated and ahead of the main ion trace (black arrow). As can be seen in Fig. 3.6 (b_{iii}), this separate trace yields a maximum carbon energy more than twice as high as for any other shot in this campaign. Unfortunately, the G-CCD was set to a low proton energy interval and too high gain for this shot. Consequently, the measurement is fully saturated. In contrast to such an extended, separated

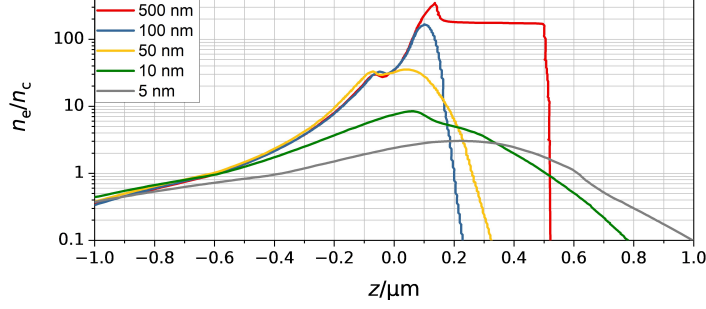


Figure 3.9.: The plasma profiles simulated with MULTI-fs for the different foil thicknesses are shown. Note that the targets are not fully ionized. Hence, the maximum electron densities are below the value of a fully ionized target. The data for the figure was provided by S. Keppler [165].

trace, the carbon traces of many shots exhibit fragmented signal near the maximum energy, for example, the maximum carbon energies marked by the black arrows for the shots shown in Fig. 3.8 (b) and (d). Such fragmented carbon traces are not exclusive to the thinnest foils but were often observed over the entire campaign for various experimental settings. Extended carbon features like the one shown in (c) were, for example, observed in [45, 46, 48, 163] for very thin foils ($d = 5\text{--}30$ nm) and interpreted in the context of RPA.

As a step towards the interpretation of the thickness dependence of the maximum ion energies, hydrodynamic simulations with the code MULTI-fs were performed.² The simulated one-dimensional density profiles for the thicknesses 500 nm, 100 nm, 50 nm, 10 nm, and 5 nm are shown in Fig. 3.9 when the intensity of 10^{17} W/cm² is reached since MULTI-fs is not suited to simulate interactions at relativistic intensities [146]. The peak intensity of the linearly polarized, simulated pulse was $1 \cdot 10^{20}$ W/cm² with a pulse duration of 140 fs. More information about the simulations can be found in [164].

For all thicknesses, the front side has expanded, with the critical density being located at $z \approx -0.6$ μm ($z \approx -0.4$ μm for $d = 5$ nm). With decreasing foil thickness, the plasma density gradient at the rear side increases, whereas a foil's maximum plasma density decreases. The roughly constant maximum ion energies for LP (Fig. 3.7 (a), black) might be due to this target expansion. For TNSA, the electric field is proportional to the square root of the hot electron density (Eq. (2.34)) that is

²The simulations were performed by Sebastian Keppler and Mathis Nolte. The input data for carbon was provided by Rafael Ramis, and the input parameters for the simulations were chosen according to his recommendations.

inverse proportional to the square of the electron sheath's radius (Eq. (2.31)). With the focus' radius $r \approx 1.6 \mu\text{m}$ and a full divergence angle of $2\theta \approx 40^\circ$, the difference in the electric field due to the electron divergence for the two foil thicknesses of 50 nm and 500 nm can be estimated as $\approx 10\%$. If one uses, instead of the unexpanded foil thicknesses, the distance between the two positions where the critical density is reached, then this enhancement is reduced to $\approx 5\%$. Additionally, the plasma may expand further from the target's rear surface until the main pulse arrives, which is not beneficial for TNSA.

As one can see in Fig. 3.6 and Fig. 3.7 (a), the highest maximum ion energies were obtained with the 5 nm thin foil. Before the arrival of the main pulse, the simulated 5 nm foil has expanded into a 1 μm wide, near-critical plasma (Fig. 3.9, 5 nm (grey)). That the target was no longer in its initial form in the experiment can be seen by calculating the optical skin depth for the fully ionized carbon foils (Eq. (2.22)) that is $\delta(n_e = 600n_c) \approx 7 \text{ nm}$. Due to this skin depth, transmitted laser light should have been detected for these foils even at low laser pulse energies (see Fig. 3.7 (b), $E_L \lesssim 4 \text{ J}$). However, the opacity of the foil can be explained by its expansion. For a plasma density of, e.g., $n_e \approx 2n_c$, the skin depth is $\delta(n_e = 2n_c) \approx 170 \text{ nm}$, which is much smaller than the simulated extension of the expanded plasma with a higher density (Fig. 3.9, 5 nm (grey)). The increased light transmission with increasing laser energy can be the result of a reduced plasma density on the propagation axis of the laser since the PF of the laser can push electrons out of its path transversely in an experiment. Another possibility is that the laser's PF compresses the plasma along the propagation axis in a way that light can tunnel through the remaining plasma. A third possibility is that the electrons in the laser's path may be heated, and the plasma becomes relativistically transparent (see Sec. 2.3.1.2). In any case, it seems that the onset of transparency correlates with experimental conditions that are not beneficial for ion acceleration, as seen in Fig. 3.6 (a_{iii}) and Fig. 3.7 (b).

However, up to this onset of transmission, the 5 nm foil (Fig. 3.6 (a_{iii})) shows a steeper increase of the maximum ion energies than the thicker foils ((a_i) and (a_{ii})). This steeper scaling was also measured for the thinner foils and CP (Fig. 3.6 (b_{ii}) and (b_{iii})). As a consequence of the thin foils' expansion, there might be different approaches for an explanation of the increase in ion energies. Firstly, the overall low plasma density of the expanded thin foils enables the laser to penetrate deeply into the plasma that might lead to volumetric heating of plasma electrons. On the other hand, due to the reduced plasma density, HB-RPA might become important as an

acceleration process for the ions (see Sec. 2.4.3.1). Also, a combination of HB and further acceleration via TNSA may be possible. The effectiveness of the latter may be increased by the compression of the plasma by the laser, which might counteract the negative effect of an extended plasma density gradient.

3.4. Ring-like proton beam profile

In this section, the spatial profile of proton beams, generated during the interaction of high-intensity laser pulses with thin plastic foils, was investigated to gain a deeper understanding of the physics involved. This understanding is a prerequisite for improving the control over laser-driven proton beams, which is necessary when one wants to use them for applications, like hadron therapy or as an ultra-short pulse front-end for conventional accelerators [33–41].

When using submicron foils as targets, various ion acceleration mechanisms may play a role that have not yet been fully understood, especially those that are expected to be dominant for thin foils, like BOA or RPA (see Sec. 2.4). Therefore, it is necessary to clearly distinguish between different acceleration mechanisms when investigating laser-driven proton acceleration. For this purpose, it is advantageous to identify significant characteristics of the proton beams that can be assigned to a particular mechanism and fully explained within its context. The proton beam’s spatial characteristics are of special interest since they are also relevant for the transport of the accelerated protons to subsequent applications.

The proton beam feature investigated in this section is a stable ring-like structure (RLS) formed by protons with “low” kinetic energies. Since this is an often observed feature in experiments, it is significant for laser-accelerated proton beams. Important experiments in which such a RLS was observed for micrometer- and nanometer-thin foils are listed below.

In an experiment performed at the VULCAN laser facility ($E_L \approx 50\text{--}100\text{ J}$, $\tau_L \approx 1\text{ ps}$), a RLS was detected for different target materials and $25\text{ }\mu\text{m} \leq d \leq 1000\text{ }\mu\text{m}$ [166]. The RLS, oriented around the target’s normal direction, was explained for experiments with $125\text{ }\mu\text{m}$ thick aluminum foils as a consequence of magnetic fields forming within the target [3]. The protons forming the RLS were initially interpreted as originating from the foil’s front surface (laser-illuminated side). When traveling through the aluminum foil, these protons would be deflected in a RLS by the mag-

netic field. The measurements were reproduced with a 100 μm thick foil [167]. In both experiments, also protons with higher energies were deflected in a RLS, with its opening angle decreasing for increasing proton energy. Low-energy protons expanding from the laser-illuminated side in backward direction also formed such structures, which was attributed to magnetic fields within the expanding plasma [4].

At the GEKKO MII laser (25 J, 0.45 ps), RLSs were emitted from plastic foils with thicknesses of 5 μm , 25 μm , and 100 μm [168]. Murakami *et al.* suggested that the protons were accelerated from the foils' rear surface and deflected by a toroidal magnetic field located outside the target generated by hot electrons.

In an experiment at the LULI laser system (15 J, 0.35 ps) with 1–3 μm thick plastic foils, the RLS was attributed to the PF's radial component acting close to the region of the critical density [169]. In different experiments at LULI and at the THOR laser system (0.4 J, 42 fs), the RLS was observed with 25 μm thin aluminum foils and 10 μm thin gold foils coated with a 1 μm thin chrome layer [170]. The authors interpreted the RLS as a consequence of a “bell-shaped” electron sheath that sets up the electric field, which accelerates protons.

Recent observations of the RLS were made with submicron thin foils when investigating other acceleration mechanisms besides TNSA. At the TRIDENT laser (80 J, 550 fs), the RLS was especially pronounced for ≈ 190 nm thin DLC foils [171]. Here, the main focus was put on the acceleration of carbon ions, and it was measured that also ions with high kinetic energy are forming this RLS. The results were interpreted in the context of relativistic transparency and the RLS as a signature of the breakout-afterburner acceleration mechanism.

Several measurements with thin foils were done recently at the VULCAN laser ($\lesssim 200$ J, $\lesssim 1$ ps). In [172], the RLS was observed for 10 nm and 40 nm thin aluminum foils, and the orientation of the RLS was determined to be centered around the target normal direction, as in the experiments with micrometer thin foils. In measurements performed with aluminum foils of thicknesses between 10 nm and 400 nm, the RLS was detected for thicknesses of ≤ 200 nm [173]. The RLS's full opening angle as a function of the foil thickness d was found to increase from $d = 10$ nm to $d = 80$ nm and to decrease slightly for thicker foils. In supporting simulations, they found that the opening angle increased for $d = 20$ nm to $d = 40$ nm and then continuously decreased for thicker foils. Padda *et al.* [173] interpreted the RLS as a result of the interaction between the aluminum ions and the protons when the target becomes relativistically transparent. Here, aluminum ions accelerated by RPA

should exert a force on the protons, which causes the formation of a ring. In another experiment with DLC foils, the RLS was measured to be present for all thicknesses used (5–500 nm), whereas the opening angle of the RLS was thickness-independent [162].

The multitude of observations for several laser and target parameters identify the RLS as a central feature of laser-driven proton acceleration. Since there exist individual explanations for the different measurements, further investigations of this feature are necessary to deepen the understanding of laser-driven proton acceleration.

Consequently, a detailed investigation with submicron plastic foils with experiments and simulations was performed. The second harmonic of the POLARIS system was used to exclude the influence of extended pre-plasmas or foil transparency by a significant rising edge or pre-pulse. Finally, the RLS could be explained with a simple model within the TNSA framework.

3.4.1. Experimental results

The experimental setup in the target chamber is presented in Sec. 3.2.2, with a sketch of the setup displayed in Fig. 3.5 (a). The characteristic RLS is shown in Fig. 3.5 (b). For the verification of the scintillator signal, a part of the RLS was measured with a CR-39 nuclear track detector. It can be seen that both measurements complement each other.

To investigate if all protons are contributing to the ring or only protons with certain energies, one G-CCD was used to observe protons within different energy intervals, while the other G-CCD was used to detect all protons, which were not blocked by the aluminum foil. In Fig. 3.10 (a), the beam profile is shown for two different shots/energy intervals. The left image shows the beam profile for low-energy protons ($0.17 \lesssim E_p/E_{\max} \lesssim 0.20$), and the right one displays the beam profile for protons with higher kinetic energies ($0.53 \lesssim E_p/E_{\max} \lesssim 0.72$). The small images in the upper left corners show the beam profile containing protons with $1.0 \text{ MeV} \leq E_p \leq E_{\max}$. For the low-energy protons, a clear RLS is visible, similar to the RLS for all protons with energies above 1.0 MeV. In contrast to that, the protons with higher kinetic energies do not form a RLS. This beam profile is more homogeneous, except for a hotspot in the upper right part of the image. The spatial distribution of all detectable protons shows a very sharp RLS for this shot, too. Hence, the beam profile

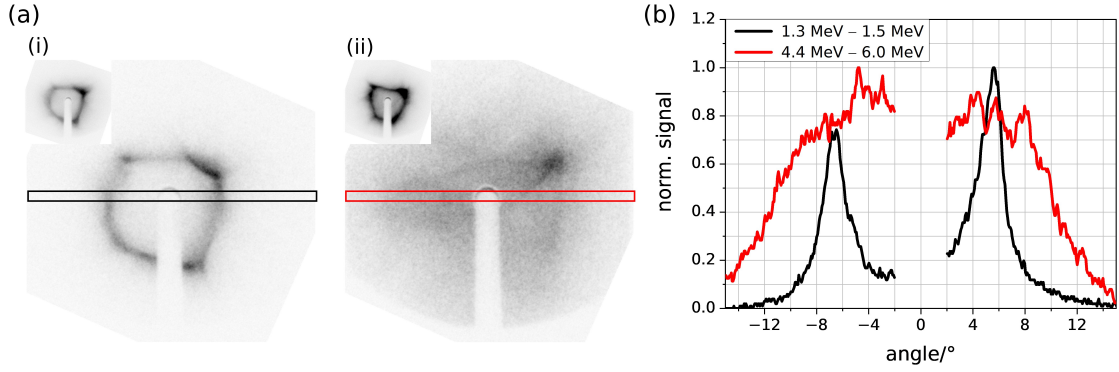


Figure 3.10.: In (a), the proton beam profile is displayed for two different shots, measured with a G-CCD that was set to observe protons within the energy intervals of (i) $1.3 \text{ MeV} \lesssim E_p \lesssim 1.5 \text{ MeV}$ and (ii) $4.4 \text{ MeV} \lesssim E_p \lesssim 6.0 \text{ MeV}$ (large images). The target was a 200 nm thin foil, and the maximum proton energies, measured with the TP, for the two shots were $E_{\text{max}} \approx 7.6 \text{ MeV}$ and $E_{\text{max}} \approx 8.3 \text{ MeV}$. The small images in the upper left corners show the beam profiles captured with the second G-CCD for $1.0 \text{ MeV} \leq E_p \leq E_{\text{max}}$. The corresponding lineouts taken along the rectangles are shown in (b). Both lineouts are normalized to their maximum. Note that the given energy intervals are for the center of the beam’s profile. For the horizontal sides of the scintillator, the energy intervals shift slightly to $1.4 \text{ MeV} \lesssim E_p \lesssim 1.6 \text{ MeV}$ and $4.7 \text{ MeV} \lesssim E_p \lesssim 6.4 \text{ MeV}$ due to an increased distance to the target.

is dominated by protons with low kinetic energy. Since proton beams accelerated via TNSA usually exhibit spectra that decrease exponentially for higher energies, this is not surprising. Note that the signal strength of the scintillator signal increases with increasing proton energy for the same number of protons. However, this is not enough to smear out the RLS when the entire proton energy spectrum was observed with the second G-CCD.

For a comparison of the measurements with 2D-PIC simulations, horizontal lineouts were taken along the indicated rectangles. The normalized lineouts are shown in Fig. 3.10 (b). Here, the distribution for the higher energies is slightly broader than the peak-to-peak distance/opening angle for the case of lower proton energies.

For an investigation of the RLS’s orientation, the target’s normal direction and the laser’s propagation direction were separated by tilting a foil around the vertical axis (y -axis) going through the position of the laser focus. The laser’s forward direction relates to mechanisms like RPA, while the foil’s normal direction correlates with the TNSA mechanism. In Fig. 3.11 (a) three exemplary beam profiles are displayed, one for normal laser incidence and two with different rotation angles. The RLS

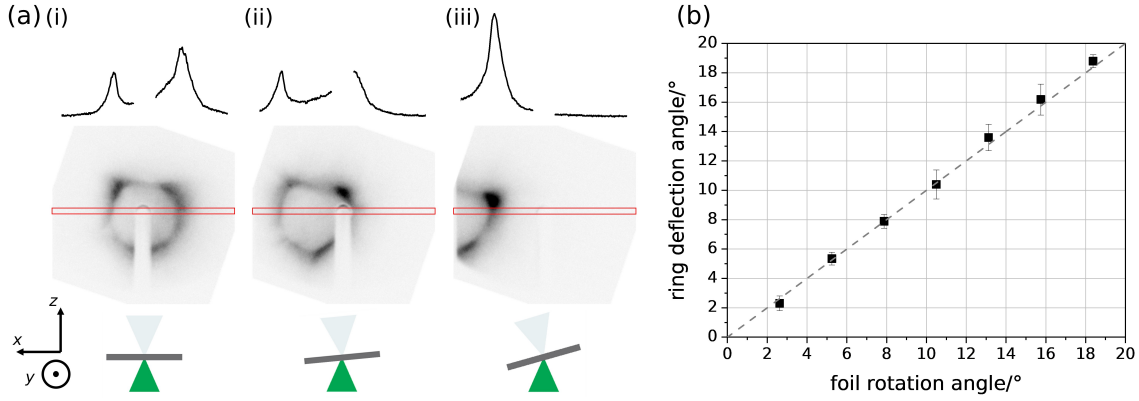


Figure 3.11.: The figure shows the effect of the rotation of a 480 nm thin foil around the vertical axis (y -axis) going through the laser’s focus position. (a) displays exemplary images of the beam profile for three different rotation angles with corresponding lineouts. (i) represents 0° , the standard normal laser incidence case, while in (ii) and (iii), the beam profiles for a tilt angle of about 5.25° and 15.75° are shown. (b) shows the deflection angle of the RLS as a function of the rotation angle. The total scan consists of 19 individual shots. The line is a guide for the eye to emphasize the 1 : 1 relation between the angles. The deflection angle was measured by determining the position of both peaks, or one when only one was visible on the scintillator, relative to the peak positions of the 0° case.

changes its position on the scintillator screen accordingly to the tilt angle of the foil. From the systematic scan in (b), a one-to-one relation between the two angles can be deduced. Thus, the RLS is clearly oriented around the normal direction of the foil. That is a strong indication that the protons forming it are accelerated via the TNSA mechanism.

Finally, the dependence of the opening angle on the foil thickness was investigated, as presented in Fig. 3.12 (b) (black graph). Here, a small but continuous decrease of the opening angle could be observed.

3.4.2. Simulations and interpretation

For a deeper understanding of the underlying physics, 2D-PIC simulations with the code EPOCH were performed [140].³ The 10000×10000 cell simulation grid covered a spatial extension of $-5 \mu\text{m} \leq z \leq 45 \mu\text{m}$ and $-25 \mu\text{m} \leq x \leq 25 \mu\text{m}$, while 50 particles per cell were used. The target foils, with the four different thicknesses

³The simulations were performed by Stefan Tietze. The simulation data was analyzed by myself with open-source software [174–177].

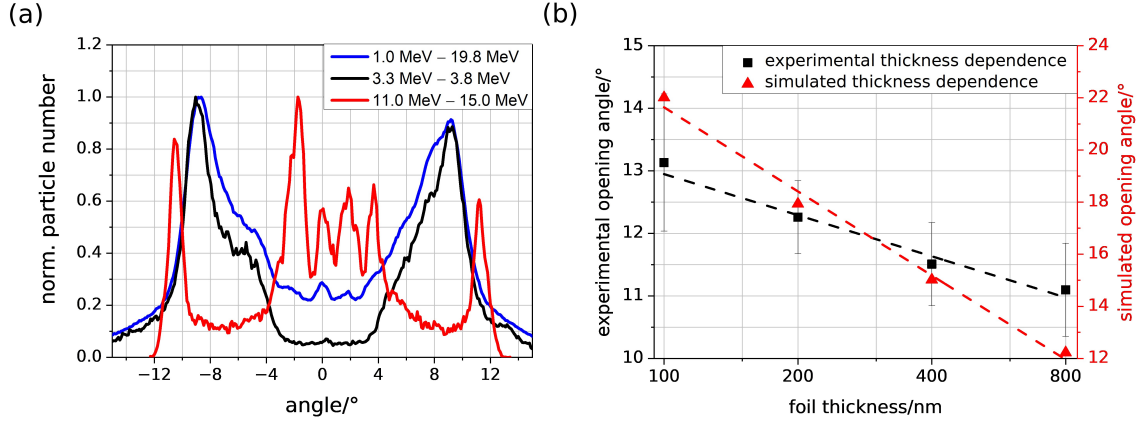


Figure 3.12.: (a) shows the normalized proton distribution as a function of the emission angle extracted from the simulations for a 200 nm thin foil at the time $T_0 + 198$ fs. The blue graph shows the beam profile for all protons between 1.0 MeV and the maximum kinetic energy of 19.8 MeV. The black graph includes protons with $3.3 \text{ MeV} \leq E_p \leq 3.8 \text{ MeV}$, while the red graph shows the angular distribution for $11 \text{ MeV} \leq E_p \leq 15 \text{ MeV}$. (b) displays the opening angle of the RLS in dependency on the four different foil thicknesses. The black squares represent the averaged measured values with standard deviation, and the red triangles are the simulated opening angles. The averages consist of 11 shots for the 100 nm thin foil, 4 for 200 nm, 6 for 400 nm, and 6 shots for the 800 nm thick foil. Here, the lineouts from the measured beam profiles, including all protons not blocked by the aluminum foil, were used to determine the opening angle.

$d = 100$ nm, 200 nm, 400 nm, and 800 nm, had a lateral extension of $-20 \mu\text{m} \leq x \leq 20 \mu\text{m}$, and their front surface was centered at ($z = 0 \mu\text{m}$, $x = 0 \mu\text{m}$). The foils had a maximum plasma density of $n_{e0} = 90 \cdot n_c$ ($\lambda = 515$ nm). As ions, protons and C^{6+} ions with a number ratio 1 : 1 were included. The initial temperature of all plasma components was set to 1 keV. The laser pulse with a central wavelength of 515 nm was modeled to have a Gaussian shape both in space and time, with a focal spot diameter of $3 \mu\text{m}$ and a pulse duration of 140 fs. The pulse was linearly polarized and had a maximum amplitude of the normalized vector potential of $a_0 = 4.5$. The peak of the pulse entered the simulation box ($z = -5 \mu\text{m}$) at the time $t = 322$ fs $=: T_0$ after the start of the simulation. The pulse peak arrived at the front surface of the target 16.7 fs later, i.e., $T_0 + 16.7$ fs.

The RLS in the 3D experiment corresponds to a two-peak structure in the 2D simulations. For the simulated 200 nm thin foil, the normalized particle number is displayed in Fig. 3.12 (a) as a function of the particles' emission angle = $\arctan(p_x/p_z)$ for the time $T_0 + 198$ fs. The blue graph includes all protons with $1.0 \text{ MeV} \leq E_p \leq E_{\text{max}}$,

where $E_{\max} = 19.8 \text{ MeV}$ is the maximum proton energy for this timestep. The higher maximum proton energy, compared to the experiment, is likely due to the 2D geometry of the simulations. In [178], 3D simulations were compared with 2D simulations. The latter produced cutoff energies of about a factor of 2.3 higher than in 3D. For the 2D simulations, one should also note that the cutoff energy depends on the simulation time, which may be a consequence of the plasma being only diluted in two dimensions and not in three. Higher particle densities and higher field strengths over longer times, compared to experiments, are the consequences.

Because the maximum proton energy for this simulation is roughly two and a half times as high as the energies measured for the two shots in Fig. 3.10, the boundaries of the energy intervals in the simulation were multiplied by 2.5. The simulation reproduces the RLS for protons with low kinetic energy ($0.17 \lesssim E_p/E_{\max} \lesssim 0.19$). For the protons with higher kinetic energy ($0.56 \lesssim E_p/E_{\max} \lesssim 0.76$), the amount of particles emitted around the forward direction significantly increases, but two peaks at the sides remain. For these high energy protons, the experimental lineouts are smoother except for the peak in the upper right of the beam profile in Fig. 3.10 (a_{ii}). Thus, the simulation reproduces quite well the spatial structure of the accelerated proton beams from the experiments.

The proton distribution with $1.0 \text{ MeV} \leq E_p \leq E_{\max}$ was used to compare the simulated thickness dependence of the opening angle with the experiment. The opening angle of the RLS is plotted as a function of the target thickness d for the simulation (Fig. 3.12 (b), red) in addition to the experiment (black). The simulation reproduces the decrease of the opening angle for increasing foil thickness qualitatively. The higher values of the simulated opening angle and the steeper slope are again likely due to the 2D simulation geometry. In general, the simulations could qualitatively well reproduce the experimental characteristics of the RLS.

The proton acceleration process is displayed in Fig. 3.13 for the 200 nm thin foil to investigate the origin of the RLS. (a) displays the longitudinal charge separation field due to the electron sheath and the positively charged target. The electric field is strongest around the center of the target $x \approx 0 \mu\text{m}$ (i)–(iii), which is opposite to the position of the highest laser intensity on the front surface. Hence, the highest electron density is located along $x \approx 0 \mu\text{m}$ where also the highest electric field is generated. In (b), the corresponding expansion of the proton density is shown.

The protons around $x = 0 \mu\text{m}$ gain higher momenta and travel longer distances along the z -axis than the protons starting at positions with $|x| \gg 0 \mu\text{m}$ due to

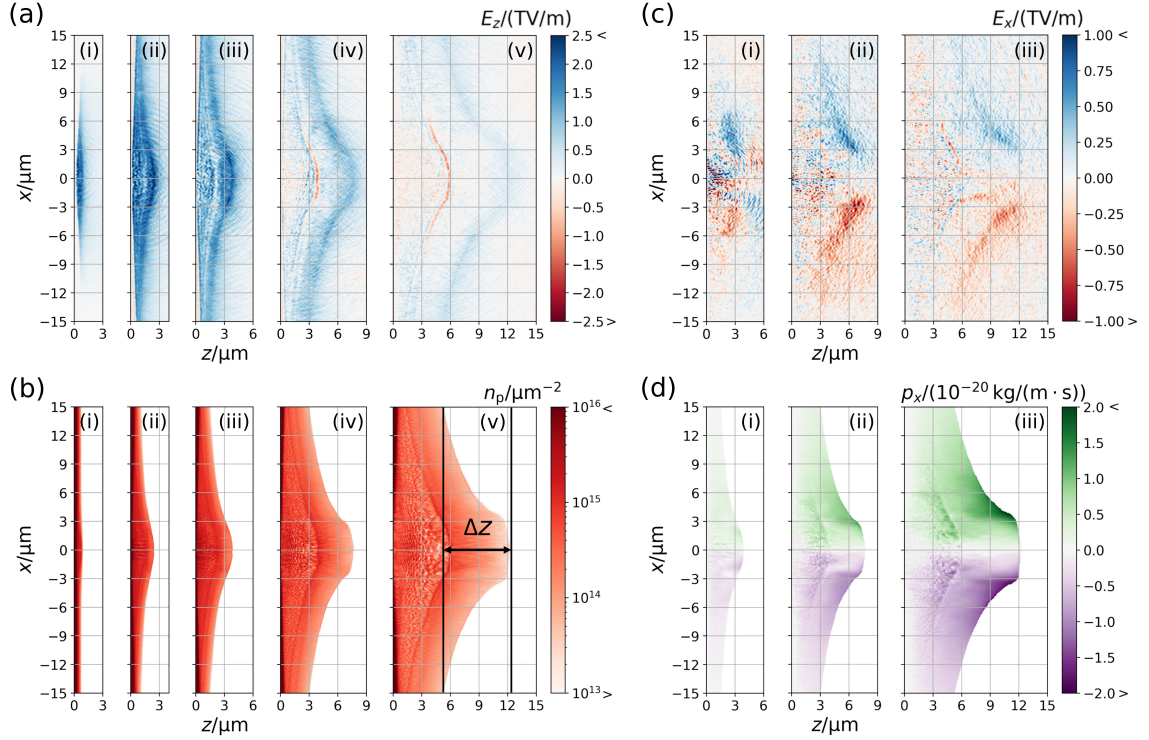


Figure 3.13.: This figure shows the process of the proton acceleration for the simulated 200 nm thin foil for different timesteps. In (a), the longitudinal electric field $E_z(z, x)$ is shown, which is parallel to the target's normal direction. The five different displayed time steps are (i) $T_0 - 82$ fs, (ii) $T_0 - 2$ fs, (iii) $T_0 + 38$ fs, (iv) $T_0 + 118$ fs, and (v) $T_0 + 198$ fs. (b) displays the proton density distribution for the same time steps. (c) presents the lateral electric field $E_x(z, x)$ for the three times (i) $T_0 + 38$ fs, (ii) $T_0 + 118$ fs and (iii) $T_0 + 198$ fs. (d) shows the lateral momentum $p_x(z, x)$ of the protons at these three time steps.

the variation of E_z along the x -axis. A charge separation is induced between the maximum positive charge at $x = 0 \mu\text{m}$ and the negative charge of electrons in the vacuum region due to the path length difference Δz , as indicated in Fig. 3.13 (b_v).

The electric field component along the x -axis $E_x(z, x)$ caused by this charge separation is displayed in (c), with the first image showing the field at $T_0 + 38$ fs. That is the first recorded time step at which the RLS can be identified in this simulation.

The momentum $p_x(z, x)$ is shown in (d). Around $x \approx 0 \mu\text{m}$ there is no lateral field and thus $p_x \approx 0$. It can be seen that the maxima of p_x are formed at the front sides of the proton distribution, where the maxima of E_x are located. For the last time step $T_0 + 198$ fs, these maxima are within the area described by $9 \mu\text{m} \leq z \leq 12 \mu\text{m}$ and $3 \mu\text{m} \leq |x| \leq 6 \mu\text{m}$. Here, the lateral charge separation is maximal. From these

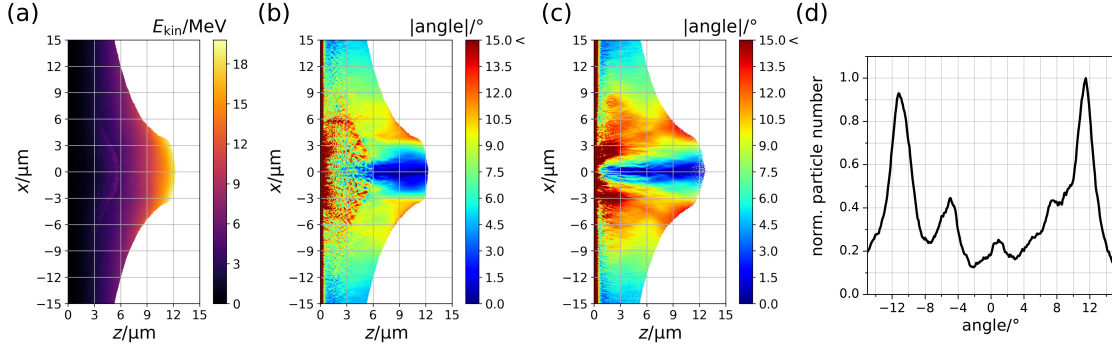


Figure 3.14.: (a) displays the kinetic energy of protons for the simulated 200 nm thick foil and the time $T_0 + 198$ fs. (b) presents the absolute value of the protons' emission angle as a function of the spatial coordinates for the same foil and time. In (c) is the emission angle for the simulation without carbon ions shown. (d) shows the particle number as a function of the emission angle for $1.0 \text{ MeV} \leq E_p \leq E_{\text{max}}$.

positions, $|p_x(z, x)|$ decreases towards the target's initial surface and for larger values of $|x|$ where the boundary between the proton density distribution and the vacuum becomes more parallel to the initial target surface.

In Fig. 3.14 (a) and (b) are the distribution of the protons' kinetic energy and the distribution of the absolute value of the deflection angle $|\arctan(p_x(z, x)/p_z(z, x))|$ plotted to investigate the spatial origin of the RLS. In (a), it can be seen that in the areal described by $9 \mu\text{m} \leq z \leq 12 \mu\text{m}$ and $3 \mu\text{m} \leq |x| \leq 6 \mu\text{m}$, protons with high kinetic energies are located. These protons are emitted under large angles ($\approx \pm 11^\circ$), as seen in (b), and are forming the peaks in Fig. 3.12 (a) (red graph).

However, the low-energy protons emitted into the two peaks (blue and black graph) originate from the large yellow/green region ($\approx \pm 9^\circ$), which is located around $2 \mu\text{m} \lesssim |x| \lesssim 10 \mu\text{m}$. This large region of constant emission angle is the consequence of both momentum components behaving similarly. The maxima of both distributions are located at the expansion front. From these positions, their absolute values decrease towards the foil, and also in the outward direction.

The modulated region in these plots ($z \lesssim 6 \mu\text{m}$ for $x \approx 0 \mu\text{m}$) is the intersection between the proton density distribution and the carbon density distribution. Although it includes mostly protons with very low kinetic energy, there might be an influence of the carbon ions on the angular distribution due to modulations in the electric field. The carbon ions were removed for an additional simulation to exclude this possibility.

The removed charge was replaced by protons to maintain charge neutrality. The results of this simulation are presented in Fig. 3.14 (c) and Fig. 3.14 (d). The two peaks are still present in (d) at slightly larger emission angles $\approx \pm 11.3^\circ$, and the location of these protons in (c) (orange region) is the same areal as for the foil with carbons (b). Consequently, the heavy ions are not essential for the formation of the RLS. However, the carbon ion front causes a modulation of $E_z(z, x)$ (Fig. 3.13 (a), steps (iv) and (v)) that modulates the protons' energy spectrum as described in [107, 179–181].

A region with large emission angles is also visible in Fig. 3.14 (c) close to the target's rear surface ($z \lesssim 3 \mu\text{m}$, $|x| \lesssim 2 \mu\text{m}$) that cannot be identified in (b) due to the modulations caused by the carbon ions. In this region, the protons have a low momentum p_z . Consequently, a low p_x is enough for large emission angles.

The smearing of the proton beam profile for high proton energies can be explained as follows. Protons with high kinetic energies are only localized at the front of the distribution (Fig. 3.14 (a)) and experience the strongest variation of E_x (Fig. 3.13 (c)), causing proton emission in a large solid angle, as seen in Fig. 3.14 (b).

The orientation of the RLS around the target's normal is also a direct consequence of the proton expansion since the lateral charge separation is always perpendicular to the initial longitudinal TNSA field and parallel to the foil's surface.

The simulated electric field for the four different foil thicknesses is presented in Fig. 3.15 for $T_0 + 78$ fs to identify the reason for the decreasing opening angle as a function of the thickness. E_z is displayed in (a) and E_x is plotted in (b).

Since the decrease of the simulated opening angle is quite pronounced, it is necessary to compare the absolute field values in more detail. Therefore, the absolute values of both field components were averaged over the regions indicated by the black rectangles. These averaged values are shown in (c). The relative decrease of E_x is much steeper than the reduction of E_z , causing the strong decline of the RLS's opening angle. If both components would decrease in the same way, the opening angle would likely not decline. Instead, the presence of the RLS would probably only shift to lower proton energies.

The proton density distribution is shown for the 100 nm (i) and the 800 nm (ii) thin foil in (d) for $T_0 + 78$ fs to illustrate the origin of this decrease of E_x . Both density distributions have a different shape. The center ($x \approx 0 \mu\text{m}$) of the distribution (i) has expanded a greater distance Δz into the vacuum, compared to the edges of the

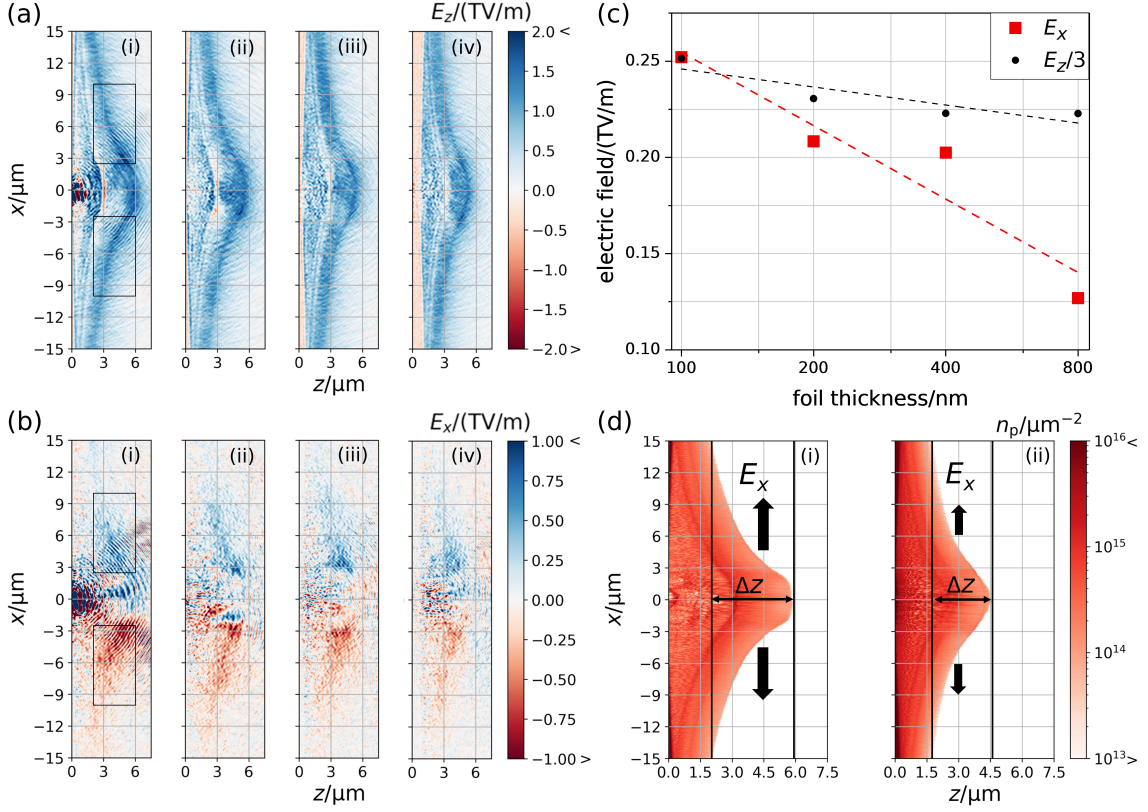


Figure 3.15.: (a) and (b) are displaying $E_z(z, x)$ and $E_x(z, x)$ for the time $T_0 + 78$ fs and the four different simulated foil thicknesses (i) 100 nm, (ii) 200 nm, (iii) 400 nm, and (iv) 800 nm. The electric field within the rectangles was averaged and plotted against the foil thickness in (c). Note that E_z was divided by a factor of 3. The values for E_x are the averaged absolute values of the two average values in both rectangles. (d) displays the proton density distribution for the 100 nm (i) and the 800 nm (ii) foil for $T_0 + 78$ fs. Note that only in these two density plots, the foils' rear surface is located at $z = 0 \mu\text{m}$, in contrast to previous images.

distribution, than the center of (ii). Hence, the proton distribution is flatter for thicker foils, leading to a reduced E_x . Thus it may be concluded, that strength and extension of E_x depend strongly on the shape of the proton expansion into the vacuum.

The reason for a flatter proton distribution in the case of thick foils is likely that E_z has a smaller dependence on x as compared to thin foils during the acceleration process because the electron sheath's distribution is sharper for thinner foils due to the divergence of the hot electrons. The difference of the electron sheath in the experiment is likely much less pronounced than in the simulation since the measured opening angle decreases only slightly as compared to the simulation. This difference

between experiment and simulation is probably a geometrical effect of the difference between 2D and 3D.

Besides the dependence on the thickness, the generation of the hot electrons itself will likely influence the shape and opening angle of the RLS. The hot electron generation is linked to the TIC and to the intensity distribution of the laser close to the focus. The latter might explain why the measured RLS is not a perfectly shaped ring and has more the shape of connected hot-spots. In [182], an experiment with gold foils with thicknesses between 13 μm to 50 μm is described wherein a change in focus led to a change in the proton beam profile.

A factor that may play a role for foils thinner than 100 nm is if the laser breaks through the foil. In an experiment with thinner aluminum foils, it was measured that the opening angle decreases when reducing the foil thickness [173]. An explanation may be that the quasi-static electric fields are reduced when the laser breaks through the foil early during the interaction, or that the laser directly modifies the hot electron sheath. Note that in Fig. 3.15 (a_i) and (b_i), the modulations close to ($z = 0 \mu\text{m}$, $x = 0 \mu\text{m}$) are the electric field of the laser breaking through the 100 nm thin foil. However, this does not prevent the occurrence of the RLS in the simulations presented here. Additionally, no laser breakthrough was observed in the experiment.

3.5. Summary and discussion

In this chapter, laser-driven ion acceleration from thin foils using contrast-enhanced laser pulses has been investigated. In an experimental campaign with a PM, the dependencies of the maximum proton energy, as well as the carbon ion energy, on the target thickness, the laser's polarization, and pulse energy were studied. For LP, maximum ion energies were measured to be almost independent on the foil thickness for $10 \text{ nm} \leq d \leq 500 \text{ nm}$. These results are comparable with experiments performed at other laser systems [53, 162, 163] and consistent with ion acceleration via TNSA. For the 5 nm thin foil, a significant increase of the maximum ion energies was measured due to a steeper scaling with the laser energy. However, with the onset of transparency, this scaling stops and prevents the realization of higher ion energies under these experimental conditions. Since hydrodynamic simulations indicate that due to the laser pulse's rising edge, the 5 nm thin foil has expanded into a near-critical plasma, it is likely that the TIC of POLARIS needs to be further improved to exploit the strong increase of the ion energies as a function of the laser's pulse

energy. Due to this strong (pre-)plasma expansion, a simple, definitive interpretation of the results is not trivial. Hence, extensive PIC simulations for the varied laser and target parameters are necessary.

Besides ion acceleration with LP, the laser pulses were converted to CP to investigate ion acceleration via RPA. As expected, the use of CP led to a decrease of the maximum ion energies due to a reduced electron heating, especially for the thicker foils. For decreasing foil thickness, the maximum ion energies slowly increased, which might be due to an enhancement of electron heating due to foil deformation [163]. As in the case of LP, the highest maximum ion energies with similar absolute values were obtained for the 5 nm thin (CP) foil due to an increased scaling with the laser energy, but at higher pulse energy.

Besides the dependencies of the maximum ion energies, the proton beam's profile was investigated in an experimental campaign using the second harmonic of POLARIS and plastic foils with $100 \text{ nm} \leq d \leq 800 \text{ nm}$. It was found that protons with low kinetic energies form a very reproducible RLS, while protons with higher kinetic energies have a more homogeneous lateral distribution. By rotating a foil around the vertical axis, it could be observed that the RLS's orientation is always centered around the foil's normal direction. For increasing foil thickness, it could be determined that the opening angle of the RLS decreases. Due to the combination of high-contrast laser pulses and foils that are much thicker than necessary for LS-RPA and above the onset of transparency (see Sec. 2.4.3.2), the influence of acceleration mechanisms that are expected to be dominant for very thin foils is very unlikely.

Hence, with the help of 2D-PIC simulations, an explanation for this RLS could be found that fits within the concept of laser-driven ion acceleration with the TNSA mechanism and explains the experimental observations. In this model, the RLS thus arises due to a lateral charge separation that is a consequence of the proton distribution's shape during the acceleration process via TNSA.

4. Ion acceleration with water microdroplets

This chapter presents the results of an experiment performed at the JETI 40 laser system with water microdroplets as targets and off-harmonic optical probing of the laser-plasma interaction. A short description of the laser system and the optical probe laser are given in Sec. A.1.

Water microdroplets as targets for laser-driven ion acceleration have one main advantage in contrast to foils when considering the TNSA mechanism (see Sec. 2.4.1). Since a foil usually has a much larger lateral extension than the laser's focal region, hot electrons generated by the laser can leave the interaction region along the foil's surface [57]. As a result, the electron density at the target's rear side is reduced, which eventually lowers the electric field responsible for the ion acceleration process (see Eq. (2.34b)). In contrast, water droplets have a limited extension in all three spatial dimensions, which confines the electrons to a smaller volume. Besides droplets, small isolated plastic spheres levitating within a Paul trap also fulfill this condition and have been successfully used as targets [183–186]. However, after a laser shot has interacted with and then destroyed a sphere, a new one has to be moved into the interaction region, i.e., the Paul trap, which takes a lot of time and experience for this kind of target. Water droplets generated by a nozzle can be created with a repetition rate of ≈ 1 MHz in the interaction region, which makes them interesting for laser-driven ion acceleration, especially when it comes to experimental statistics and applications. Such (heavy) water droplets were already used in experiments at the Max Born Institut in Berlin. At these experiments, the kinetic energy per nucleon of the accelerated deuterons or protons was ≈ 1 MeV [187–190]. Since it was possible to accelerate protons to higher kinetic energies with comparable laser parameters at the JETI 40 laser system [191], it seemed necessary to investigate which experimental parameters are crucial for the generation of MeV protons from microdroplets.

In this chapter, the influence of the droplets' position relative to the laser's focus position along the laser's polarization axis will be described. Furthermore, the effect of an artificial pre-plasma was investigated. Images of the plasma expansion were captured with the probe laser and imaging system. The plasma expansion can be correlated to the proton acceleration process. An explanation of the experimental results of the proton acceleration, with the help of 2D PIC-simulations, will be presented. Also, measurements of the proton beam's profile were performed. The chapter starts with a description of the experimental setup.

4.1. Experimental setup

The experimental setup in the JETI target chamber is shown in Fig. 4.1 (a). The main laser pulses at $\lambda_L = 800$ nm were frequency doubled by a KDP crystal at the entrance of the target chamber to improve the TIC [193]. The half-wave plate and the KDP crystal were oriented in such a way that the 2ω -pulses were horizontally polarized behind the crystal. The FWHM pulse duration of these 400 nm-pulses was simulated to be $\tau_L \approx 42$ fs [194].

Between the KDP crystal and the focusing parabola, two dichroic mirrors were placed to reduce the remaining laser light at 1ω . The measured TIC of the fundamental and the calculated one for 2ω are shown in Fig. 4.1 (c).

The 400 nm-pulses were then focused with a 90° off-axis, aluminum parabola with $f = 101.6$ mm, $\approx f/1.8$. The spot where the laser intensity is higher than 50 % of the peak value had a size of $A \approx 1.1 \mu\text{m}^2$ and contained a fraction of $q \approx 0.2$ of the total pulse energy of $E_L \approx 90$ mJ. A and q were extracted from focal spot images of pulses with low laser energy. From these values, the intensity within the focal area can be estimated as $I_L \approx E_L \cdot q / (A\tau_L) \approx 4 \cdot 10^{19}$ W/cm², which corresponds to $a_0 \approx 2.1$ (see Eq. 2.7).

A motorized half-inch mirror could be placed in front of the second dichroic mirror to introduce a pre-pulse with an approximate intensity of 10^{16} W/cm² to generate a pre-plasma in a controlled way. Due to the smaller beam diameter, the pre-pulse had a much larger focal spot compared to the focused main laser pulse [194, 195]. For the measurement of the pre-plasma expansion triggered by the pre-pulse alone, a circular aperture with a diameter of ≈ 8 mm could be used to block the main laser. Nozzles (Micro Jet Components) equipped with a piezo element were used to gener-

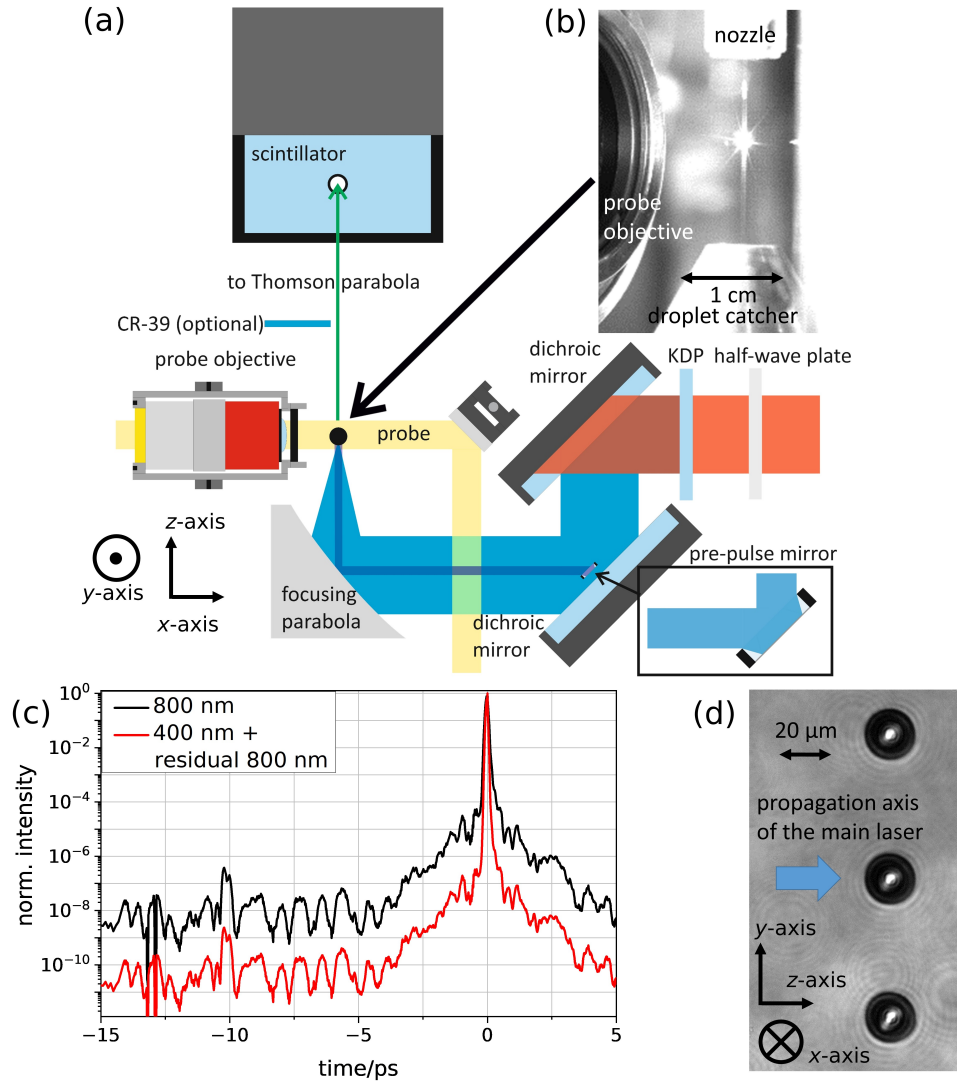


Figure 4.1.: (a) is a sketch of the experimental setup (not to scale). (b) displays a photo of the interaction zone. (c) presents the measured TIC of the 1ω -pulses (black curve) and the calculated TIC of the 2ω -pulses (red curve), including the residual light at 1ω . Data for (c) was provided by A. Sävert [192]. (d) shows a part of a droplet chain illuminated by the probe laser only.

ate a chain of water microdroplets. The piezo element was driven by a high-frequency voltage that was synchronized with the laser's repetition frequency. Such an excitation leads to a controlled breakup of the water jet into a chain of droplets. These droplets had a diameter of $\approx 20 \mu\text{m}$ and were spatially and temporally stable relative to the arrival of the main laser pulse and its focus position. Details of the synchronization procedure can be found in [191]. Below the interaction region, the water was extracted from the vacuum chamber by a heated, separately pumped droplet

catcher, which had an entrance aperture with a diameter of 0.5 mm. Fig. 4.1 (b) is an image of the water jet emerging from the nozzle in downward direction together with the upper part of the droplet catcher.

The few-cycle probe laser was used to observe the laser-droplet interaction (see Sec. A.1.1). The probe pulses illuminated the droplets perpendicular to the main laser's propagation axis. After the objective of the imaging system, a bandpass-filter with a transmission of (710 ± 20) nm was implemented. This filtering to wavelength regions clearly separated from 800 nm and 400 nm was used to minimize the signal from plasma emission or scattered laser light in the images. Droplets illuminated by the probe are exemplarily shown in Fig. 4.1 (d).

To measure the energy spectrum of protons accelerated in the main laser's forward direction, the TP was used (see Sec. 3.1.1). In this experiment, the distance of the entrance aperture, with a diameter of 1.0 mm, from the target was 97 cm. As a consequence, the TP covered a solid angle of $\Omega \approx 0.8 \mu\text{sr}$. The distance between the aperture and the MCP was 35.5 cm, while the MCP was placed 5 cm behind the end of the TP's magnet. The size of the projected aperture on the MCP's surface leads to an energy resolution of $\Delta E_{\text{kin}}/E_{\text{kin}} \approx 0.1$ for $E_{\text{kin}} \approx 2$ MeV for protons.

The combination of the plastic scintillator and the G-CCD camera was used to measure the proton beam's spatial profile (see Sec. 3.1.2). In this setup, the center of the scintillator had a distance of 29 cm to the droplets (tilted upwards by 20°). In addition, for a few individual shots, CR-39 detector plates could be placed at a distance of 7.3 cm to the droplets.

4.2. Plasma expansion

The interaction of the main laser pulse with the droplets was observed for different delays between the main laser pulse and the probe pulse, as shown in Fig. 4.2 (a). Here, T_0 denotes the time at which the main laser pulse irradiates the central droplet. Before the main laser pulse arrives (left picture, $T_0 - 0.2$ ps), all water droplets act as spherical lenses for the probe beam. Therefore, the probe beam's light is focused and produces bright spots in the image (orange arrow). The bright light (green arrow), visible close to the central droplet, is probably due to the scattering of laser light by the plasma electrons. It is very localized and must contain light within (710 ± 20) nm since it was detected by the camera equipped with a bandpass filter.

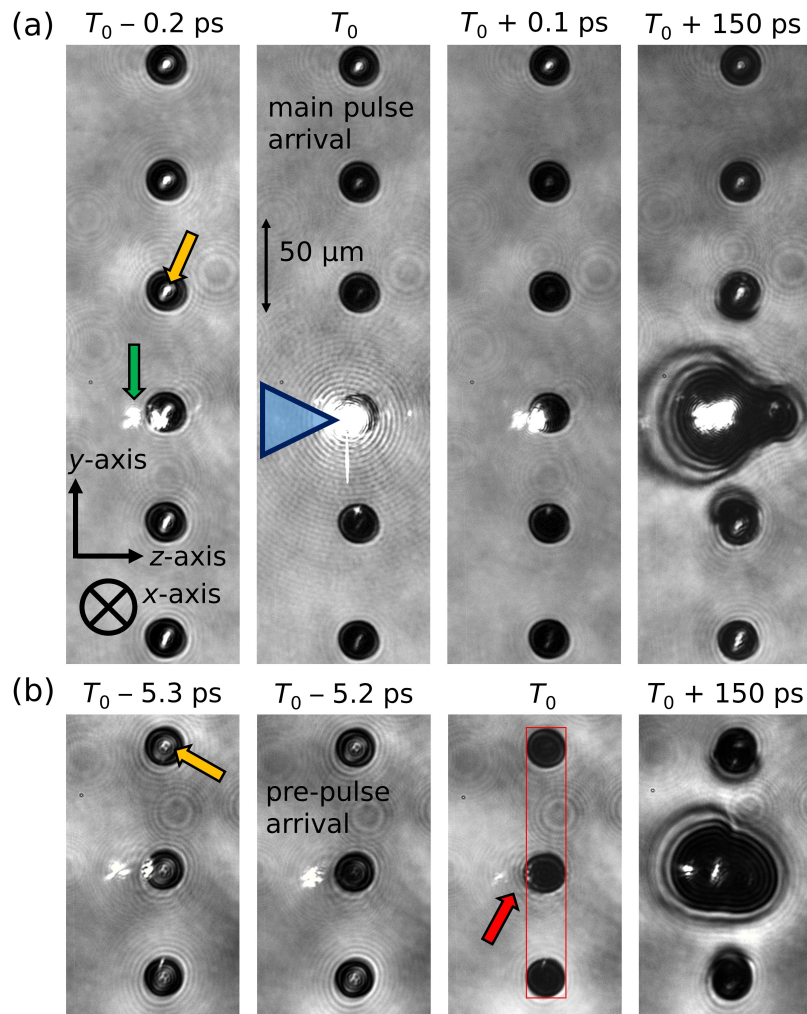


Figure 4.2.: Exemplary images of the laser-droplet interaction for different laser shots and time delays of the probe pulse, concerning the main pulse's arrival at T_0 , are shown in this figure. (a) shows the scan without and (b) with an applied pre-pulse. Both the main pulse and the pre-pulse illuminate the central droplet from the left, as indicated by the blue triangle in the second image of (a). In (b), the pre-pulse arrival is at $T_0 - 5.2$ ps. For the image at time T_0 , a small expansion of the central droplet in the left direction, due to the pre-pulse, is emphasized by the red rectangle and the red arrow. Note that the distance between different pairs of droplets is slightly different but stable.

It is visible on every image since the camera's minimal exposure time is several microseconds, which is orders of magnitudes longer than the probe's pulse duration and the entire time of the laser-droplet interaction.

The blackening of the central droplet and its neighbors at T_0 is a consequence of the main pulse's arrival. The pulse ionizes the droplets and generates a plasma with

an electron density higher than n_c for the probe pulse's filtered spectrum centered around 710 nm. As a result, the probe's light is no longer transmitted and focused by the droplets. At the next shown time step of $T_0 + 0.1$ ps, no visible change of the central droplet's shape is visible. That means that on this timescale, within which the ions are accelerated to MeV energies ($t \gtrsim \tau_L$), no direct indication of this short acceleration process can be seen in the shadowgraphy images.

About 150 ps after the main pulse's arrival (right image in (a), $T_0 + 150$ ps), the central illuminated droplet has expanded significantly, mostly towards the incident laser (left), but also a bulge on the right is visible. Additionally, the two neighboring droplets of the central droplet have expanded a bit towards the central droplet. Since the neighboring droplets are transparent again to the probe's light, the plasma density inside the droplets must have dropped below the critical density due to the recombination of plasma electrons with ions. Although the expansion process of the central droplet clearly does not occur on the same time scale as the acceleration process of protons to megaelectronvolts of kinetic energy, the size and form of the expanded plasma give information about the position of the droplet relative to the laser's focus. Hence, these images of the plasma expansion allow to draw conclusions about the proton acceleration process, as shown in Sec. 4.3.

A pre-pulse was introduced, arriving ≈ 5.2 ps before the main laser pulse, to investigate the influence of a pre-plasma on the interaction. In Fig. 4.2 (b) images of the expansion driven both by pre- and main pulse are shown. Before the arrival of both laser pulses ($T_0 - 5.3$ ps image), all droplets are transparent to the probe's light. In contrast to Fig. 4.2 (a), the probe's light transmitted and focused by the transparent droplets is not imaged to small spots but rather to extended spots since the droplets had a different position along the x -axis and were irradiated on the side facing away from the objective (orange arrow). Therefore, the scattered light is also reduced in intensity because it was partly blocked by the droplet between the incident laser and the imaging objective.

As soon as the pre-pulse arrives (Fig. 4.2 (b), $T_0 - 5.2$ ps), only the central droplet becomes opaque to the probe pulse, while the adjacent droplets still transmit the probe light. At the time of the main pulse's arrival T_0 , the central droplet has slightly expanded towards the incident pulse due to the heating induced by the pre-pulse. As a consequence of the changed interaction, the shape of the expanded droplet at $T_0 + 150$ ps is different than for the case without a pre-pulse (compare Fig. 4.2 (a) and (b), both $T_0 + 150$ ps images).

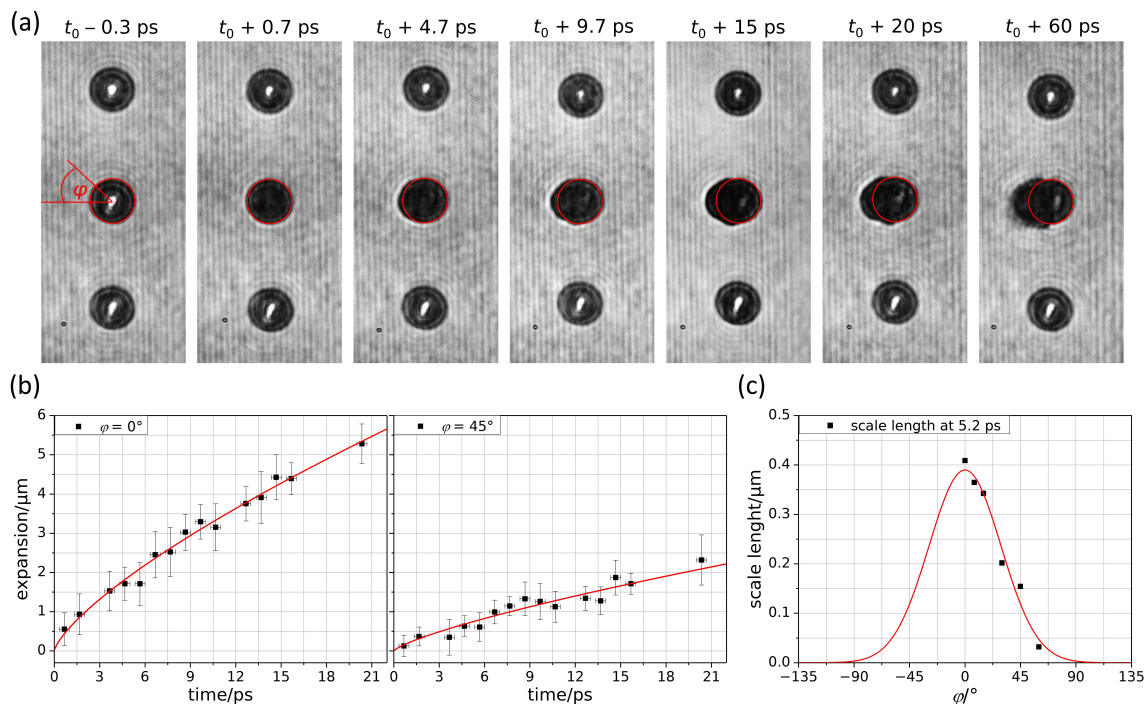


Figure 4.3.: In (a), exemplary images of the plasma expansion induced by the pre-pulse alone are shown for several time steps relative to the time of the pre-pulse arrival t_0 . The main pulse was blocked while taking these images. The red circles denote the original position and size of the central droplet before expansion. (b) shows the estimated position of n_c for two angles φ with respect to the laser's propagation axis, measured from the droplet's center as a function of time. The red lines are power function fits. Note that in these plots, $t_0 = 0$ ps. In (c) is the scale length of the pre-plasma for $t_0 + 5.2$ ps as a function of φ shown. The black squares are values extracted from the power function fits for six different angles. The red line is a Gaussian fit.

For an estimation of the plasma expansion triggered by the pre-pulse alone, the pre-pulse was isolated from the main pulse via a beam block with a small aperture. In Fig. 4.3 (a), the expansion of the pre-plasma is shown for different time steps relative to the pre-pulse's arrival at t_0 . At $t_0 - 0.3$ ps, all droplets focus the light of the probe laser. After the irradiation by the pre-pulse, only the central droplet becomes dark ($t_0 + 0.7$ ps) and starts to expand towards the left, i.e., the direction of the incident laser ($t_0 + 4.7$ ps). The plasma expansion into the left half-space continues up to 20 ps after the pre-pulse has illuminated the droplet. The side facing the TP (i.e., the right side) has not expanded and seems undisturbed at least until the time $t_0 + 60$ ps. That justifies the assumption that when the main pulse was applied together with

the pre-pulse, no plasma gradient was present in the experiment on the droplet's side facing the TP at the time of the main pulse's arrival ($T_0 = t_0 + 5.2$ ps) that would have modified the protons' acceleration process.

The images of the plasma expansion up to 20 ps after the pre-pulse's arrival were used to estimate a pre-plasma profile as input for 2D-PIC simulations. For these input parameters, the following assumptions were made. Firstly, the maximum electron density was estimated as $n_{e,0} \approx 123 \cdot n_c$ ($\lambda = 0.71 \mu\text{m}$), which corresponds to eight freed electrons per water molecule. Secondly, the position of the expansion front as visible in the images was assumed to have a density of $\approx n_c$. For the distance between these two positions, it was assumed that the plasma has an exponential density profile (see Eq. 2.25). The expansion was measured for several shots and timesteps along six different angles, from the center of the droplet with respect to the incoming laser, as indicated in Fig. 4.3 (a) ($t_0 - 0.3$ ps). In Fig. 4.3 (b) is the pre-plasma expansion presented for the two angles ($\varphi = 0^\circ$ and $\varphi = 45^\circ$), showing that the expansion is fastest in the direction of the incoming pre-pulse. The ion sound velocity is (for $\varphi = 0^\circ$) $c_s \approx 80 \frac{\text{nm}}{\text{ps}}$ at the beginning of the interaction and decreases to $c_s \approx 40 \frac{\text{nm}}{\text{ps}}$ for $t \approx t_0 + 20$ ps. Although the measured values are based on unavoidable uncertainties, they seem reasonable. Kahaly *et al.* [195] found $c_s = 37 \frac{\text{nm}}{\text{ps}}$ induced by a pre-pulse with a peak intensity of 10^{16} W/cm^2 focused onto a silicon target.

From the scale lengths measured under the different angles, a Gaussian dependency of the scale length $L(\varphi) = L_{\text{max}} \cdot \exp\left(-2 \cdot (\varphi/58.4^\circ)^2\right)$ was determined (Fig. 4.3 (c)). The maximum scale length along the laser axis is $L_{\text{max}} \approx 0.39 \mu\text{m} \approx \lambda_L$. This pre-plasma profile has been used as input for PIC simulations (see Sec. 4.4). However, to account for the uncertainties of these estimations, pre-plasmas with the scale lengths $L_{\text{max}} \rightarrow L_{\text{max}}/4$, $L_{\text{max}}/2$, and $2L_{\text{max}}$ have been used as an alternative input, too.

4.3. Influence of target position and pre-plasma formation on proton acceleration

The droplets' position along the laser's polarization axis (x -axis) relative to the laser's focus position was varied to investigate the influence of the laser's angle of incidence on the kinetic energy of the protons. At the same time, the energy

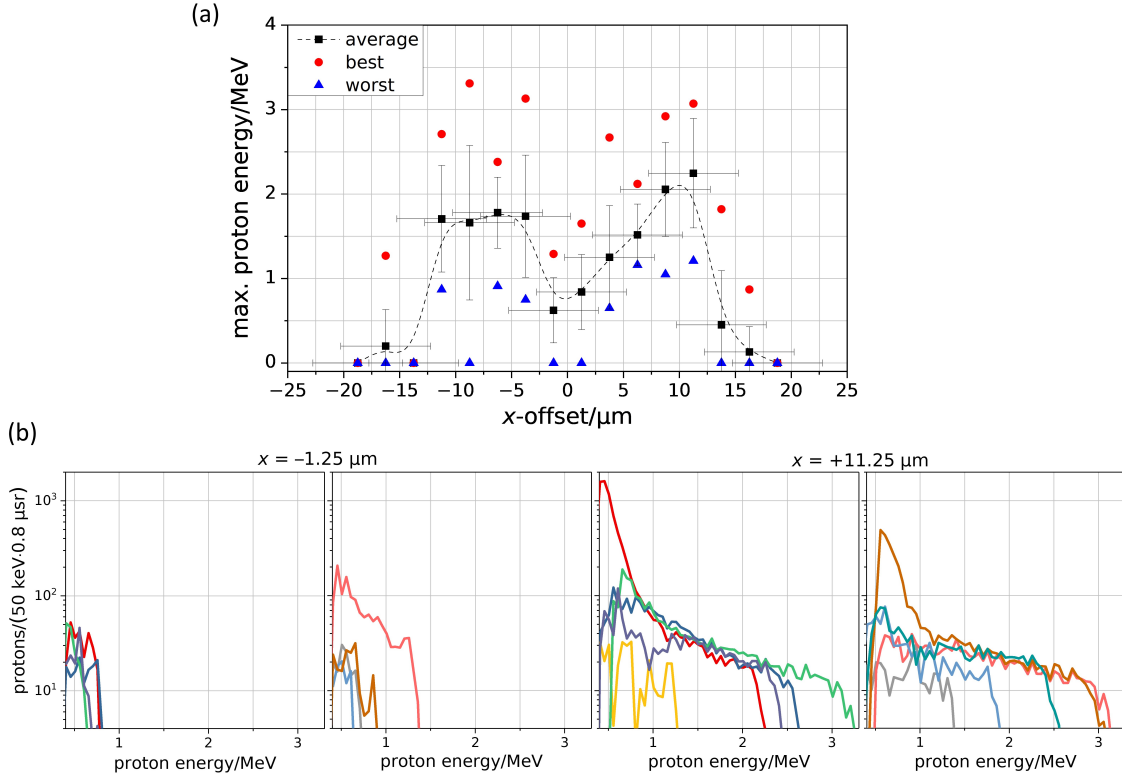


Figure 4.4.: In (a), the maximum kinetic energy of protons as a function of the relative distance to the laser’s focus position along the polarization axis is shown. The total scan includes 165 consecutive shots taken between $x = -18.75 \mu\text{m}$ and $x = +18.75 \mu\text{m}$. At each position, ten shots were taken except for $x = -16.25 \mu\text{m}$ (15 shots), $x = +16.25 \mu\text{m}$ (11 shots) and $x = +18.75 \mu\text{m}$ (9 shots). The mean values and standard deviations of the maximum proton energies are represented by the black squares with error bars. The red circles and blue triangles denote the highest and lowest maximum proton energies measured at these positions, respectively. Shots with no signal above the low-energy threshold of the TP (0.4 MeV) were counted as 0 MeV. If at least one shot at a specific position fulfills this criterion, a blue triangle is set to 0 MeV at this position. Shots counted as 0 MeV were also included in the calculation of the mean values and standard deviations. Consequently, all shots performed during this scan are included in this plot. The error bars for the x -position of the droplets consist of the estimated positioning error of the motor stage, used to translate the nozzle, the pointing of the low-intensity laser focus, and the stability of the droplet position. (b) displays all shots which produced a signal on the TP’s MCP for $x = -1.25 \mu\text{m}$ (normal laser incidence, 8 shots out of 10 produced a signal) and $x = +11.25 \mu\text{m}$ (grazing laser incidence, all 10 shots produced a signal).

spectra of the accelerated protons were measured in the laser’s forward direction. No pre-pulse was applied for this scan.

In Fig. 4.4 (a), the maximum proton energy is plotted against the droplets' position along the x -axis. Since the droplets' exact position relative to the laser focus could not be measured, the zero-offset was set according to the plot's axis of symmetry. For central irradiation of the droplets ($x \approx 0 \mu\text{m}$), the averaged maximum proton energy is below 1 MeV. For larger incidence angles, i.e., larger distances to the focus position, the maximum proton energy rises significantly by a factor of 2–3.

This difference in proton cutoff energy between the cases of normal laser incidence and grazing laser incidence is likely due to a difference in electron heating. When a droplet is irradiated under grazing incidence, the laser's electric field has a component pointing into the droplet and can directly interact with electrons below the droplet surface, most likely via the Brunel heating mechanism (see Sec. 2.3.2.3). Since before main pulse's arrival (Fig. 4.2, $T_0 - 0.2 \text{ ps}$) the irradiated droplet has not yet been ionized, the condition for a steep plasma gradient is satisfied. The hot electrons produced in this way generate an electric field responsible for proton acceleration that is stronger than in the case of central irradiation. In the latter case, the laser cannot penetrate into the droplet due to the steep density gradient yielding a reduced coupling of laser energy into hot electrons via the oscillating $\vec{j} \times \vec{B}$ -heating mechanism (see Sec. 2.3.2.4). The differences between the irradiation geometries will be investigated in more depth with simulations in Sec. 4.4.

The dependence of the maximum proton energy on the target's position is compared to the plasma expansion imaged with the optical probe for the delay of $T_0 + 150 \text{ ps}$. In Fig. 4.5, images of the plasma expansion for three different droplet positions are shown. The images were sorted by their maximum proton energy. For the case of off-axis irradiation (images in (a) and (c)), the droplets have expanded significantly, and a bulge on the right side is visible, which is particularly well-formed for the images shown in (c). Note that for positive values of x , the droplet was moved away from the imaging objective, i.e., the droplets were irradiated on the side facing the objective. Consequently, more signal by scattered laser light was captured by the imaging objective leading to a local saturation of the images.

In contrast, when the droplets were irradiated centrally, they expanded mostly in a triangular shape and much less in the direction to the right (laser's forward direction) (b). That is particularly true for the shots which produced maximum proton energies below 1 MeV. For the shots taken at this position that produced higher proton energies (shots 95 and 93), the size of the plasma is larger, and a small bulge is seen, meaning that the interaction conditions were probably a bit different than for the

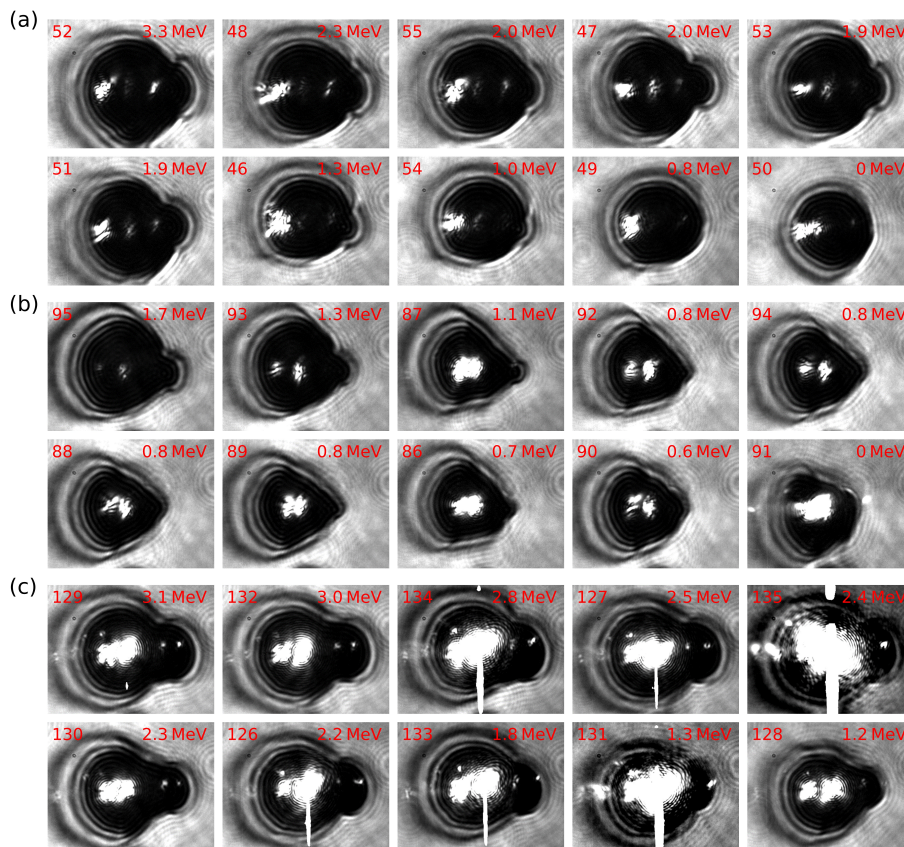


Figure 4.5.: All plasma expansion images of the shots taken at the positions $x = -8.75 \mu\text{m}$ (a), $x = +1.25 \mu\text{m}$ (b), and $x = +11.25 \mu\text{m}$ (c) (see scan shown in Fig. 4.4) are displayed here for the delay $T_0 + 150 \text{ ps}$. The images were sorted by the maximum proton energies (top right of each image, top left is the shot number within the scan) of the respective shots.

other eight shots taken at this position. Overall, the plasma expansion is smaller for shots with very low proton energies than for the shots that produced higher energies. As a consequence, the size of the plasma expansion can be correlated to the proton acceleration process. The reason for this is that the electric field responsible for accelerating ions and protons to kinetic energies of several MeV also triggers the plasma's expansion. The process of ion acceleration is also often theoretically described as plasma expansion into the vacuum (see Sec. 2.4.1.3). Since the electric field is determined by the density of hot electrons, it is correlated to the transfer of laser energy to the plasma, and thus to the size and form of the plasma expansion, the latter being visible at later times. The presence of a pre-plasma changes this expansion behavior as well as the achievable maximum proton energies, as seen in the following.

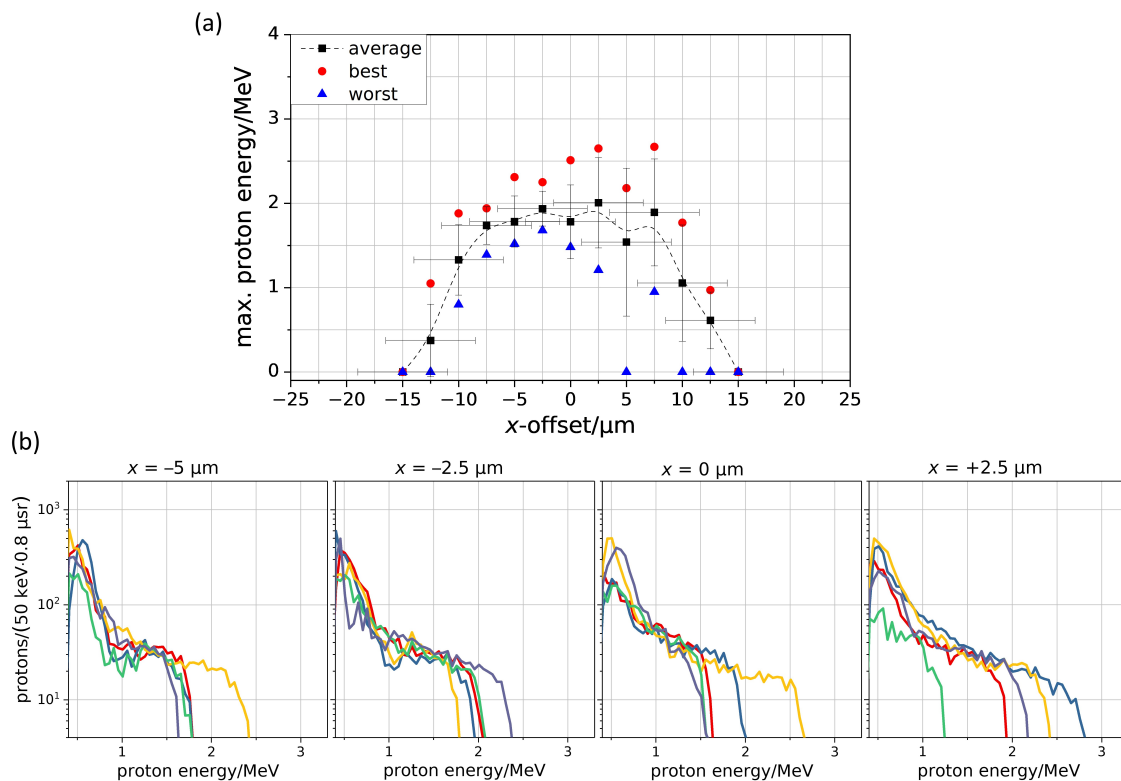


Figure 4.6.: (a) shows the maximum kinetic energy of the accelerated protons as a function of the droplets' position along the x -axis for the interaction of the pre- and main laser pulse with the droplets. The total scan consists of 65 consecutive shots taken between $x = -15 \mu\text{m}$ and $x = +15 \mu\text{m}$. Here, five shots at each position were taken except for $x = +12.5 \mu\text{m}$ (6 shots) and $x = +15 \mu\text{m}$ (4 shots). The black squares with error bars are the mean values with standard deviations of all shots taken at the respective position, again including the shots with 0 MeV. The highest and the lowest proton energy are represented by red circles and blue triangles, respectively. In (b), the spectra of all 20 consecutive shots taken at the positions $x = -5 \mu\text{m}$, $x = -2.5 \mu\text{m}$, $x = 0 \mu\text{m}$, and $x = +2.5 \mu\text{m}$ are presented (5 shots per position).

In Fig. 4.6, the maximum proton energy for different droplet positions along the x -axis is shown together with the spectra of 20 consecutive laser shots when the pre-pulse arriving at $T_0 - 5.2 \text{ ps}$ was applied, too (see Fig. 4.2 (b)). In Fig. 4.6 (a), it can be seen that the maximum proton energy has significantly increased for normal laser incidence ($x \approx 0 \mu\text{m}$) due to an increased laser absorption of the main pulse within the pre-plasma when compared to the case without the pre-pulse (Fig. 4.4 (a), $x \approx 0 \mu\text{m}$). With the applied pre-pulse, the average proton energy is relatively constant for droplet positions between $x = -7.5 \mu\text{m}$ and $x = +7.5 \mu\text{m}$. Also, the

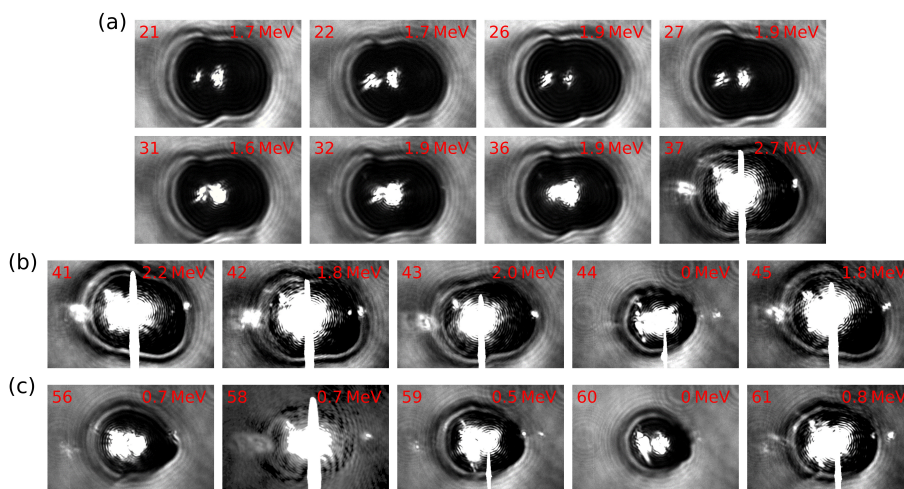


Figure 4.7.: Images of the plasma expansion of the position scan along the x -axis with the applied pre-pulse (see Fig. 4.6) for the delay $T_0 + 150$ ps. The upper left number corresponds to the shot number within the scan, while the upper right number is the maximum proton energy. (a) displays the plasma expansion for the first two shots taken in each case at the positions $x = -5 \mu\text{m}$ (21, 22), $x = -2.5 \mu\text{m}$ (26, 27), $x = 0 \mu\text{m}$ (31, 32), and $x = +2.5 \mu\text{m}$ (36, 37). In (b) are the expansion images for all five shots taken at $x = +5 \mu\text{m}$ shown, while (c) displays five of the six images captured at $x = +12.5 \mu\text{m}$. Shot 57 is not shown since the camera saturation is stronger than for shot 58.

standard deviation for the maximum proton energies for positions between $x = -7.5 \mu\text{m}$ and $x = +2.5 \mu\text{m}$ is mostly smaller for the pre-pulse case when compared to the irradiation under large incidence angles without the pre-pulse ($x \approx \pm 10 \mu\text{m}$ in Fig. 4.4). The comparison of the corresponding proton energy spectra also confirms that the shot-to-shot stability is indeed higher for the case with the pre-plasma when comparing the spectra of the 20 consecutive shots taken (Fig. 4.6 (b)) between the positions $x = -5 \mu\text{m}$ and $x = +2.5 \mu\text{m}$, with 10 consecutive shots that were taken for the grazing incidence case without a pre-plasma (Fig. 4.4 (b), $x = +11.25 \mu\text{m}$). However, higher proton energies on a single shot basis were measured for the case of grazing incidence without a pre-plasma.

Additionally, the shape of the plasma expansion changed when the pre-pulse was introduced, as can be seen in Fig. 4.7. In (a), the plasma expansion images of the first two shots taken at each position between $x = -5 \mu\text{m}$ and $x = +2.5 \mu\text{m}$ are shown. All droplets show an oval shape, and no significant bulge to the right side is visible in contrast to the scan without the pre-pulse. The independence of the plasma shape indicates that the acceleration process is similar for the different

droplet positions.

In Fig. 4.7 (b), the plasma expansion images of all five shots taken at $x = +5 \mu\text{m}$ are displayed. Four images show a similar expansion characteristic, like the expansion seen in (a), except shot 44. Here, the plasma expansion is quite small, and the shot produced no signal on the TP's MCP detector. This shot is responsible for the large standard deviation at $x = +5 \mu\text{m}$ in Fig. 4.6. To investigate what happened at this particular laser-droplet interaction, it can be compared to the plasma expansion images captured at $x = +12.5 \mu\text{m}$ (see Fig. 4.7 (c)). Here, the droplets were intentionally moved out of the laser's focus position and thus mostly missed. Shot 59, which produced a MCP signal just above the TP's low energy cutoff, and shot 60, which produced no MCP signal, are a bit larger and smaller, respectively, than shot 44 shown in (b). Consequently, the plasma expansion is an indication that the laser pulse likely missed the droplet for shot 44.

4.4. Simulations and interpretation

2D-PIC simulations with the code EPOCH were performed to get a better understanding of the differences in the proton acceleration process for the different cases of irradiation [140].¹ The simulation box extended from $-15 \mu\text{m}$ to $15 \mu\text{m}$ in both axes with 200 cells/ μm . The main laser pulse was modeled as Gaussian in both time and space with a central wavelength of $\lambda_L = 400 \text{ nm}$ and a normalized vector potential of $a_0 = 2.5$. The FWHM-pulse duration was $\tau_L = 42 \text{ fs}$. The laser pulse was focused into a FWHM-spot with $d = 0.6 \mu\text{m}$ located at the center of the simulation box ($z = 0 \mu\text{m}$, $x = 0 \mu\text{m}$). The droplets were implemented in 2D as disks with a radius of $2.5 \mu\text{m}$ and a maximum electron density of $n_e = 30n_c$. The diameter of the laser focus and the simulated droplets/disks were reduced with respect to the experiment by a factor of 2 and 4, respectively, due to computational reasons. For every six electrons, two protons and one O^{4+} ion were implemented in the simulation. The number of particles per cell was 20. The initial temperature of all plasma components was set to 1 keV. Two different laser irradiance geometries were simulated. For the off-axis/grazing incidence case, without the additional pre-plasma, the droplet was centered around the point ($z = 2.5 \mu\text{m}$, $x = -2.5 \mu\text{m}$), while for normal laser incidence, the droplet's center was positioned at ($z = 2.5 \mu\text{m}$, $x = 0 \mu\text{m}$). For each

¹The simulations were performed by Stefan Tietze. The simulation data was analyzed by myself with open-source software [174–177].

of these two irradiation geometries, a simulation was first carried out without a pre-plasma.

The pre-plasma was modeled as Gaussian-shaped in 2D with an exponential density profile and was attached to the droplet (see Sec. 4.2) for the normal irradiation geometry. To account for unavoidable uncertainties in the estimation of the pre-plasma profile $L(\varphi)$, with the maximum scale length of $L_{\max} = 390 \text{ nm} \approx \lambda_L$ on the laser axis (see Sec. 4.2), additional simulations were performed with $L(\varphi) \rightarrow L(\varphi)/4$, $L(\varphi)/2$, $2 \cdot L(\varphi)$. The arrival time of the laser pulse's peak at ($z = 0 \text{ }\mu\text{m}/x = 0 \text{ }\mu\text{m}$) was $t = 171 \text{ fs} =: T_0$ after the start of the simulation.

In Fig. 4.8 (a), the simulated maximum proton energy is plotted against the on-axis scale length for the case of normal laser incidence together with the maximum proton energy for the simulation without pre-plasma and grazing laser incidence for the last recorded time step of $T_0 + 129 \text{ fs}$. Here, the maximum proton energy increases for normal laser incidence the more extended the pre-plasma is, but an optimal scale length might exist since the proton energy does not significantly change between L_{\max} and $2 \cdot L_{\max}$.

Since the experimental increase of the proton energy due to the pre-plasma for the case of normal laser incidence was about a factor of 2 to 2.5 (compare Fig. 4.4 with Fig. 4.6 both around $x \approx 0 \text{ }\mu\text{m}$), it can be assumed from the simulated results in Fig. 4.8 that the maximum scale length in the experiment was between the experimentally deduced scale length of L_{\max} and $L_{\max}/2$.

Furthermore, the simulation with off-axis irradiation (red dot in Fig. 4.8 (a)) produced protons with slightly higher energies than the simulations for normal laser incidence. This is consistent with the experimental results (compare single best shots/red dots in Fig. 4.4 with Fig. 4.6).

In the simulations, the protons emitted from the laser's point of impact exhibit even higher energies (not for the case of normal laser incidence and $L_{\max} \approx \lambda_L$), as can be seen in Fig. 4.8 (b), where the normalized distribution of the protons' momenta is shown. For the case of normal laser incidence and no pre-plasma (b_i), there are protons with higher kinetic energies or momenta, compared to the forward accelerated protons, emitted from the laser's point of impact in the direction of $\pm 160^\circ$ relative to the laser's forward axis (arrows). For the case of $L_{\max}/2 \approx \lambda_L/2$ shown in (b_{ii}), the energy of protons emitted in all directions increases. In contrast to that, there is only a further enhancement in the forward acceleration for (b_{iii}). The difference for these cases may be explained as follows. At the laser's impact

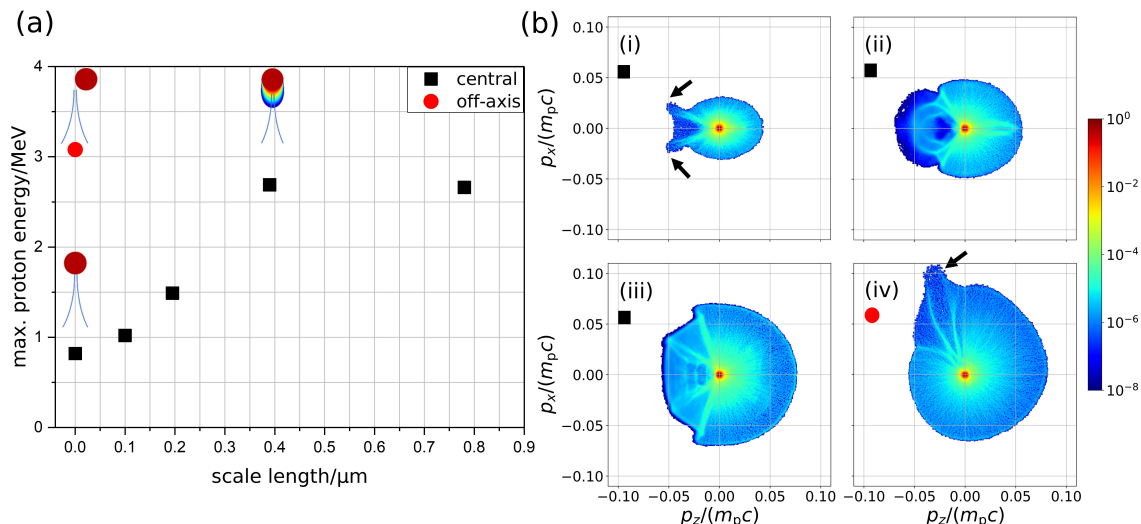


Figure 4.8.: In (a), the simulated maximum proton energy of protons emitted in laser forward direction within an angle of $\pm 1^\circ$ is plotted against the on-axis pre-plasma scale length for the delay $T_0 + 129 \text{ fs}$. The black squares are the central irradiation cases, while the red circle is the off-axis case, as indicated with the small sketches. The proton distribution in the phase space is shown in (b). ((i)–(iii)) correspond to the central irradiation of a droplet with (i) no pre-plasma, (ii) a maximum scale length of $L_{\max}/2 = 195 \text{ nm} \approx \lambda_L/2$, and (iii) $L_{\max} = 390 \text{ nm} \approx \lambda_L$ on the laser axis. (iv) is the off-axis case without a pre-plasma present.

point, hot electrons are generated and extracted from the droplet. Thus, a charge separation field in this region is induced. For the case with pre-plasma, this electric field is reduced due to the plasma scale length (see Sec. 2.4.1.2) but increases due to the higher electron temperature, which means both effects cancel each other out. On the droplets' right (the side which faces the TP in the experiment), there is no pre-plasma present. Hence, the maximum proton energy increases with the rising scale length on the droplet's front side. As a consequence, the measured proton energies in the experimental scan (pre-pulse) shown in Fig. 4.6 are likely the ones with the highest kinetic energy emitted from the droplets for these interaction conditions.

For the case of off-axis irradiation without a pre-plasma, this might not be the case. The black arrow in Fig. 4.8 (b_{iv}) points to the protons that have been emitted from the laser's incident point on the droplet. These protons have the highest momenta or kinetic energies in the simulations and have been emitted in the direction of about 105° with respect to the laser's forward direction, the latter being the direction to the TP. This occurs, as mentioned before because the hot electrons are generated at the impact region of the laser. Since there is no pre-plasma present, the electric field is

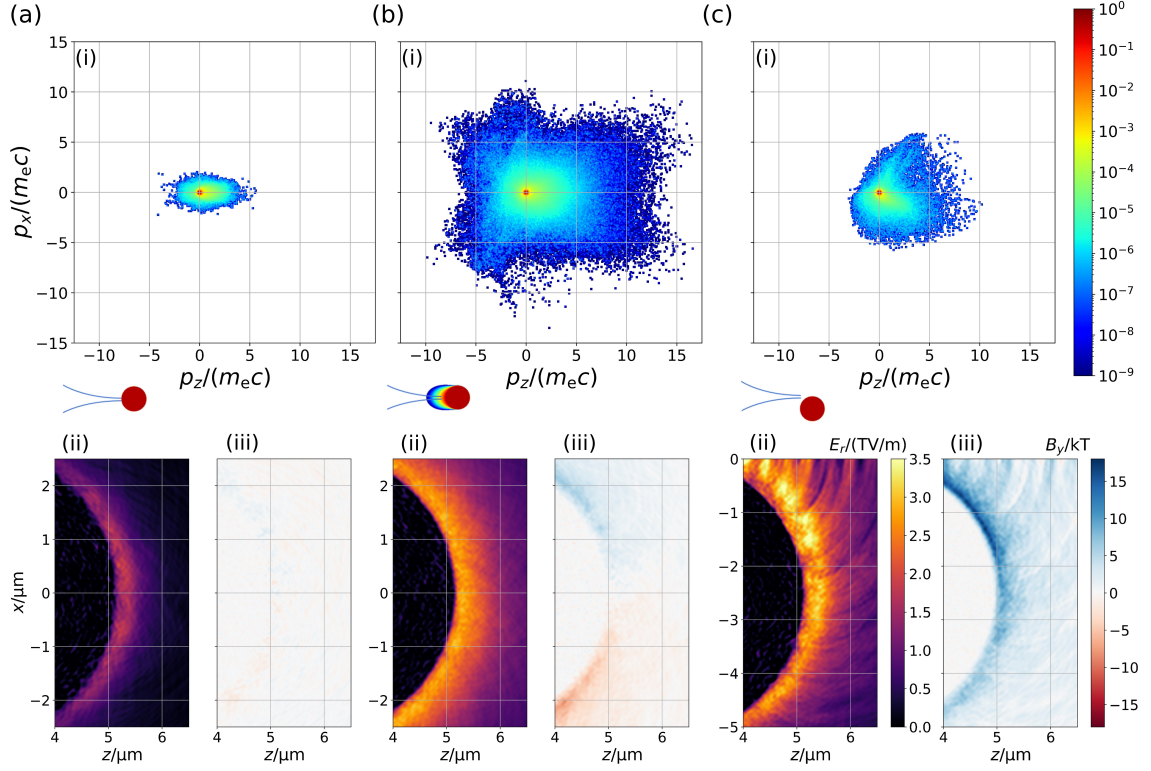


Figure 4.9.: (a_i)–(c_i) show the electron density in phase space for $T_0 + 9$ fs for the on-axis illumination of a simulated droplet without a pre-plasma (a_i), with the pre-plasma with maximum scale length $L_{\text{max}} \approx \lambda$ (b_i), and for the off-axis irradiation without pre-plasma (c_i). (a_{ii})–(c_{ii}) and (a_{iii})–(c_{iii}) show the radial electric fields $E_r(z, x)$ and the magnetic fields along the y -axis $B_y(z, x)$, respectively, for $T_0 + 29$ fs.

strongest there. As a result, the global maximum proton energy in the experimental off-axis case ($x \approx \pm 10 \mu\text{m}$, Fig. 4.4, scan without pre-pulse) may be higher than the one which was measured.

To investigate if the difference of the proton energies measured in the experiment in the laser forward direction is only due to the difference in electron heating for the different irradiance geometries and scale lengths, the normalized electron momentum distributions are shown in Fig. 4.9 (a_i)–(c_i). For normal laser incidence and no pre-plasma (a_i), electrons are preferably accelerated in the laser forward direction, which means through the droplet, probably due to the oscillating component of the $\vec{j} \times \vec{B}$ -force (see Sec. 2.3.2.4).

When the laser is incident on a pre-plasma ((b_i), $L_{\text{max}} \approx \lambda$), the momenta and the number of the hot electrons increase with increasing scale length, as expected,

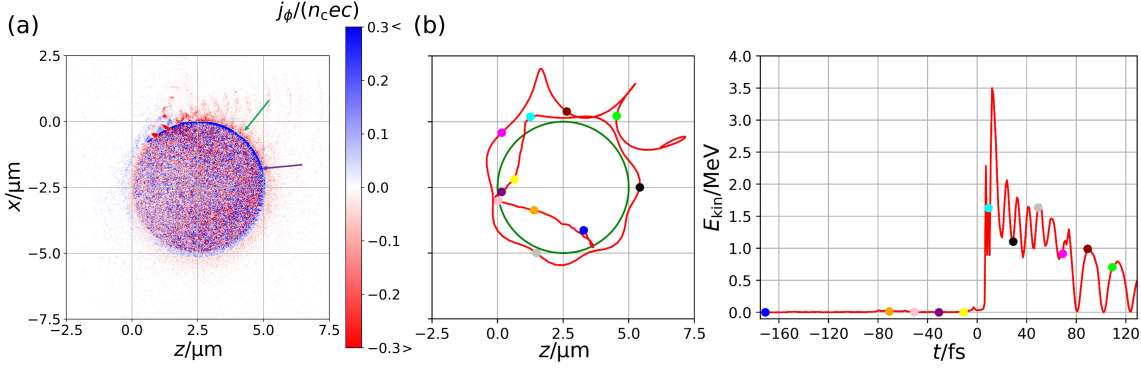


Figure 4.10.: In (a) the azimuthal, normalized electron current density is displayed for the simulated off-axis irradiation case (see Fig. 4.9 (c)) for the time $T_0 + 29$ fs. Note that values higher or smaller than the maximum/minimum numbers on the color bar are displayed as these values to emphasize the significant currents. The red distribution displays the hot electron current moving clockwise (green arrow). Blue is the return current that moves counter-clockwise (purple arrow). In (b) the trajectory (left) and the evolution of the kinetic energy (right) of a single, hot electron is displayed. In both plots, the blue dot denotes the start of the simulation $T_0 - 171$ fs. The orange dot denotes the position and kinetic energy at $T_0 - 71$ fs. Afterwards, for each dot 20 fs have been added.

especially in the forward direction. This explains why the energy of the accelerated protons rises with increasing scale-length, as seen in Fig. 4.8 (a).

However, the enhancement in heating alone cannot explain the high proton energies for grazing laser incidence since, in this case, the electrons are heated much less (Fig. 4.9 (c_i)) than for the case with pre-plasma in (b_i). Nevertheless, the electric field at the droplet's rear surface (Fig. 4.9 (c_{ii}), grazing incidence without a pre-plasma) is stronger than in the other cases. Since the TNSA field is due to charge separation, this stronger electric field has to be the consequence of a higher electron density rather than a higher electron temperature.

This localized hot electron density can be explained as follows [196, 197]. When the laser pulse illuminates a droplet under grazing incidence, part of the laser's electric field points into the droplet and heats electrons. A fraction of these hot electrons gets accelerated into the droplet, but there are also electrons that get dragged out of the droplet. The electrons that are dragged out of the droplet are likely the reason for the high electric field that causes the acceleration of protons from the laser's impact region. A part of the dragged out electrons is pushed in the forward direction by the laser pulse close to the droplet's surface. Due to the magnetic

field generated by this hot electron current, a cold return current is induced (see Sec. 2.4.1.1) within the droplet but close to its surface. These two currents are visualized in Fig. 4.10 (a). Together, they generate a magnetic field located close to the droplet's surface, which points in the positive y -direction (Fig. 4.9 (c_{iii})). As a consequence, the magnetic component of the Lorentz force (Eq. 2.3) pushes the electrons away from the droplet's surface in the radial direction. The electric field due to the charge separation between electrons and the droplet, on the other hand, pulls the electrons back. Since the magnetic field is located closer to the droplet surface than the charge separation field, the electrons get confined by these two fields. As a consequence, this enhances the electric field due to the more localized electron charge density.

Such surface currents were also simulated and measured when using foil targets [198–200]. This electron confinement is likely the reason why off-axis irradiation on a steep plasma gradient generates protons with higher kinetic energies.

Fig. 4.10 (b) shows the trajectory of a single, hot electron (left) together with its kinetic energy as a function of simulation time to look deeper into the dynamics of this interaction. At the beginning of the simulation ($T_0 - 171$ fs), the electron is inside the droplet (blue dot). The trajectory of the electron can be interpreted as follows. Due to the rising intensity of the laser pulse, electrons are dragged out of the droplet at the laser's impact position, which causes a charge imbalance within the droplet. Due to this, the electron moves slowly towards this position. Shortly after the pulse peak, the electron is extracted into the vacuum by the laser (cyan dot). It is then accelerated forward and has maximum kinetic energy when it is close to the droplet. The magnetic field close to the droplet's surface prevents the electron from entering the droplet again. When the distance to the droplet is maximal, the kinetic energy takes a minimum until the electron is accelerated back to the droplet by the electric field, which increases the kinetic energy. The electron oscillates in this way around the droplet. At the end of the simulation, when the electron arrives at the laser's impact region again, the amplitude of the trajectory grows larger, since the electric field is now localized further away from the droplet's initial surface due to the expanded plasma. Since this electron has a high kinetic energy and its position at $T_0 + 29$ fs is behind the droplet ($z \approx 5.4 \mu\text{m}$, $x \approx -2.5 \mu\text{m}$), electrons performing similar motions likely contribute to the enhanced electric field in Fig. 4.9 (c_{ii}).

In summary, the increase of the maximum proton energy for normal laser incidence and an additional pre-plasma could be explained as well as the high proton energies

for grazing irradiation of a droplet without a pre-plasma.

However, when comparing the grazing irradiation ($x \approx \pm 10 \mu\text{m}$) of a droplet without the pre-plasma (Fig. 4.4) and with the pre-plasma (Fig. 4.6), it can be seen that the lateral irradiation geometry did not increase the maximum ion energies for the case of the pre-plasma. This may be a result of a vanished or reduced surface current. Li *et al.* [198] observed that the more pre-plasma was present on the irradiated surface, the lower was the amount of surface electrons. The reduction of the surface current may be explained as follows. Without a pre-plasma, the hot surface current is a consequence of the electric and magnetic fields close to the droplet surface. If a pre-plasma with a long scale-length is present at the laser's impact position, two consequences arise. Firstly, the TNSA field at this position is reduced due to the plasma's scale length unless this reduction could be compensated by an increase in electron temperature. Secondly, there are electrons outside the former droplet surface in the pre-plasma present, which cause an extended cold return current instead of a localized one. This delocalization of the cold return current eventually leads to a weaker magnetic field. These reduced fields would then produce a less confined hot surface current and a reduction of the electron density at the droplet's rear side, counteracting the effect of increased heating in the pre-plasma.

4.5. The proton beam profile

In Sec. 4.3, the influence of the target position and an additional pre-plasma on the protons, which were accelerated in the laser forward direction within a small solid angle, was presented.

To transport and use a large fraction of the accelerated protons for applications, it is also necessary to investigate the proton beam's characteristics within a larger solid angle. Hence, additional measurements of the proton beam's spatial distribution were performed (see Sec. 3.1.2 for a description of the diagnostics).

4.5.1. Experimental results

Due to the combination of the plastic scintillator and the G-CCD, the proton beam profile could be measured together with the maximum proton energies and the plasma expansion. In Fig. 4.11, exemplary images of these measurements are presented for shots, for which the maximum proton energies were around 3 MeV. These

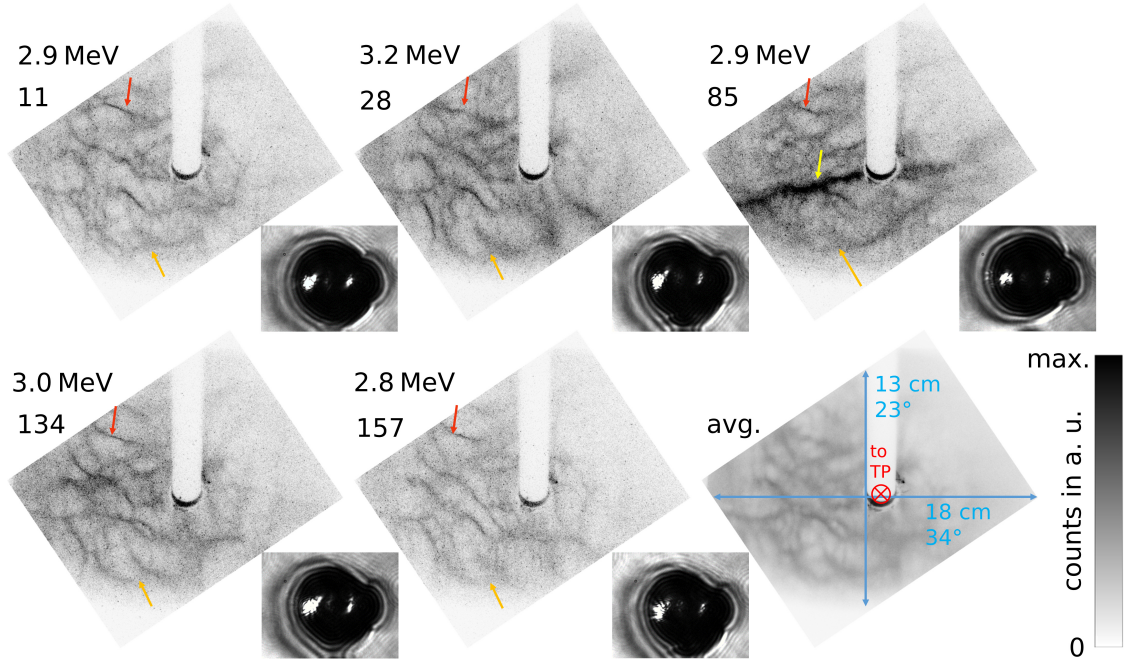


Figure 4.11.: The first five images show measurements of the proton beam profile captured within a scan of 167 consecutive shots in total. The lower number is the shot number within this scan, while the upper number is the corresponding maximum proton energy as detected by the TP. The small images in the lower right show the corresponding plasma expansion for the delay $T_0 + 150$ ps. Shots 11 and 28 correspond to the first two shots within this scan with a maximum proton energy of approximately 3 MeV. Shot 85 was taken in the middle of the scan, while the last two beam profiles correspond to the last two shots with $E_{\max} \approx 3$ MeV within this scan. The sixth image is an average of the 50 best shots ($3.3 \text{ MeV} \geq E_{\max} \geq 2.5 \text{ MeV}$) out of the total scan. The G-CCD was set to observe the signal originating mainly from protons with kinetic energies of $1.1 \text{ MeV} \leq E_p \leq E_{\max}$. During this scan, the nozzle was not moved. The droplets were irradiated on the side facing away from the probe objective. Not the entire scintillator was imaged onto the camera chip. Also, a part of the image was blocked by the viewport into the vacuum chamber. The maximum full horizontal opening angle that was covered by the scintillator was $\approx 34^\circ$, while in the vertical axis the maximum acceptance angle was $\approx 23^\circ$, as indicated in the lower right image.

images were captured within a scan consisting of 167 shots in total, in which the droplets were irradiated on the side facing away from the probe objective. This position corresponds to the left maximum of the proton energy as a function of x , as shown in Fig. 4.4. Each of the five exemplary beam profiles shows spatial modulations, especially on the left side of the scintillator. The shape of these modulations seems quite similar for different shots, especially when comparing the shots 11, 28,

134, and 157. Exemplary structures that can be seen in each of the five images are indicated by red and orange arrows. The red arrows point to a horizontal line, which corresponds to a region with a high particle density, while the orange arrows point to a structure of two curved lines. These lines will be called filaments in the following, while the regions of reduced proton density will be named bubbles. These two features indicated by the arrows can be seen even in the beam profile of shot 85, which shows some differences to the other four beam profiles, in particular, a very pronounced, long filament (yellow arrow). The reason for this different beam profile might be that the laser irradiated the droplet at a slightly different position. This difference can be deduced from the different shapes of the plasma expansion, which is also shown Fig. 4.11. For shot 85, the irradiated droplet did expand a little more upwards than in the other four shots, which indicates a slightly different position of the laser with respect to the droplet along the vertical axis. Nevertheless, the spatial distribution of the accelerated protons was, in general, quite stable during this scan. The beam profile was averaged over the 50 best shots of this scan to illustrate this. The averaged beam profile is shown as the sixth image in Fig. 4.11.

The droplets' lateral position in relation to the laser's focus position has, indeed, a strong influence on the proton beam's profile. To emphasize this, beam profile measurements that were taken at the position of the right maximum in Fig. 4.4 ($x = +11.25 \mu\text{m}$), and are displayed in Fig. 4.12 (a), are compared to those shown in Fig. 4.11. The strong modulations on the left side of the scintillator have different patterns for the two irradiation cases. Additionally, the proton distribution on the scintillator's right side has a higher density and is more homogeneous for the irradiation geometry considered in Fig. 4.12 (a). The differences between shots 129, 132, and 134 might be attributed again to a slightly different irradiation geometry since the plasma expansion behavior is also slightly different. Again, exemplary structures that are similar for each of the three beam profiles are indicated by the arrows (red and yellow).

Fig. 4.12 (b) shows spatial distributions of accelerated protons that were captured during the scan with the applied pre-pulse at $x = +7.5 \mu\text{m}$ (see Fig. 4.6). As a consequence, the droplets were irradiated on the side facing the objective, as the shots in (a). Shots 46 and 49 have a quite similar pattern, while shot 50 is slightly different, probably again due to a small difference in the irradiation geometry. In general, the distributions in (a) and (b) are comparable. All images show a relatively homogeneous signal on the right side and significant modulations on the left.

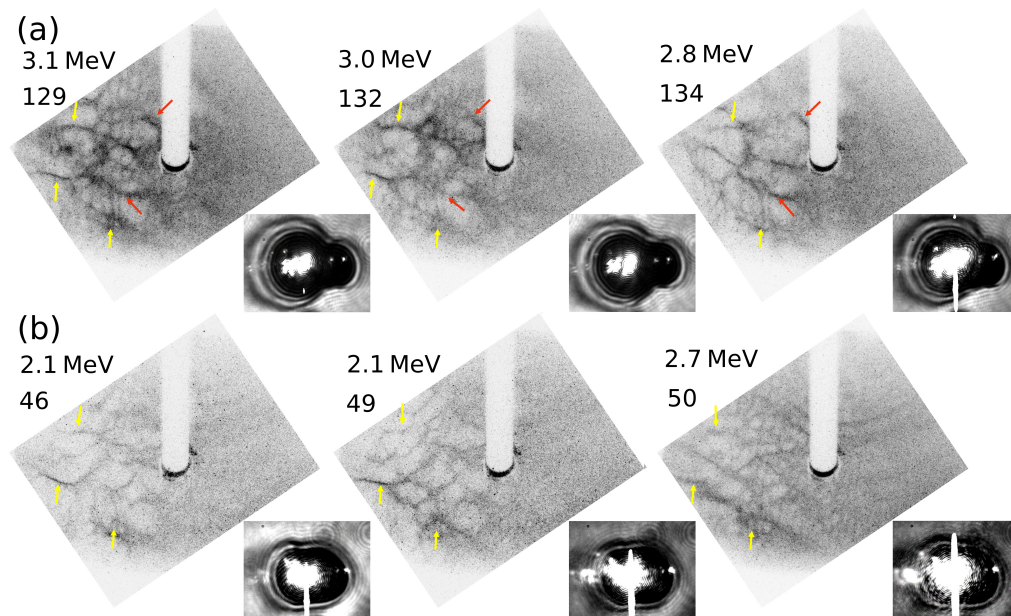


Figure 4.12.: (a) shows the beam profiles of the three shots with the highest proton energies taken at the position $x = +11.25 \mu\text{m}$ during the scan shown in Fig. 4.4. Thus the shot numbers correspond to the respective shots within that scan. (b) displays the beam profiles from the three best shots taken at $x = +7.5 \mu\text{m}$ during the scan with the applied pre-pulse, which was shown in Fig. 4.6. Note that the pixel counts for shots 46 and 49 were multiplied by a factor of 2 to account for the reduced signal strength.

Features of the modulation patterns that are identical in both cases are indicated by the yellow arrows.

However, it cannot be excluded that there may be conditions for proton acceleration with droplets that cause the modulations to vanish or change their shape significantly because the signal strength of the measurements depends on the kinetic energy and number of particles hitting the scintillator (see Sec. 3.1.2). For the conditions in this experiment, the signal strength of the scintillator started to be high enough to make a statement about the beam profile as soon as the maximum proton energy was around 2 MeV. As a consequence, it was not possible to verify if the modulations vanish or change significantly when the droplets were irradiated under central irradiation and without a pre-pulse ($x \approx 0 \mu\text{m}$ in Fig. 4.4). In this scan, the maximum proton energy was, on average, lower than the threshold energy, which is necessary for protons to pass through the aluminum foil shielding the plastic scintillator. For the scan with the applied pre-pulse and central irradiation ($x \approx 0 \mu\text{m}$ in Fig. 4.6), not enough shots produced a signal strong enough to allow a statement to be made.

With the scintillator measurements only, it was not possible either to investigate the beam profile for small energy intervals close to the maximum proton energies. That would provide information as to whether the cutoff of the proton energy spectrum depends on the location within the proton beam's spatial distribution or not. Additionally, the scintillator covered a relatively small angle in the forward direction. Further measurements were necessary to investigate the size of the modulated region and if there are regions that exhibit a homogeneous spatial distribution of the accelerated protons.

These measurements were performed by placing CR-39 detector plates, shielded with aluminum foil, at a distance of 7.3 cm to the target. An exemplary piece of CR-39, which has been etched in 6.25 mol NaOH for 90 min at 85 °C, is shown in Fig. 4.13 (a), which was divided into three regions, each shielded by a different aluminum foil thickness. In the small central region in the center, no proton craters are visible since the maximum proton energy measured with the TP was about 1.8 MeV which was below the threshold energy for this region.

In the upper part of the CR-39, protons with kinetic energies below 1 MeV were blocked. The modulations cover a limited area around the laser's forward axis, while to the left and in the upward direction, the proton density is homogeneous. However, since the CR-39 only covered the region that is oriented to the left of the laser's forward axis (side of the probe objective), no clear statement about the right half-space can be made. However, since the scintillator measurements for comparable irradiation geometries (Fig. 4.11 (a)) also show modulations on the right side, it can be concluded that these modulations appear, at least to some extent, on this side of the laser's forward axis. Images taken from the modulated region with an optical microscope and two different magnifications are shown in (b). These images show an example of a transition between an area of low proton density (bubble) to a region of higher proton density (filament).

Due to the maximum proton energy of 1.8 MeV for this shot, the protons detected in the lower part of the CR-39 (threshold energy of 1.6 MeV) have kinetic energies close to this value. As in the upper region, the protons' spatial distribution is strongly modulated near the laser's forward axis. These modulations are encircled by a border region of a more homogeneous crater density (orange arrow), which decreases to zero in the outward direction. An example of a transition from a filament to a bubble is shown in the magnified images in (c). In the two enlarged image sections, the number of protons within the filament (≈ 230 protons) is about a factor of ≈ 4.6

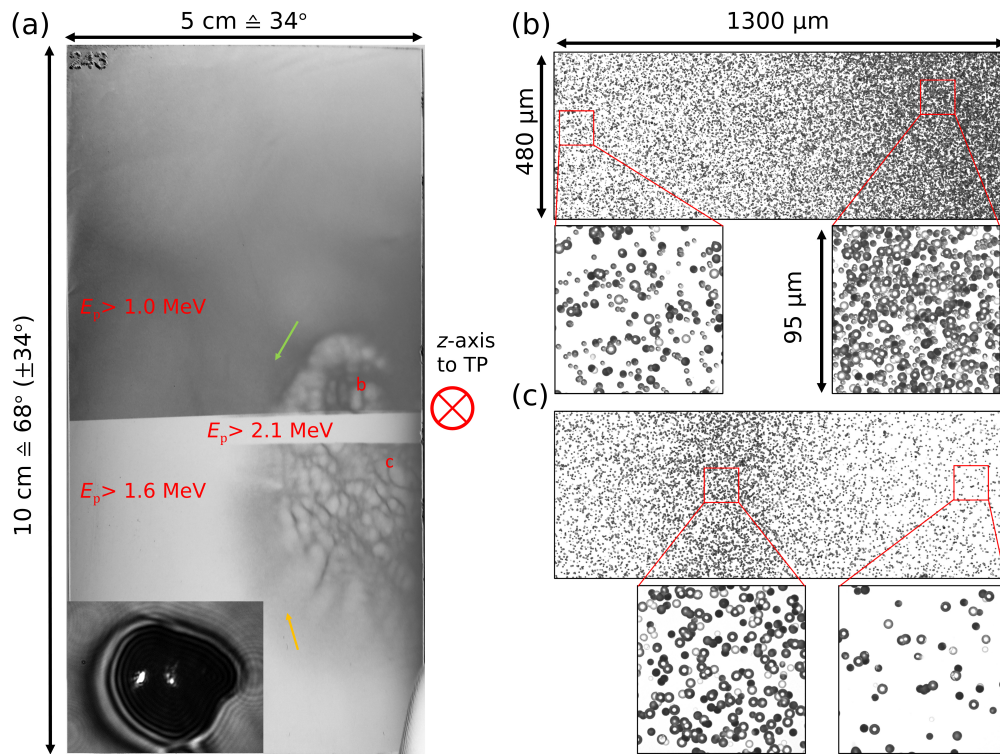


Figure 4.13.: (a) shows the front surface of a CR-39 nuclear track detector, which was placed at a distance of $7.3\ \mu\text{m}$ from the target, as indicated in Fig. 4.1 (a). The piece of CR-39 was placed to the left of the laser's forward axis and covered a horizontal opening angle of 34° in the left half-space. The full angle covered along the vertical axis was about 68° . The CR-39 detector was divided into three different regions, each shielded with aluminum to block protons below a particular energy. These threshold energies are 1.0 MeV (upper region, $15\ \mu\text{m}$ thick aluminum foil), 1.6 MeV (lower region, $30\ \mu\text{m}$ aluminum) and 2.1 MeV (small central region, $45\ \mu\text{m}$ aluminum). The maximum proton energy for this shot measured with the TP was $E_{\text{max}} \approx 1.8\ \text{MeV}$. The droplet was irradiated on the side facing away from the probe objective, as indicated by the plasma expansion, which is displayed in the lower-left corner of the CR-39. For this shot, a pre-pulse was applied, which arrived approximately $0.7\ \text{ps}$ before the main laser. (b) and (c) show images taken with an optical microscope of the two regions indicated with red letters in (a).

higher than in the bubble region (≈ 50 protons).

The differences in particle numbers in the modulated area of the beam profile has likely direct consequences for the measurement of the proton energy spectrum with the TP in the laser's forward direction. The projected aperture of the TP at the distance of $7.3\ \text{cm}$ to the target is $\approx 70\ \mu\text{m}$ in diameter. That is smaller than the

microscope images with the highest magnification in Fig. 4.13. Consequently, the amount of particles detected by the TP depends on the relative position of the aperture within the beam profile. However, due to the stability of the modulations, if the droplets' position is not changed, it is unlikely that significant variations of the absolute number of protons are measured for consecutive laser shots due to the beam profile's modulations. In contrast to the number of particles, the maximum proton energy likely shows only small changes as a function of the detection direction since protons are detectable in the bubbles and the filaments of the lower part of the CR-39 in Fig. 4.13 and not in the center.

Since the modulations of the proton beam were reproducibly generated, they can be considered as characteristic for laser-driven proton acceleration with droplets, at least for the laser parameters considered here. Furthermore, such modulations were also observed in a different experiment with droplets, in which the fundamental of the JETI40 laser was used instead of the 2ω -pulses, which led mainly to a reduced TIC, higher laser pulse energy, and larger focal spot [191].

Comparable patterns in the protons' spatial distribution were observed in several experiments, in which various types of targets were used. In experiments performed at the VULCAN laser facility, modulated beam profiles were observed when foils with a thickness of a few nanometers were irradiated [172, 201]. The occurrence of the modulations was attributed to the Rayleigh-Taylor instability caused by the pressure of the laser on the thin plasma in the light-sail regime (see Sec. 2.4.3.2) [201]. However, for foils with thicknesses of 30 nm and 50 nm, no such beam patterns could be observed. Since the droplets' diameter is much larger than the thickness of such foils, it is unlikely that the Rayleigh-Taylor instability causes the modulations in the case of droplets.

Similar structures were also observed when micrometer thick metal foil targets or cylindrical jets of frozen, solid hydrogen were used at experiments performed at the DRACO and PHELIX laser systems [202–204]. For the experiments and simulations described in [203, 204], their occurrence was attributed to the so-called Weibel Instability (WI) that causes the generation of transverse magnetic and electric fields that focus or defocus the protons [205]. The WI arises in a pre-plasma present at the target's rear side. In this pre-plasma, the return current necessary to compensate the hot (relativistic) electron current (see Sec. 2.4.1.1) is unstable and amplifies magnetic field fluctuations [203].

As a criterion for the minimum scale length necessary for the WI to grow at the

target's rear surface, Göde *et al.* [203] give $L \geq c\Gamma_{\text{Wi}}^{-1}$ with $\Gamma_{\text{Wi}} \approx (v_r/c)\omega_r/\sqrt{\gamma_r} = (v_r/c)\sqrt{n_r/n_e}\omega_L/\sqrt{\gamma_r}$ as the growth rate of the WI. v_r , ω_r , γ_r , and n_r are the mean velocity, plasma frequency, gamma factor, and density of the return current electrons, respectively. The growth rate of the WI is maximized when the return current electrons in the corresponding region are relativistic, and n_r is comparable to the hot electron density n_e . With the hot electron density estimated in Sec. 2.4.1.1 ($n_e \approx n_r \approx 5 \cdot 10^{19} \text{ cm}^{-3}$), the gamma factor $\gamma_r \approx \sqrt{1 + a_0^2} \approx 2.3$ (Sec. 2.2.1), and the approximation of $v_r \approx c$, the minimum scale length necessary for the WI to take place is roughly $L \approx 1.1 \mu\text{m}$ for $\lambda_L = 0.4 \mu\text{m}$. Such an extended pre-plasma was not observed during the arrival of the main pulse at the target's rear side (see Sec. 4.2). However, the estimation of the minimum scale length depends on a rough estimation of the hot electron density. It cannot be excluded that a significantly higher electron density was generated in the experiment, for example, due to the confinement of hot electrons close to the droplets' surface, as described in Sec. 4.4. As a result, the necessary scale length for the WI to occur would be smaller.

One argument against such instabilities as a possible explanation for the modulated beam profile is its stability. This stability, however, is an argument for another possible explanation that was given by Obst *et al.* [206]. In experiments at the DRACO laser with solid hydrogen jets and tungsten wires, they detected structures within the modulated beam profiles that corresponded to objects placed in the beam path of the collimated laser beam. In the case of a tungsten wire, the structures and modulations were only present when the pressure in the vacuum chamber was increased to $\approx 1.6 \cdot 10^{-3} \text{ mbar}$. Thus, the background gas could be identified as being critical for the appearance of the beam profile. The target, which was in their experiment smaller than the laser focus, blocked the central parts of the laser pulse that contain the low spatial frequencies. The remaining transmitted laser light ionized the background gas on a length scale of millimeters and imprinted its spatial intensity profile into it. The accelerated protons then propagated through these regions of low-density plasma and experienced transverse quasistatic electric fields that accelerated them according to the laser's intensity modulations.

Gas, locally even with a higher density, was also likely present in the droplet experiment close to the target since liquid water evaporates when ejected into a vacuum. However, since the properties of this gas corona were not investigated in the experiment, no statements can be made for the molecular density at a certain distance from the target.

Although the laser focus in the experiment was much smaller than the droplets (see Sec. 4.1), there was probably still enough laser light far outside the laser's focal region to ionize the four droplets close to the central irradiated droplet, as seen in Fig. 4.2. Consequently, it is possible that also gas behind the droplets might have been ionized on a length scale of hundreds of micrometers. That could especially be the case when the droplets were irradiated on their side so that more intense laser parts could pass around the droplets. Thus, the measurement of the transmitted laser light as a function of the droplets' position and its comparison with the measured beam profile would give more insight into the physics and more control over the acceleration process itself.

4.6. Summary and discussion

Within this chapter, the interaction of high-intensity frequency-doubled laser pulses with water microdroplets was investigated. The droplets' position concerning the laser's focus along the polarization axis was varied, and the energy spectra of protons accelerated in the laser forward direction were measured. When the droplets were irradiated centrally with these contrast-enhanced laser pulses, the maximum proton energies were, on average, clearly below 1 MeV. With a pre-pulse applied, this maximum proton energy could be enhanced in this irradiation geometry to about 2 MeV. With the help of PIC simulations, this improvement of the proton acceleration could be attributed to the generation of more electrons with higher kinetic energies in the generated pre-plasma.

However, slightly higher proton energies on a single shot basis were achieved without the pre-pulse and when the droplets were irradiated under grazing incidence. Despite the higher proton energies, the simulations showed a reduced generation of hot electrons compared to the case with applied pre-pulse and normal incidence. But in this irradiation geometry, a hot electron population is accelerated parallel to the droplets' surface. Consequently, a magnetic field is generated that – together with the charge separation field between droplets and electrons – confines the electron current close to the surface [196–200]. This hot electron population close to the surface, in turn, enhances the electric field, eventually leading to higher maximum proton energies.

With the optical probe laser of the JETI 40 [59–61] filtered to a narrow wavelength band between 1ω and 2ω , it was possible to monitor the interaction of the pre-

pulse and the main pulse with the droplets. Hence, it was possible to estimate the pre-plasma generated by the pre-pulse alone and use this information as input for the PIC simulations. Furthermore, it was possible to observe the droplets' plasma expansion induced by the main pulse on a picosecond timescale. The size and shape of this expansion correlate with the measured maximum proton energies since they depend not only on the irradiation geometry but also if a pre-plasma is present or not.

Besides the proton acceleration in the laser's forward direction and the plasma expansion, also the proton beam profile was measured in a larger solid angle areal around the laser's forward axis. This proton beam's spatial distribution exhibits significant spatial modulations. It could be shown that the beam profile, i.e., the structure of these modulations depends on the irradiation geometry as well. When the droplets' position was not changed, the shape of the modulations remained relatively stable. That indicates that these modulations are directly related to the laser's electric field, as described by Obst *et al.* [206]. By ionization of the background gas in the vacuum chamber close to the target, high-frequency modulations of the laser's electric field can be imprinted into the gas and thus be transferred onto the accelerated proton beam. An alternative origin of the modulations may be the occurrence of instabilities, like the Weibel instability, which manifests itself in a pre-plasma at the target's rear surface [203, 204]. This explanation is less likely because of the beam profile's stability and the lack of a pre-plasma at the droplets' surface facing the detectors. Further experiments are necessary to clarify the origin of these modulations. For this purpose, measurements of the transmitted laser light for a comparison with the protons' beam profile are necessary. The amount of transmitted light could be varied via changes in droplet and focus size. Also, a further investigation of the influence of the target's geometry would be interesting since a difference in the shape of the beam profile for cylindrical hydrogen and droplets could be observed in [191]. For example, the beam profile of protons originating from water microdroplets could be compared to the one that originates from a water curtain that is generated by two colliding liquid jets [207].

5. Summary

In the context of this thesis, different aspects of laser-driven ion acceleration with contrast-enhanced laser pulses were characterized to obtain a deeper understanding of the acceleration process itself.

In an experiment with a plasma mirror at the POLARIS system, the thickness of carbon foils was continuously decreased from 500 nm down to 5 nm to study possible ways to increase the energy of the accelerated protons and carbon ions. For linearly polarized laser pulses, a significant increase of the maximum ion energies up to an intensity of $\approx 9 \cdot 10^{19} \text{ W/cm}^2$ was measured for the 5 nm thin foil due to a steeper scaling with the laser pulse energy compared to thicker foils. However, with increasing intensity, the particles' kinetic energy did not rise further. This stop correlates to the onset of transparency of the foil. Although the use of circular polarization was expected to be beneficial for ion acceleration via RPA, it did only lead in the case of the 5 nm thin foil, in general, to similar ion energies for higher laser pulse energies. For thicker foils, circular polarization did lead to reduced ion energies, which is likely a consequence of reduced electron heating. To exploit the better scaling of the ion energies for the thinnest foils, further improvements of the TIC and an increase of the available laser pulse energy are necessary. For this purpose, the POLARIS laser system will be improved.

Besides the measurement of maximum ion energies, the protons' spatial distribution is an observable that allows conclusions to be made about the acceleration process. In an experiment with the second harmonic of the POLARIS laser and foils with thicknesses between 800 nm and 100 nm, the occurrence of a ring-like-structure formed by protons with low kinetic energy was investigated. This structure is centered around the foil's normal direction, and its opening angle decreases with increasing foil thickness. With the help of simulations, the ring's occurrence was interpreted as a consequence of the plasma expansion process within the TNSA mechanism. It arises due to a lateral charge separation that is a consequence of the proton distribution's shape during expansion into the vacuum. The explanation may

potentially be used in other experiments to separate features of more sophisticated acceleration mechanisms from those of TNSA-accelerated protons.

At the JETI 40 laser system, water microdroplets were irradiated with frequency-doubled laser pulses, while the droplets' expansion was observed with an optical probe laser system filtered to off-harmonic wavelengths. The shape and size of plasma expanding on a picosecond timescale could be correlated with the protons accelerated in the laser forward direction.

The maximum proton energy was low, and the plasma expansion small when the droplets were irradiated centrally. As the droplets were shifted by approximately their radius along the laser's polarization direction, the expanded plasma was larger, and the maximum proton energy was more than twice as high. With the help of 2D-PIC simulations, a population of hot electrons could be identified which was confined close to the surface due to self-generated electric and magnetic fields. These confined electrons enhance the electric field responsible for proton acceleration, which is only possible for targets with a limited volume, such as droplets since in this case the confined current cannot escape the interaction region. The application of a controlled pre-pulse led to higher proton energies for normal laser incidence due to an increased generation of hot electrons. With the pre-pulse applied, the average maximum proton energy remained relatively similar for the different irradiation geometries, together with the expanded plasma's shape. This indicates that the sensitivity of the acceleration process on the irradiation geometry is effectively reduced. However, slightly higher maximum proton energies were achieved on a single shot basis without the pre-pulse and under grazing laser incidence. Since most applications require stable proton sources, further investigations with various pre-plasmas are necessary to find settings that may deliver high maximum proton energies and reduced sensitivity.

Additionally, measurements of the proton beam's profile around the laser's forward direction were performed, and a stable, net-like proton pattern was detected. Due to the dependency of the pattern on the irradiation geometry, it is possible that the laser's electric field modulations imprint on the water vapor and then on the accelerated protons [206]. Further investigations, for example, with different target geometries and controlled background pressure conditions are necessary to manipulate these structures to implement such targets as a reliable proton source in the future, bringing laser-based MeV ion sources and their potential applications closer to reality.

A. Appendix

A.1. The JETI 40 laser system

JETI 40 is a Ti:sapphire laser system whose laser pulses can be focused to relativistic intensities. The system is designed according to the chirped pulse amplification (CPA) scheme [5]. Within this scheme, laser pulses are temporally stretched before amplification, which reduces the laser's intensity, to avoid self-focusing in transmissive optics and thus damaging the amplifiers. After the laser pulses are fully amplified, they can be recompressed to femtosecond duration. A diagram with the main components of the laser is shown in Fig. A.1

The first component of the front-end (Amplitude Technologies) is an oscillator (Femtosource Scientific by Femtolasers). It provides laser pulses at a repetition rate of 75 MHz. In the booster, the repetition rate is reduced to 10 Hz, while the laser pulses are already amplified to 2 μ J. Before further amplification, the pulses are stretched to 800 ps. To pre-compensate high-order spectral phase distortions, which the laser pulses can experience as they pass through the entire laser system, an acousto-optic programmable dispersive filter [209, 210] (Dazzler by Fastlite) is installed before the next amplifier. This ensures that the stretched pulses are optimally compressible after amplification. The last part of the front-end consists of a regenerative amplifier and a 5-pass amplifier.

The pulses coming from this front-end are further amplified first by a 3-pass amplifier and then by a 2-pass amplifier with a cryogenic cooled active medium. The maximum pulse energy after this last amplifier is 1.3 J. In the grating compressor, the stretched pulses are recompressed to a minimum pulse duration of 25 fs. Then, the compressed pulses enter a chamber with an adaptive optic (AO) [211]. With the AO, wavefront aberrations can be corrected to increase the focusability of the laser pulses in the target chamber.

In the experiment with water microdroplets (see Chapter 4), the final amplifier was

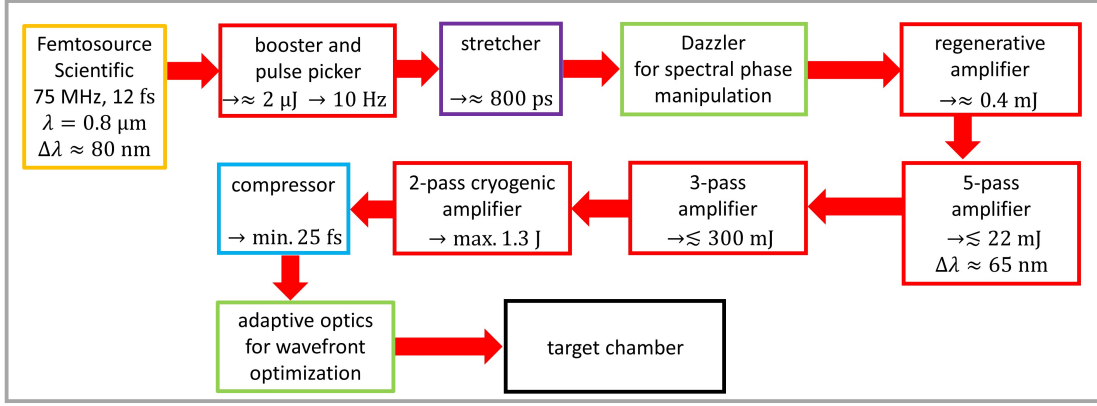


Figure A.1.: Schematic of the JETI 40 laser system. Laser parameters were provided by F. Ronneberger [208].

delivering ≈ 1.2 J. Due to the compressor and beamline transmission efficiency, the laser pulses entering the target chamber had a pulse energy of $E_L \approx 750$ mJ. The pulse duration was $\tau_L \approx 35$ fs and thus longer than the minimum duration of 25 fs mainly due to two reasons. Firstly, the width of the laser spectrum was reduced to approximately 50 nm (FWHM) to increase the efficiency of the SHG process used in the droplet experiment. However, a narrower spectrum leads also to a longer pulse duration of the fundamental. Secondly, the duration of the probe laser (see next section) was optimized using the Dazzler. Since the main laser and the probe laser rely on the same Dazzler, this can also result in a longer duration of the main laser pulses.

A.1.1. The optical probe laser

To monitor the interaction of the main laser pulses in an experiment with water droplets (see Chapter 4), a few-cycle optical probe laser was used [59]. A sketch of the probe's setup is shown in Fig. 1 in [59]. The probe works in principle as follows. Using a beam splitter (BS) within the vacuum beamline, $\approx 1\%$ of the main laser pulse energy is extracted after the main compressor. These pulses leave the vacuum chamber and are further reduced in diameter to about 1 cm containing $\lesssim 1$ mJ. Since these pulses have been chirped during their passage through the beam splitter and a window, two chirped mirrors (CM) are installed in the beam path to recompress the pulses. These pulses are then focused into a hollow-core fiber filled with neon gas. Due to self-phase-modulation in the gas, the laser pulses are

spectrally broadened to a bandwidth of $\Delta\lambda \approx 400$ nm. An example of a spectrum can be seen in Fig. 1 in [60]. Eight CMs are placed in the beam path to compress these laser pulses to a duration of a few femtoseconds. For fine compensation of negative group delay dispersion induced by these CMs, fused silica wedges can be inserted into the beam path. The mean duration of the compressed pulses was measured to be < 4 fs, whereas the Fourier-transform-limit was ≈ 2.8 fs [60]. These short pulses could be used to image laser-driven wakefields in an electron acceleration experiment [61]. For their use in an ion acceleration experiment, the probe pulse's duration must not be that short since ion acceleration takes place on timescales of or longer than the main laser pulse's duration. However, it is beneficial to use an optical probe with a broadband spectrum containing spectral intensity away from the main laser's spectrum. Laser light scattered by the plasma, laser harmonics generated by the laser-plasma interaction, or plasma emission would typically produce a strong, saturating signal on the imaging detector. By spectrally filtering the probe after the interaction in a spectral region away from the scattered or generated light, this unwanted signal can be significantly reduced, and images of the laser-plasma interaction can be recorded as shown in Chapter 4.

A.2. The POLARIS laser system

POLARIS stands for Petawatt Optical Laser Amplifier for Radiation Intensive experimentS. It is a diode-pumped, solid-state laser system, based on the double CPA principle [212] and is operated by the Helmholtz-Institute Jena and the Institute of Optics and Quantum Electronics [50, 213]. A diagram showing the main components of the laser is presented in Fig. A.2.

The seed pulses at $\lambda = 1.03$ μm for the laser system are delivered by a Ti:sapphire oscillator (Mira 900 by Coherent). For further amplification, a Pockels cell pulse picker lets one pulse per second pass to the first CPA. Details can be found in [214, 215]. First, these pulses are stretched to a duration of 20 ps. This allows the amplification up to a pulse energy of 2 mJ in the first regenerative amplifier A1. As the active medium Yb^{3+} :glass is used, as in the following amplifiers A2, A3, and A4. The pulses are recompressed to a pulse duration of ≈ 117 fs in the first of the two compressors equipped with gold gratings. The TIC of these pulses is improved by the generation of a cross-polarized wave (XPW) [214]. The ratio of the amplified spontaneous emission (ASE) to the laser's peak intensity of the generated pulses is

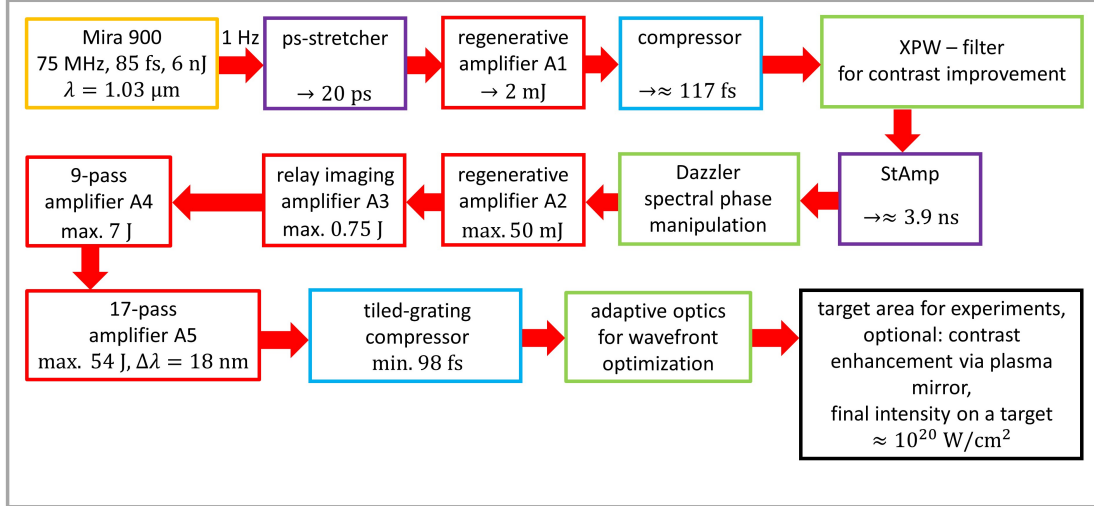


Figure A.2.: Schematic of the POLARIS laser system.

improved by the XPW stage to $\approx 2 \cdot 10^{-13}$. These pulses are sent to an amplifier with an intracavity stretcher (StAmp) [216]. The pulses are stretched to $\approx 3.9 \text{ ns}$ and can be amplified to hundreds of μJ . Like in the JETI laser system, a Dazzler (Fastlite) is used to pre-compensate high-order phase aberrations [209, 210].

Afterwards, the laser pulses enter the next regenerative amplifier A2, where they are amplified up to a maximum of 50 mJ [215, 216]. For further amplification, these pulses pass three multi-pass amplifiers. A3 is a 20-pass relay-imaging amplifier, whose design is described in [217]. Here, the pulse energy is increased to 750 mJ. In the 9-pass amplifier A4, the pulses are further amplified to a maximum energy of 7 J. In the final amplifier A5 [50, 218], the laser pulses pass the active medium, Yb:CaF₂, 17 times. It has been demonstrated that this amplifier, which runs with a repetition rate of 1/50 Hz, can deliver pulses with an energy of 54 J.

However, due to the damage-threshold of the gold gratings ($\approx 0.2 \text{ J/cm}^2$) installed in the tiled-grating compressor [213, 219], it is currently not possible to compress pulses with such a high energy. The highest energy sent through the compressor during the time of the experiments presented in this thesis was $\approx 26.6 \text{ J}$, while the shortest pulses leaving the compressor had a duration of $\approx 98 \text{ fs}$. Before they are sent to the target chamber, the laser pulses are reflected by an AO. The transmission efficiency of the compressor and the beamline was measured in the target chamber to be $\gtrsim 60 \%$.

A.3. Estimation of the proton number detected with the TP in the water droplet experiment

As written in Sec. 3.1.1, a MCP with a phosphor screen imaged onto a CCD camera was used in the TP to measure the spectra of the accelerated protons. However, the camera does provide a bit-count per pixel that depends on the detector and camera settings. To obtain an estimate of the actual detected number of protons as a function of the proton energy E_{kin} , CR-39 nuclear track detectors can be used that provide an absolute number of protons. For this purpose, CR-39 plates with a grating structure can be placed in front of the MCP, as was done in [155, 156]. The CR-39s used here have slits with a width of 3 mm and a grating constant of 6 mm. Consequently, parts of a spectrum are detected by a CR-39 and the parts that are not blocked are detected by the MCP. This allows a direct comparison of the camera signal with the absolute proton number. Thus, a “conversion” factor/function between the MCP/camera signal and the number of protons can be obtained. The conversion factor as a function of E_{kin} obtained with two different CR-39 detectors/shots in the experiment with water microdroplets is shown in Fig. A.3. The fit is $f = (2.4 \cdot 10^{-2} \cdot \exp(-E_{\text{kin}}/0.184 \text{ MeV}) + 3.25 \cdot 10^{-4})$ protons/counts. The conversion factor (protons/counts) decreases with increasing E_{kin} , or in other words, the response of the MCP (counts/protons) increases with increasing proton energy. A comparable behavior was measured by Prasad *et al.* [155] for proton energies between 1 MeV and 3 MeV, where the measured detector’s response (counts/proton) increased with increasing proton energy by a factor of 2. Jeong *et al.* [156] obtained a roughly constant detector response for kinetic energies between 2 MeV and 8 MeV, which decreases for higher energies.

However, a variation of the conversion factor (protons/counts) between 3 and 10 was measured in [220] when using protons from a conventional accelerator with kinetic energies between 1 MeV and 4 MeV, where a higher conversion factor was measured for higher energies (which corresponds to a reduced detector response). For three comparison measurements with CR-39 detectors at the JETI 40 laser system, different exponential conversion functions were obtained [220, 221]. There, consecutive measurements performed either with CR-39 detectors or the MCP were compared. A comparable behavior was measured by Harres *et al.* [148]. They used radiochromic films for comparison with their MCP and measured a quadratic increase of the conversion factor (protons/counts) as a function of the proton energy

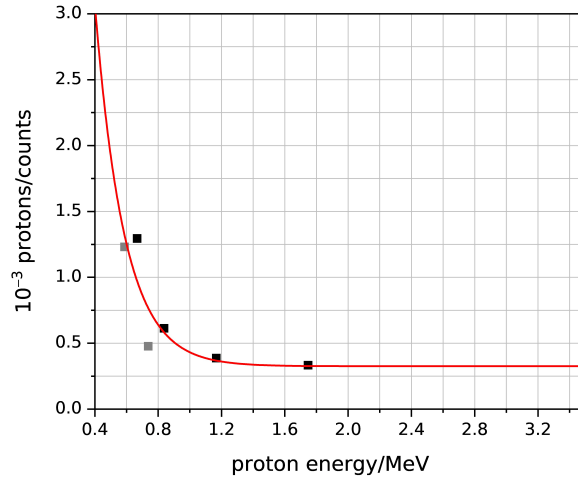


Figure A.3.: The squares are experimentally determined “conversion factors” between MCP/camera counts and protons detected with CR-39 for two different shots (black and grey) taken in the droplet experiment. The red line is a fit. More details are in the text.

for values between 2 MeV and 12 MeV.

To obtain the number of protons/ $(50 \text{ keV} \cdot 0.8 \text{ } \mu\text{sr})$ as a function of the proton energy, as shown Figs. 4.4 and 4.6, the spectra obtained with the MCP given in bit counts/ $(50 \text{ keV} \cdot 0.8 \text{ } \mu\text{sr})$ were multiplied by f . Besides the variation of the conversion factor with E_{kin} , it cannot be excluded that other factors influence the conversion factor since there is apparently a difference between the two CR-39 measurements shown in Fig. A.3.

References

- [1] S. P. Hatchett, C. G. Brown, T. E. Cowan, E. A. Henry, J. S. Johnson, M. H. Key, J. A. Koch, A. B. Langdon, B. F. Lasinski, R. W. Lee, A. J. Mackinnon, D. M. Pennington, M. D. Perry, T. W. Phillips, M. Roth, T. C. Sangster, M. S. Singh, R. A. Snavely, M. A. Stoyer, S. C. Wilks, and K. Yasuike. Electron, photon, and ion beams from the relativistic interaction of petawatt laser pulses with solid targets. *Physics of Plasmas*, 7(5):2076–2082, 2000.
- [2] R. A. Snavely, M. H. Key, S. P. Hatchett, T. E. Cowan, M. Roth, T. W. Phillips, M. A. Stoyer, E. A. Henry, T. C. Sangster, M. S. Singh, S. C. Wilks, A. MacKinnon, A. Offenberger, D. M. Pennington, K. Yasuike, A. B. Langdon, B. F. Lasinski, J. Johnson, M. D. Perry, and E. M. Campbell. Intense high-energy proton beams from petawatt-laser irradiation of solids. *Physical Review Letters*, 85(14):2945–2948, 2000.
- [3] E. L. Clark, K. Krushelnick, J. R. Davies, M. Zepf, M. Tatarakis, F. N. Beg, A. Machacek, P. A. Norreys, M. I. K. Santala, I. Watts, and A. E. Dangor. Measurements of energetic proton transport through magnetized plasma from intense laser interactions with solids. *Physical Review Letters*, 84(4):670–673, 2000.
- [4] E. L. Clark, K. Krushelnick, M. Zepf, F. N. Beg, M. Tatarakis, A. Machacek, M. I. K. Santala, I. Watts, P. A. Norreys, and A. E. Dangor. Energetic heavy-ion and proton generation from ultraintense laser-plasma interactions with solids. *Physical Review Letters*, 85(8):1654–1657, 2000.
- [5] D. Strickland and G. Mourou. Compression of amplified chirped optical pulses. *Optics Communications*, 55(6):447–449, 1985.
- [6] J. W. Yoon, C. Jeon, J. Shin, S. K. Lee, H. W. Lee, I. W. Choi, H. T. Kim, J. H. Sung, and C. H. Nam. Achieving the laser intensity of 5.5×10^{22} W/cm² with a wavefront-corrected multi-PW laser. *Optics Express*, 27(15):20412–20420, 2019.
- [7] C. N. Danson, C. Haefner, J. Bromage, T. Butcher, J.-C. F. Chanteloup, E. A. Chowdhury, A. Galvanauskas, L. A. Gizzi, J. Hein, D. I. Hillier, N. W. Hopps, Y. Kato, E. A. Khazanov, R. Kodama, G. Korn, R. Li, Y. Li, J. Limpert, J. Ma, C. H. Nam, D. Neely, D. Papadopoulos, R. R. Penman, L. Qian, J. J. Rocca, A. A. Shaykin, C. W. Siders, C. Spindloe, S. Szatmári, R. M. G. M. Trines, J. Zhu, P. Zhu, and J. D. Zuegel. Petawatt and exawatt class lasers worldwide. *High Power Laser Science and Engineering*, 7:e54, 2019.
- [8] S. C. Wilks, A. B. Langdon, T. E. Cowan, M. Roth, M. Singh, S. Hatchett,

- M. H. Key, D. Pennington, A. MacKinnon, and R. A. Snavely. Energetic proton generation in ultra-intense laser-solid interactions. *Physics of Plasmas*, 8(2):542–549, 2001.
- [9] J. Hornung, Y. Zobus, P. Boller, C. Brabetz, U. Eisenbarth, T. Kühl, Z. Major, J. B. Ohland, M. Zepf, B. Zielbauer, and V. Bagnoud. Enhancement of the laser-driven proton source at PHELIX. *High Power Laser Science and Engineering*, 8:e24, 2020.
- [10] B. Dromey, M. Coughlan, L. Senje, M. Taylor, S. Kuschel, B. Villagomez-Bernabe, R. Stefanuik, G. Nersisyan, L. Stella, J. Kohanoff, M. Borghesi, F. Currell, D. Riley, D. Jung, C.-G. Wahlström, C. L. S. Lewis, and M. Zepf. Picosecond metrology of laser-driven proton bursts. *Nature Communications*, 7:10642, 2016.
- [11] T. E. Cowan, J. Fuchs, H. Ruhl, A. Kemp, P. Audebert, M. Roth, R. Stephens, I. Barton, A. Blažević, E. Brambrink, J. Cobble, J. Fernández, J.-C. Gauthier, M. Geissel, M. Hegelich, J. Kaae, S. Karsch, G. P. Le Sage, S. Letzring, M. Manclossi, S. Meyroneinc, A. Newkirk, H. Pépin, and N. Renard-LeGalloudec. Ultralow emittance, multi-MeV proton beams from a laser virtual-cathode plasma accelerator. *Physical Review Letters*, 92(20):204801, 2004.
- [12] F. Nürnberg, M. Schollmeier, E. Brambrink, A. Blažević, D. C. Carroll, K. Flippo, D. C. Gautier, M. Geißel, K. Harres, B. M. Hegelich, O. Lundh, K. Markey, P. McKenna, D. Neely, J. Schreiber, and M. Roth. Radiochromic film imaging spectroscopy of laser-accelerated proton beams. *Review of Scientific Instruments*, 80(3):033301, 2009.
- [13] A. Macchi, M. Borghesi, and M. Passoni. Ion acceleration by superintense laser-plasma interaction. *Reviews of Modern Physics*, 85(2):751–793, 2013.
- [14] H. Daido, M. Nishiuchi, and A. S. Pirozhkov. Review of laser-driven ion sources and their applications. *Reports on Progress in Physics*, 75(5):056401, 2012.
- [15] F. Hinterberger. *Physik der Teilchenbeschleuniger und Ionenoptik*. Springer, 2008.
- [16] M. Barberio, M. Scisciò, S. Vallières, F. Cardelli, S. N. Chen, G. Famulari, T. Gangolf, G. Revet, A. Schiavi, M. Senzacqua, and P. Antici. Laser-accelerated particle beams for stress testing of materials. *Nature Communications*, 9:372, 2018.
- [17] M. Barberio, S. Veltri, M. Scisciò, and P. Antici. Laser-accelerated proton beams as diagnostics for cultural heritage. *Scientific Reports*, 7:40415, 2017.
- [18] M. Barberio, M. Scisciò, S. Vallières, S. Veltri, A. Morabito, and P. Antici. Laser-generated proton beams for high-precision ultra-fast crystal synthesis. *Scientific Reports*, 7:12522, 2017.
- [19] T. M. Ostermayr, C. Kreuzer, F. S. Englbrecht, J. Gebhard, J. Hartmann, A. Huebl, D. Haffa, P. Hilz, K. Parodi, J. Wenz, M. E. Donovan, G. Dyer,

- E. Gaul, J. Gordon, M. Martinez, E. Mccary, M. Spinks, G. Tiwari, B. M. Hegelich, and J. Schreiber. Laser-driven x-ray and proton micro-source and application to simultaneous single-shot bi-modal radiographic imaging. *Nature Communications*, 11:6174, 2020.
- [20] A. J. Mackinnon, P. K. Patel, R. P. Town, M. J. Edwards, T. Phillips, S. C. Lerner, D. W. Price, D. Hicks, M. H. Key, S. Hatchett, S. C. Wilks, M. Borghesi, L. Romagnani, S. Kar, T. Toncian, G. Pretzler, O. Willi, M. Koenig, E. Martinoli, S. Lepape, A. Benuzzi-Mounaix, P. Audebert, J. C. Gauthier, J. King, R. Snavely, R. R. Freeman, and T. Boehlly. Proton radiography as an electromagnetic field and density perturbation diagnostic (invited). *Review of Scientific Instruments*, 75(10):3531–3536, 2004.
- [21] L. Romagnani, A. P. L. Robinson, R. J. Clarke, D. Doria, L. Lancia, W. Nazarov, M. M. Notley, A. Pipahl, K. Quinn, B. Ramakrishna, P. A. Wilson, J. Fuchs, O. Willi, and M. Borghesi. Dynamics of the electromagnetic fields induced by fast electron propagation in near-solid-density media. *Physical Review Letters*, 122(2):025001, 2019.
- [22] K. L. Lancaster, S. Karsch, H. Habara, F. N. Beg, E. L. Clark, R. Freeman, M. H. Key, J. A. King, R. Kodama, K. Krushelnick, K. W. D. Ledingham, P. McKenna, C. D. Murphy, P. A. Norreys, R. Stephens, C. Stöeckl, Y. Toyama, M. S. Wei, and M. Zepf. Characterization of ${}^7\text{Li}(p, n){}^7\text{Be}$ neutron yields from laser produced ion beams for fast neutron radiography. *Physics of Plasmas*, 11(7):3404–3408, 2004.
- [23] S. Kar, A. Green, H. Ahmed, A. Alejo, A. P. L. Robinson, M. Cerchez, R. Clarke, D. Doria, S. Dorkings, J. Fernandez, S. R. Mirfayzi, P. McKenna, K. Naughton, D. Neely, P. Norreys, C. Peth, H. Powell, J. A. Ruiz, J. Swain, O. Willi, and M. Borghes. Beamed neutron emission driven by laser accelerated light ions. *New Journal of Physics*, 18(5):053002, 2016.
- [24] P. K. Patel, A. J. Mackinnon, M. H. Key, T. E. Cowan, M. E. Foord, M. Allen, D. F. Price, H. Ruhl, P. T. Springer, and R. Stephens. Isochoric heating of solid-density matter with an ultrafast proton beam. *Physical Review Letters*, 91(12):125004, 2003.
- [25] A. McKelvey, G. E. Kemp, P. A. Sterne, A. Fernandez-Panella, R. Shepherd, M. Marinak, A. Link, G. W. Collins, H. Sio, J. King, R. R. Freeman, R. Hua, C. McGuffey, J. Kim, F. N. Beg, and Y. Ping. Thermal conductivity measurements of proton-heated warm dense aluminum. *Scientific Reports*, 7:7015, 2017.
- [26] M. Roth, T. E. Cowan, M. H. Key, S. P. Hatchett, C. Brown, W. Fountain, J. Johnson, D. M. Pennington, R. A. Snavely, S. C. Wilks, K. Yasuike, H. Ruhl, F. Pegoraro, S. V. Bulanov, E. M. Campbell, M. D. Perry, and H. Powell. Fast ignition by intense laser-accelerated proton beams. *Physical Review Letters*, 86(3):436–439, 2001.
- [27] J. C. Fernández, B. J. Albright, F. N. Beg, M. E. Foord, B. M. Hegelich, J. J.

- Honrubia, M. Roth, R. B. Stephens, and L. Yin. Fast ignition with laser-driven proton and ion beams. *Nuclear Fusion*, 54(5):054006, 2014.
- [28] S. V. Bulanov and V. S. Khoroshkov. Feasibility of using laser ion accelerators in proton therapy. *Plasma Physics Reports*, 28(5):453–456, 2002.
- [29] V. Malka, S. Fritzler, E. Lefebvre, E. d’Humières, R. Ferrand, G. Grillon, C. Albaret, S. Meyroneinc, J.-P. Chambaret, A. Antonetti, and D. Hulin. Practicability of protontherapy using compact laser systems. *Medical Physics*, 31(6):1587–1592, 2004.
- [30] A. Yogo, K. Sato, M. Nishikino, M. Mori, T. Teshima, H. Numasaki, M. Murakami, Y. Demizu, S. Akagi, S. Nagayama, K. Ogura, A. Sagisaka, S. Orimo, M. Nishiuchi, A. S. Pirozhkov, M. Ikegami, M. Tampo, H. Sakaki, M. Suzuki, I. Daito, Y. Oishi, H. Sugiyama, H. Kiriya, H. Okada, S. Kanazawa, S. Kondo, T. Shimomura, Y. Nakai, M. Tanoue, H. Sasao, D. Wakai, P. R. Bolton, and H. Daido. Application of laser-accelerated protons to the demonstration of DNA double-strand breaks in human cancer cells. *Applied Physics Letters*, 94(18):181502, 2009.
- [31] F. Hanton, P. Chaudhary, D. Doria, D. Gwynne, C. Maiorino, C. Scullion, H. Ahmed, T. Marshall, K. Naughton, L. Romagnani, S. Kar, G. Schettino, P. McKenna, S. Botchway, D. R. Symes, P. P. Rajeev, K. M. Prise, and M. Borghesi. DNA DSB repair dynamics following irradiation with laser-driven protons at ultra-high dose rates. *Scientific Reports*, 9:4471, 2019.
- [32] S. Raschke, S. Spickermann, T. Toncian, M. Swantusch, J. Boeker, U. Giesen, G. Iliakis, O. Willi, and F. Boege. Ultra-short laser-accelerated proton pulses have similar DNA-damaging effectiveness but produce less immediate nitroxidative stress than conventional proton beams. *Scientific Reports*, 6:32441, 2016.
- [33] K. Ledingham, P. Bolton, N. Shikazono, and C.-M. Ma. Towards laser driven hadron cancer radiotherapy: A review of progress. *Applied Sciences*, 4(3):402–443, 2014.
- [34] K. M. Hofmann, U. Masood, J. Pawelke, and J. J. Wilkens. A treatment planning study to assess the feasibility of laser-driven proton therapy using a compact gantry design. *Medical Physics*, 42(9):5120–5129, 2015.
- [35] L. Karsch, E. Beyreuther, W. Enghardt, M. Gotz, U. Masood, U. Schramm, K. Zeil, and J. Pawelke. Towards ion beam therapy based on laser plasma accelerators. *Acta Oncologica*, 56(11):1359–1366, 2017.
- [36] U. Masood, T. E. Cowan, W. Enghardt, K. M. Hofmann, L. Karsch, F. Kroll, U. Schramm, J. J. Wilkens, and J. Pawelke. A light-weight compact proton gantry design with a novel dose delivery system for broad-energetic laser-accelerated beams. *Physics in Medicine & Biology*, 62(13):5531, 2017.
- [37] D. Margarone, G. A. P. Cirrone, G. Cuttone, A. Amico, L. Andó, M. Borghesi, S. S. Bulanov, S. V. Bulanov, D. Chatain, A. Fajstavr, L. Giuffrida, F. Grepl, S. Kar, J. Krasa, D. Kramer, G. Larosa, R. Leanza, T. Levato, M. Mag-

- giore, L. Manti, G. Milluzzo, B. Odlozilik, V. Olsovcova, J.-P. Perin, J. Pipek, J. Psikal, G. Petringa, J. Ridky, F. Romano, B. Rus, A. Russo, F. Schillaci, V. Scuderi, A. Velyhan, R. Versaci, T. Wiste, M. Zakova, and G. Korn. ELI-MaIA: A laser-driven ion accelerator for multidisciplinary applications. *Quantum Beam Science*, 2(2):8, 2018.
- [38] S. Busold, A. Almomani, V. Bagnoud, W. Barth, S. Bedacht, A. Blažević, O. Boine-Frankenheim, C. Brabetz, T. Burris-Mog, T. Cowan, O. Deppert, M. Droba, H. Eickhoff, U. Eisenbarth, K. Harres, G. Hoffmeister, I. Hofmann, O. Jaeckel, R. Jaeger, M. Joost, S. Kraft, F. Kroll, M. Kaluza, O. Kester, Z. Lecz, T. Merz, F. Nuernberg, H. Al-Omari, A. Orzhekhovskaya, G. Paulus, J. Polz, U. Ratzinger, M. Roth, G. Schaumann, P. Schmidt, U. Schramm, G. Schreiber, D. Schumacher, T. Stoehlker, A. Tauschwitz, W. Vinzenz, F. Wagner, S. Yaramyshev, and B. Zielbauer. Shaping laser accelerated ions for future applications—the LIGHT collaboration. *Nuclear Instruments and Methods in Physics Research Section A: Accelerators, Spectrometers, Detectors and Associated Equipment*, 740:94–98, 2014.
- [39] S. Busold, D. Schumacher, C. Brabetz, D. Jahn, F. Kroll, O. Deppert, U. Schramm, T. E. Cowan, A. Blažević, V. Bagnoud, and M. Roth. Towards highest peak intensities for ultra-short MeV-range ion bunches. *Scientific Reports*, 5:12459, 2015.
- [40] D. Jahn, D. Schumacher, C. Brabetz, F. Kroll, F. E. Brack, J. Ding, R. Leonhardt, I. Semmler, A. Blažević, U. Schramm, and M. Roth. Focusing of multi-MeV, subnanosecond proton bunches from a laser-driven source. *Physical Review Accelerators and Beams*, 22(1):011301, 2019.
- [41] F.-E. Brack, F. Kroll, L. Gaus, C. Bernert, E. Beyreuther, T. E. Cowan, L. Karsch, S. Kraft, L. A. Kunz-Schughart, E. Lessmann, J. Metzkes-Ng, L. Obst-Huebl, J. Pawelke, M. Rehwald, H.-P. Schlenvoigt, U. Schramm, M. Sobiella, E. R. Szabó, T. Ziegler, and K. Zeil. Spectral and spatial shaping of laser-driven proton beams using a pulsed high-field magnet beamline. *Scientific Reports*, 10:9118, 2020.
- [42] A. Higginson, R. J. Gray, M. King, R. J. Dance, S. D. R. Williamson, N. M. H. Butler, R. Wilson, R. Capdessus, C. Armstrong, J. S. Green, S. J. Hawkes, P. Martin, W. Q. Wei, S. R. Mirfayzi, X. H. Yuan, S. Kar, M. Borghesi, R. J. Clarke, D. Neely, and P. McKenna. Near-100 MeV protons via a laser-driven transparency-enhanced hybrid acceleration scheme. *Nature Communications*, 9:724, 2018.
- [43] T. Esirkepov, M. Borghesi, S. V. Bulanov, G. Mourou, and T. Tajima. Highly efficient relativistic-ion generation in the laser-piston regime. *Physical Review Letters*, 92(17):175003, 2004.
- [44] A. Macchi, S. Veghini, and F. Pegoraro. “Light sail” acceleration reexamined. *Physical Review Letters*, 103(8):085003, 2009.
- [45] A. Henig, S. Steinke, M. Schnürer, T. Sokollik, R. Hörlein, D. Kiefer, D. Jung,

- J. Schreiber, B. M. Hegelich, X. Q. Yan, J. Meyer-ter Vehn, T. Tajima, P. V. Nickles, W. Sandner, and D. Habs. Radiation-pressure acceleration of ion beams driven by circularly polarized laser pulses. *Physical Review Letters*, 103(24):245003, 2009.
- [46] I. J. Kim, K. H. Pae, C. M. Kim, H. T. Kim, J. H. Sung, S. K. Lee, T. J. Yu, I. W. Choi, C.-L. Lee, K. H. Nam, P. V. Nickles, T. M. Jeong, and J. Lee. Transition of proton energy scaling using an ultrathin target irradiated by linearly polarized femtosecond laser pulses. *Physical Review Letters*, 111(16):165003, 2013.
- [47] I. J. Kim, K. H. Pae, I. W. Choi, C.-L. Lee, H. T. Kim, H. Singhal, J. H. Sung, S. K. Lee, H. W. Lee, P. V. Nickles, T. M. Jeong, C. M. Kim, and C. H. Nam. Radiation pressure acceleration of protons to 93 MeV with circularly polarized petawatt laser pulses. *Physics of Plasmas*, 23(7):070701, 2016.
- [48] C. Scullion, D. Doria, L. Romagnani, A. Sgattoni, K. Naughton, D. R. Symes, P. McKenna, A. Macchi, M. Zepf, S. Kar, and M. Borghesi. Polarization dependence of bulk ion acceleration from ultrathin foils irradiated by high-intensity ultrashort laser pulses. *Physical Review Letters*, 119(5):054801, 2017.
- [49] M. Hornung, H. Liebetrau, A. Seidel, S. Keppler, A. Kessler, J. Körner, M. Hellwing, F. Schorcht, D. Klöpfel, A. K. Arunachalam, G. A. Becker, A. Sävert, J. Polz, J. Hein, and M. C. Kaluza. The all-diode-pumped laser system POLARIS – an experimentalist’s tool generating ultra-high contrast pulses with high energy. *High Power Laser Science and Engineering*, 2, 2014.
- [50] M. Hornung, H. Liebetrau, S. Keppler, A. Kessler, M. Hellwing, F. Schorcht, G. A. Becker, M. Reuter, J. Polz, J. Körner, J. Hein, and M. C. Kaluza. 54 J pulses with 18 nm bandwidth from a diode-pumped chirped-pulse amplification laser system. *Optics Letters*, 41(22):5413, 2016.
- [51] C. N. Danson, P. A. Brummitt, R. J. Clarke, J. L. Collier, B. Fell, A. J. Frackiewicz, S. Hancock, S. Hawkes, C. Hernandez-Gomez, P. Holligan, M. H. R. Hutchinson, A. Kidd, W. J. Lester, I. O. Musgrave, D. Neely, D. R. Neville, P. A. Norreys, D. A. Pepler, C. J. Reason, W. Shaikh, T. B. Winstone, R. W. W. Wyatt, and B. E. Wyborn. Vulcan Petawatt—an ultra-high-intensity interaction facility. *Nuclear Fusion*, 44(12):S239–S246, 2004.
- [52] V. Bagnoud, B. Aurand, A. Blazevic, S. Borneis, C. Bruske, B. Ecker, U. Eisenbarth, J. Fils, A. Frank, E. Gaul, S. Goette, C. Haefner, T. Hahn, K. Harres, H.-M. Heuck, D. Hochhaus, D. H. H. Hoffmann, D. Javorková, H.-J. Kluge, T. Kuehl, S. Kunzer, M. Kreutz, T. Merz-Mantwill, P. Neumayer, E. Onkels, D. Reemts, O. Rosmej, M. Roth, T. Stoehlker, A. Tauschwitz, B. Zielbauer, D. Zimmer, and K. Witte. Commissioning and early experiments of the PHELIX facility. *Applied Physics B*, 100(1):137–150, 2010.
- [53] P. L. Poole, L. Obst, G. E. Cochran, J. Metzkes, H.-P. Schlenvoigt, I. Prencipe, T. Kluge, T. Cowan, U. Schramm, D. W. Schumacher, and K. Zeil. Laser-

- driven ion acceleration via target normal sheath acceleration in the relativistic transparency regime. *New Journal of Physics*, 20(1):013019, 2018.
- [54] I. Tamer. *Petawatt-Class Laser Optimization and Ultrashort Probe Pulse Generation for Relativistic Laser-Plasma Interactions*. PhD thesis, Friedrich-Schiller-Universität Jena, 2020.
- [55] G. A. Becker, S. Tietze, S. Keppler, J. Reislöhner, J. H. Bin, L. Bock, F. E. Brack, J. Hein, M. Hellwing, P. Hilz, M. Hornung, A. Kessler, S. Kraft, S. Kuschel, H. Liebetrau, W. Ma, J. Polz, H.-P. Schlenvoigt, F. Schorcht, M. B. Schwab, A. Seidel, K. Zeil, U. Schramm, M. Zepf, J. Schreiber, S. Rykovanov, and M. C. Kaluza. Ring-like spatial distribution of laser accelerated protons in the ultra-high-contrast TNSA-regime. *Plasma Physics and Controlled Fusion*, 60(5):055010, 2018.
- [56] Y. Gao, J. Bin, D. Haffa, C. Kreuzer, J. Hartmann, M. Speicher, F. H. Lindner, T. M. Ostermayr, P. Hilz, T. F. Rösch, S. Lehrack, F. Englbrecht, S. Seuferling, M. Gilljohann, H. Ding, W. Ma, K. Parodi, and J. Schreiber. An automated, 0.5 Hz nano-foil target positioning system for intense laser plasma experiments. *High Power Laser Science and Engineering*, 5:e12, 2017.
- [57] P. McKenna, D. C. Carroll, R. J. Clarke, R. G. Evans, K. W. D. Ledingham, F. Lindau, O. Lundh, T. McCanny, D. Neely, A. P. L. Robinson, L. Robson, P. T. Simpson, C.-G. Wahlström, and M. Zepf. Lateral electron transport in high-intensity laser-irradiated foils diagnosed by ion emission. *Physical Review Letters*, 98(14):145001, 2007.
- [58] G. A. Becker, M. B. Schwab, R. Löttsch, S. Tietze, D. Klöpfel, M. Rehwald, H.-P. Schlenvoigt, A. Sävert, U. Schramm, M. Zepf, and M. C. Kaluza. Characterization of laser-driven proton acceleration from water microdroplets. *Scientific Reports*, 9:17169, 2019.
- [59] M. B. Schwab, A. Sävert, O. Jäckel, J. Polz, M. Schnell, T. Rinck, L. Veisz, M. Möller, P. Hansinger, G. G. Paulus, and M. C. Kaluza. Few-cycle optical probe-pulse for investigation of relativistic laser-plasma interactions. *Applied Physics Letters*, 103(19):191118, 2013.
- [60] D. Adolph, M. Möller, J. Bierbach, M. Schwab, A. Sävert, M. Yeung, A. M. Saylor, M. Zepf, M. C. Kaluza, and G. G. Paulus. Real-time, single-shot, carrier-envelope-phase measurement of a multi-terawatt laser. *Applied Physics Letters*, 110(8):081105, 2017.
- [61] A. Sävert, S. P. D. Mangles, M. Schnell, E. Siminos, J. M. Cole, M. Leier, M. Reuter, M. B. Schwab, M. Möller, K. Poder, O. Jäckel, G. G. Paulus, C. Spielmann, S. Skupin, Z. Najmudin, and M. C. Kaluza. Direct observation of the injection dynamics of a laser wakefield accelerator using few-femtosecond shadowgraphy. *Physical Review Letters*, 115(5):055002, 2015.
- [62] A. Kramida, Y. Ralchenko, J. Reader, and NIST ASD Team. *NIST Atomic Spectra Database* (ver. 5.8), [Online]. Available:

- <https://physics.nist.gov/asd> [2021, February 23]. National Institute of Standards and Technology, Gaithersburg, MD., 2020.
- [63] P. Gibbon. *Short Pulse Laser Interactions with Matter: An Introduction*. Imperial College Press, 2005.
- [64] E. S. Sarachik and G. T. Schappert. Classical theory of the scattering of intense laser radiation by free electrons. *Physical Review D*, 1(10):2738, 1970.
- [65] J.-H. Yang, R. S. Craxton, and M. G. Haines. Explicit general solutions to relativistic electron dynamics in plane-wave electromagnetic fields and simulations of ponderomotive acceleration. *Plasma Physics and Controlled Fusion*, 53(12):125006, 2011.
- [66] F. F. Chen. *Introduction to plasma physics and controlled fusion*. Plenum Press, 1984.
- [67] B. Quesnel and P. Mora. Theory and simulation of the interaction of ultraintense laser pulses with electrons in vacuum. *Physical Review E*, 58(3):3719, 1998.
- [68] D. Bauer, P. Mulser, and W.-H. Steeb. Relativistic ponderomotive force, uphill acceleration, and transition to chaos. *Physical Review Letters*, 75(25):4622, 1995.
- [69] P. Mulser and D. Bauer. *High Power Laser-Matter Interaction*. Springer, 2010.
- [70] S. C. Wilks, W. L. Kruer, M. Tabak, and A. B. Langdon. Absorption of ultra-intense laser pulses. *Physical Review Letters*, 69(9):1383, 1992.
- [71] G. Malka and J. L. Miquel. Experimental confirmation of ponderomotive-force electrons produced by an ultrarelativistic laser pulse on a solid target. *Physical Review Letters*, 77(1):75–78, 1996.
- [72] P. M. Nilson, J. R. Davies, W. Theobald, P. A. Jaanimagi, C. Mileham, R. K. Jungquist, C. Stoeckl, I. A. Begishev, A. A. Solodov, J. F. Myatt, J. D. Zuegel, T. C. Sangster, R. Betti, and D. D. Meyerhofer. Time-resolved measurements of hot-electron equilibration dynamics in high-intensity laser interactions with thin-foil solid targets. *Physical Review Letters*, 108(8):085002, 2012.
- [73] W. Kruer. *The Physics Of Laser Plasma Interactions*. Westview, 2003.
- [74] O. Jäckel, J. Polz, S. M. Pfotenhauer, H.-P. Schlenvoigt, H. Schwoerer, and M. C. Kaluza. All-optical measurement of the hot electron sheath driving laser ion acceleration from thin foils. *New Journal of Physics*, 12(10):103027, 2010.
- [75] S. Palaniyappan, B. M. Hegelich, H.-C. Wu, D. Jung, D. C. Gautier, L. Yin, B. J. Albright, R. P. Johnson, T. Shimada, S. Letzring, D. T. Offermann, J. Ren, C. Huang, R. Hörlein, B. Dromey, J. C. Fernandez, and R. C. Shah. Dynamics of relativistic transparency and optical shuttering in expanding overdense plasmas. *Nature Physics*, 8(10):763–769, 2012.
- [76] F. F. Chen and J. P. Chang. *Lecture Notes on Principles of Plasma Processing*. Springer, 2003.

- [77] K. G. Estabrook, E. J. Valeo, and W. L. Kruer. Two-dimensional relativistic simulations of resonance absorption. *The Physics of Fluids*, 18(9):1151–1159, 1975.
- [78] J. P. Palastro, J. G. Shaw, R. K. Follett, A. Colaïtis, D. Turnbull, A. V. Maximov, V. N. Goncharov, and D. H. Froula. Resonance absorption of a broadband laser pulse. *Physics of Plasmas*, 25(12):123104, 2018.
- [79] F. Brunel. Not-so-resonant, resonant absorption. *Physical Review Letters*, 59(1):52–55, 1987.
- [80] P. Gibbon and A. R. Bell. Collisionless absorption in sharp-edged plasmas. *Physical Review Letters*, 68(10):1535–1538, 1992.
- [81] W. L. Kruer and K. Estabrook. JxB heating by very intense laser light. *The Physics of Fluids*, 28(1):430–432, 1985.
- [82] M. Passoni and M. Lontano. One-dimensional model of the electrostatic ion acceleration in the ultraintense laser–solid interaction. *Laser and Particle Beams*, 22(2):163–169, 2004.
- [83] M. Passoni, L. Bertagna, and A. Zani. Target normal sheath acceleration: theory, comparison with experiments and future perspectives. *New Journal of Physics*, 12(4):045012, 2010.
- [84] M. Kaluza, J. Schreiber, M. I. K. Santala, G. D. Tsakiris, K. Eidmann, J. Meyer-ter Vehn, and K. J. Witte. Influence of the laser prepulse on proton acceleration in thin-foil experiments. *Physical Review Letters*, 93(4):045003, 2004.
- [85] J. Fuchs, P. Antici, E. d’Humières, E. Lefebvre, M. Borghesi, E. Brambrink, C. A. Cecchetti, M. Kaluza, V. Malka, M. Manclossi, S. Meyroneinc, P. Mora, J. Schreiber, T. Toncian, H. Pépin, and P. Audebert. Laser-driven proton scaling laws and new paths towards energy increase. *Nature Physics*, 2(1):48–54, 2006.
- [86] Y. Oishi, T. Nayuki, T. Fujii, Y. Takizawa, X. Wang, T. Yamazaki, K. Nemoto, T. Kayoiji, T. Sekiya, K. Horioka, Y. Okano, Y. Hironaka, K. G. Nakamura, K. Kondo, and A. A. Andreev. Dependence on laser intensity and pulse duration in proton acceleration by irradiation of ultrashort laser pulses on a Cu foil target. *Physics of Plasmas*, 12(7):073102, 2005.
- [87] F. N. Beg, A. R. Bell, A. E. Dangor, C. N. Danson, A. P. Fews, M. E. Glinsky, B. A. Hammel, P. Lee, P. A. Norreys, and M. Tatarakis. A study of picosecond laser-solid interactions up to 10^{19} Wcm⁻². *Physics of Plasmas*, 4(2):447–457, 1997.
- [88] H. Chen, S. C. Wilks, W. L. Kruer, P. K. Patel, and R. Shepherd. Hot electron energy distributions from ultraintense laser solid interactions. *Physics of Plasmas*, 16(2):020705, 2009.
- [89] T. Tanimoto, H. Habara, R. Kodama, M. Nakatsutsumi, K. A. Tanaka, K. L. Lancaster, J. S. Green, R. H. H. Scott, M. Sherlock, P. A. Norreys, R. G.

- Evans, M. G. Haines, S. Kar, M. Zepf, J. King, T. Ma, M. S. Wei, T. Yabuuchi, F. N. Beg, M. H. Key, P. Nilson, R. B. Stephens, H. Azechi, K. Nagai, T. Norimatsu, K. Takeda, J. Valente, and J. R. Davies. Measurements of fast electron scaling generated by petawatt laser systems. *Physics of Plasmas*, 16(6):062703, 2009.
- [90] A. J. Kemp, Y. Sentoku, and M. Tabak. Hot-electron energy coupling in ultraintense laser-matter interaction. *Physical Review Letters*, 101(7):075004, 2008.
- [91] M. G. Haines, M. S. Wei, F. N. Beg, and R. B. Stephens. Hot-electron temperature and laser-light absorption in fast ignition. *Physical Review Letters*, 102(4):045008, 2009.
- [92] T. Kluge, T. Cowan, A. Debus, U. Schramm, K. Zeil, and M. Bussmann. Electron temperature scaling in laser interaction with solids. *Physical Review Letters*, 107(20):205003, 2011.
- [93] Y. Ping, R. Shepherd, B. F. Lasinski, M. Tabak, H. Chen, H. K. Chung, K. B. Fournier, S. B. Hansen, A. Kemp, D. A. Liedahl, K. Widmann, S. C. Wilks, W. Rozmus, and M. Sherlock. Absorption of short laser pulses on solid targets in the ultrarelativistic regime. *Physical Review Letters*, 100(8):085004, 2008.
- [94] R. J. Gray, R. Wilson, M. King, S. D. R. Williamson, R. J. Dance, C. Armstrong, C. Brabetz, F. Wagner, B. Zielbauer, V. Bagnoud, D. Neely, and P. McKenna. Enhanced laser-energy coupling to dense plasmas driven by recirculating electron currents. *New Journal of Physics*, 20(3):033021, 2018.
- [95] W. I. Linlor. Ion energies produced by laser giant pulse. *Applied Physics Letters*, 3(11):210–211, 1963.
- [96] S. J. Gitomer, R. D. Jones, F. Begay, A. W. Ehler, J. F. Kephart, and R. Kristal. Fast ions and hot electrons in the laser-plasma interaction. *The Physics of Fluids*, 29(8):2679–2688, 1986.
- [97] M. Allen, P. K. Patel, A. Mackinnon, D. Price, S. Wilks, and E. Morse. Direct experimental evidence of back-surface ion acceleration from laser-irradiated gold foils. *Physical Review Letters*, 93(26):265004, 2004.
- [98] T. Ceccotti, A. Lévy, H. Popescu, F. Réau, P. D’Oliveira, P. Monot, J. P. Geindre, E. Lefebvre, and Ph. Martin. Proton acceleration with high-intensity ultrahigh-contrast laser pulses. *Physical Review Letters*, 99(18):185002, 2007.
- [99] S. Fourmaux, S. Buffechoux, B. Albertazzi, D. Capelli, A. Lévy, S. Gnedyuk, L. Lecherbourg, P. Lassonde, S. Payeur, P. Antici, H. Pépin, R. S. Marjoribanks, J. Fuchs, and J. C. Kieffer. Investigation of laser-driven proton acceleration using ultra-short, ultra-intense laser pulses. *Physics of Plasmas*, 20(1):013110, 2013.
- [100] A. R. Bell, J. R. Davies, S. Guerin, and H. Ruhl. Fast-electron transport in high-intensity short-pulse laser - solid experiments. *Plasma Physics and Controlled Fusion*, 39(5):653–659, 1997.

- [101] J. R. Davies. The Alfvén limit revisited and its relevance to laser-plasma interactions. *Laser and Particle Beams*, 24(2):299–310, 2006.
- [102] J. S. Green, V. M. Ovchinnikov, R. G. Evans, K. U. Akli, H. Azechi, F. N. Beg, C. Bellei, R. R. Freeman, H. Habara, R. Heathcote, M. H. Key, J. A. King, K. L. Lancaster, N. C. Lopes, T. Ma, A. J. MacKinnon, K. Markey, A. McPhee, Z. Najmudin, P. Nilson, R. Onofrei, R. Stephens, K. Takeda, K. A. Tanaka, W. Theobald, T. Tanimoto, J. Waugh, L. Van Woerkom, N. C. Woolsey, M. Zepf, J. R. Davies, and P. A. Norreys. Effect of laser intensity on fast-electron-beam divergence in solid-density plasmas. *Physical Review Letters*, 100(1):015003, 2008.
- [103] V. M. Ovchinnikov, D. W. Schumacher, M. McMahon, E. A. Chowdhury, C. D. Chen, A. Morace, and R. R. Freeman. Effects of preplasma scale length and laser intensity on the divergence of laser-generated hot electrons. *Physical Review Letters*, 110(6):065007, 2013.
- [104] A. J. Mackinnon, Y. Sentoku, P. K. Patel, D. W. Price, S. Hatchett, M. H. Key, C. Andersen, R. Snavelly, and R. R. Freeman. Enhancement of proton acceleration by hot-electron recirculation in thin foils irradiated by ultraintense laser pulses. *Physical Review Letters*, 88(21):215006, 2002.
- [105] J. E. Crow, P. L. Auer, and J. E. Allen. The expansion of a plasma into a vacuum. *Journal of Plasma Physics*, 14(1):65–76, 1975.
- [106] A. J. Mackinnon, M. Borghesi, S. Hatchett, M. H. Key, P. K. Patel, H. Campbell, A. Schiavi, R. Snavelly, S. C. Wilks, and O. Willi. Effect of plasma scale length on multi-MeV proton production by intense laser pulses. *Physical Review Letters*, 86(9):1769, 2001.
- [107] M. Allen, Y. Sentoku, P. Audebert, A. Blazevic, T. Cowan, J. Fuchs, J. C. Gauthier, M. Geissel, M. Hegelich, S. Karsch, E. Morse, P. K. Patel, and M. Roth. Proton spectra from ultraintense laser-plasma interaction with thin foils: Experiments, theory, and simulation. *Physics of Plasmas*, 10(8):3283–3289, 2003.
- [108] L. Robson, P. T. Simpson, R. J. Clarke, K. W. D. Ledingham, F. Lindau, O. Lundh, T. McCanny, P. Mora, D. Neely, C.-G. Wahlström, M. Zepf, and P. McKenna. Scaling of proton acceleration driven by petawatt-laser-plasma interactions. *Nature Physics*, 3:58–62, 2007.
- [109] J. Denavit. Collisionless plasma expansion into a vacuum. *The Physics of Fluids*, 22(7):1384–1392, 1979.
- [110] A. V. Gurevich, L. V. Pariiskaya, and L. P. Pitaevskii. Self-similar motion of rarefied plasma. *Soviet Journal of Experimental and Theoretical Physics*, 22(2):449–454, 1966.
- [111] P. Mora and R. Pellat. Self-similar expansion of a plasma into a vacuum. *The Physics of Fluids*, 22(12):2300–2304, 1979.
- [112] P. Mora. Plasma expansion into a vacuum. *Physical Review Letters*, 90(18):185002, 2003.

-
- [113] J. S. Pearlman and R. L. Morse. Maximum expansion velocities of laser-produced plasmas. *Physical Review Letters*, 40(25):1652, 1978.
- [114] J. Fuchs, Y. Sentoku, E. d’Humières, T. E. Cowan, J. Cobble, P. Audebert, A. Kemp, A. Nikroo, P. Antici, E. Brambrink, A. Blazevic, E. M. Campbell, J. C. Fernández, J.-C. Gauthier, M. Geissel, M. Hegelich, S. Karsch, H. Popescu, N. Renard-LeGalloudec, M. Roth, J. Schreiber, R. Stephens, and H. Pépin. Comparative spectra and efficiencies of ions laser-accelerated forward from the front and rear surfaces of thin solid foils. *Physics of Plasmas*, 14(5):053105, 2007.
- [115] K. Zeil, S. D. Kraft, S. Bock, M. Bussmann, T. E. Cowan, T. Kluge, J. Metzkes, T. Richter, R. Sauerbrey, and U. Schramm. The scaling of proton energies in ultrashort pulse laser plasma acceleration. *New Journal of Physics*, 12(4):045015, 2010.
- [116] J. Schreiber, F. Bell, F. Grüner, U. Schramm, M. Geissler, M. Schnürer, S. Ter-Avetisyan, B. M. Hegelich, J. Cobble, E. Brambrink, J. Fuchs, P. Audebert, and D. Habs. Analytical model for ion acceleration by high-intensity laser pulses. *Physical Review Letters*, 97(4):045005, 2006.
- [117] M. Murakami and M. M. Basko. Self-similar expansion of finite-size non-quasi-neutral plasmas into vacuum: Relation to the problem of ion acceleration. *Physics of Plasmas*, 13(1):012105, 2006.
- [118] D. C. Carroll, O. Tresca, R. Prasad, L. Romagnani, P. S. Foster, P. Gallegos, S. Ter-Avetisyan, J. S. Green, M. J. V. Streeter, N. Dover, C. A. J. Palmer, C. M. Brenner, F. H. Cameron, K. E. Quinn, J. Schreiber, A. P. L. Robinson, T. Baeva, M. N. Quinn, X. H. Yuan, Z. Najmudin, M. Zepf, D. Neely, M. Borghesi, and P. McKenna. Carbon ion acceleration from thin foil targets irradiated by ultrahigh-contrast, ultraintense laser pulses. *New Journal of Physics*, 12(4):045020, 2010.
- [119] R. Prasad, A. A. Andreev, S. Ter-Avetisyan, D. Doria, K. E. Quinn, L. Romagnani, C. M. Brenner, D. C. Carroll, N. P. Dover, D. Neely, P. S. Foster, P. Gallegos, J. S. Green, P. McKenna, Z. Najmudin, C. A. J. Palmer, J. Schreiber, M. J. V. Streeter, O. Tresca, M. Zepf, and M. Borghesi. Fast ion acceleration from thin foils irradiated by ultra-high intensity, ultra-high contrast laser pulses. *Applied Physics Letters*, 99(12):121504, 2011.
- [120] B. Dromey, S. Kar, M. Zepf, and P. Foster. The plasma mirror—a subpicosecond optical switch for ultrahigh power lasers. *Review of Scientific Instruments*, 75(3):645–649, 2004.
- [121] G. Doumy, F. Quéré, O. Gobert, M. Perdrix, P. Martin, P. Audebert, J. C. Gauthier, J. P. Geindre, and T. Wittmann. Complete characterization of a plasma mirror for the production of high-contrast ultraintense laser pulses. *Physical Review E*, 69(2):026402, 2004.
- [122] A. Lévy, T. Ceccotti, P. D’Oliveira, F. Réau, M. Perdrix, F. Quéré, P. Monot, M. Bougeard, H. Lagarde, P. Martin, J.-P. Geindre, and P. Audebert. Double

- plasma mirror for ultrahigh temporal contrast ultraintense laser pulses. *Optics Letters*, 32(3):310–312, 2007.
- [123] M. Hornung, G. A. Becker, A. Seidel, J. Reislöhner, H. Liebetrau, L. Bock, S. Keppler, A. Kessler, M. Zepf, J. Hein, and M. C. Kaluza. Generation of 25-TW femtosecond laser pulses at 515 nm with extremely high temporal contrast. *Applied Sciences*, 5(4):1970–1979, 2015.
- [124] A. Macchi, S. Veghini, T. V. Liseykina, and F. Pegoraro. Radiation pressure acceleration of ultrathin foils. *New Journal of Physics*, 12(4):045013, 2010.
- [125] A. P. L. Robinson, P. Gibbon, M. Zepf, S. Kar, R. G. Evans, and C. Bellei. Relativistically correct hole-boring and ion acceleration by circularly polarized laser pulses. *Plasma Physics and Controlled Fusion*, 51(2):024004, 2009.
- [126] T. Schlegel, N. Naumova, V. T. Tikhonchuk, C. Labaune, I. V. Sokolov, and G. Mourou. Relativistic laser piston model: Ponderomotive ion acceleration in dense plasmas using ultraintense laser pulses. *Physics of Plasmas*, 16(8):083103, 2009.
- [127] C. A. J. Palmer, N. P. Dover, I. Pogorelsky, M. Babzien, G. I. Dudnikova, M. Ispiriyan, M. N. Polyanskiy, J. Schreiber, P. Shkolnikov, V. Yakimenko, and Z. Najmudin. Monoenergetic proton beams accelerated by a radiation pressure driven shock. *Physical Review Letters*, 106(1):014801, 2011.
- [128] A. Macchi, F. Cattani, T. V. Liseykina, and F. Cornolti. Laser acceleration of ion bunches at the front surface of overdense plasmas. *Physical Review Letters*, 94(16):165003, 2005.
- [129] V. A. Vshivkov, N. M. Naumova, F. Pegoraro, and S. V. Bulanov. Nonlinear electrodynamics of the interaction of ultra-intense laser pulses with a thin foil. *Physics of Plasmas*, 5(7):2727–2741, 1998.
- [130] X. Q. Yan, C. Lin, Z. M. Sheng, Z. Y. Guo, B. C. Liu, Y. R. Lu, J. X. Fang, and J. E. Chen. Generating high-current monoenergetic proton beams by a circularly polarized laser pulse in the phase-stable acceleration regime. *Physical Review Letters*, 100(13):135003, 2008.
- [131] T. Esirkepov, M. Yamagiwa, and T. Tajima. Laser ion-acceleration scaling laws seen in multiparametric particle-in-cell simulations. *Physical Review Letters*, 96(10):105001, 2006.
- [132] S. Zeisler. *Micromatter Technologies Inc., Private Communication*, 2020.
- [133] L. Yin, B. J. Albright, B. M. Hegelich, K. J. Bowers, K. A. Flippo, T. J. T. Kwan, and J. C. Fernández. Monoenergetic and GeV ion acceleration from the laser breakout afterburner using ultrathin targets. *Physics of Plasmas*, 14(5):056706, 2007.
- [134] L. Yin, B. J. Albright, D. Jung, R. C. Shah, S. Palaniyappan, K. J. Bowers, A. Henig, J. C. Fernández, and B. M. Hegelich. Break-out afterburner ion acceleration in the longer laser pulse length regime. *Physics of Plasmas*, 18(6):063103, 2011.

-
- [135] B. M. Hegelich, I. Pomerantz, L. Yin, H. C. Wu, D. Jung, B. J. Albright, D. C. Gautier, S. Letzring, S. Palaniyappan, R. Shah, K. Allinger, R. Hörlein, J. Schreiber, D. Habs, J. Blakeney, G. Dyer, L. Fuller, E. Gaul, E. Mccary, A. R. Meadows, C. Wang, T. Ditmire, and J. C. Fernandez. Laser-driven ion acceleration from relativistically transparent nanotargets. *New Journal of Physics*, 15(8):085015, 2013.
- [136] G. M. Petrov, C. McGuffey, A. G. R. Thomas, K. Krushelnick, and F. N. Beg. Heavy ion acceleration in the radiation pressure acceleration and breakout afterburner regimes. *Plasma Physics and Controlled Fusion*, 59(7):075003, 2017.
- [137] J. M. Dawson. Particle simulation of plasmas. *Reviews of Modern Physics*, 55(2):403, 1983.
- [138] C. K. Birdsall and A. B. Langdon. *Plasma Physics via Computer Simulation*. IOP Publishing, 1991.
- [139] K. Bennett, C. Brady, H. Schmitz, C. Ridgers, T. Arber, R. Evans, and T. Bell. *Developers Manual for the EPOCH PIC codes*. University of Warwick, 2013.
- [140] T. D. Arber, K. Bennett, C. S. Brady, A. Lawrence-Douglas, M. G. Ramsay, N. J. Sircombe, P. Gillies, R. G. Evans, H. Schmitz, A. R. Bell, and C. P. Ridgers. Contemporary particle-in-cell approach to laser-plasma modelling. *Plasma Physics and Controlled Fusion*, 57(11):113001, 2015.
- [141] M. Ramsay. *Short-Pulse Laser Interactions with High Density Plasma*. PhD thesis, University of Warwick, 2015.
- [142] K. Yee. Numerical solution of initial boundary value problems involving Maxwell’s equations in isotropic media. *IEEE Transactions on antennas and propagation*, 14(3):302–307, 1966.
- [143] H. Qin, S. Zhang, J. Xiao, J. Liu, Y. Sun, and W. M. Tang. Why is Boris algorithm so good? *Physics of Plasmas*, 20(8):084503, 2013.
- [144] T. Z. Esirkepov. Exact charge conservation scheme for particle-in-cell simulation with an arbitrary form-factor. *Computer Physics Communications*, 135(2):144–153, 2001.
- [145] J. Villasenor and O. Buneman. Rigorous charge conservation for local electromagnetic field solvers. *Computer Physics Communications*, 69(2-3):306–316, 1992.
- [146] R. Ramis, K. Eidmann, J. Meyer-ter Vehn, and S. Hüller. MULTI-fs—a computer code for laser–plasma interaction in the femtosecond regime. *Computer Physics Communications*, 183(3):637–655, 2012.
- [147] C. G. Freeman, G. Fiksel, C. Stoeckl, N. Sinenian, M. J. Canfield, G. B. Graeper, A. T. Lombardo, C. R. Stillman, S. J. Padalino, C. Mileham, T. C. Sangster, and J. A. Frenje. Calibration of a Thomson parabola ion spectrometer and Fujifilm imaging plate detectors for protons, deuterons, and alpha particles. *Review of Scientific Instruments*, 82(7):073301, 2011.

- [148] K. Harres, M. Schollmeier, E. Brambrink, P. Audebert, A. Blažević, K. Flippo, D. C. Gautier, M. Geißel, B. M. Hegelich, F. Nürnberg, J. Schreiber, H. Wahl, and M. Roth. Development and calibration of a Thomson parabola with microchannel plate for the detection of laser-accelerated MeV ions. *Review of Scientific Instruments*, 79(9):093306, 2008.
- [149] D. Jung, R. Hörlein, D. Kiefer, S. Letzring, D. C. Gautier, U. Schramm, C. Hübsch, R. Öhm, B. J. Albright, J. C. Fernandez, D. Habs, and B. M. Hegelich. Development of a high resolution and high dispersion Thomson parabola. *Review of Scientific Instruments*, 82(1):013306, 2011.
- [150] I. W. Choi, C. M. Kim, J. H. Sung, T. J. Yu, S. K. Lee, I. J. Kim, Y.-Y. Jin, T. M. Jeong, N. Hafz, K. H. Pae, Y.-C. Noh, D.-K. Ko, A. Yogo, A. S. Pirozhkov, K. Ogura, S. Orimo, A. Sagisaka, M. Nishiuchi, I. Daito, Y. Oishi, Y. Iwashita, S. Nakamura, K. Nemoto, A. Noda, H. Daido, and J. Lee. Ion spectrometer composed of time-of-flight and Thomson parabola spectrometers for simultaneous characterization of laser-driven ions. *Review of Scientific Instruments*, 80(5):053302, 2009.
- [151] J. Heymann. *Entwicklung und Charakterisierung eines Ionen-Spektrometers für relativistische Laser-Plasma-Experimente*. Diplomarbeit, Friedrich-Schiller-Universität Jena, 2009.
- [152] J. N. Olsen, G. W. Kuswa, and E. D. Jones. Ion-expansion energy spectra correlated to laser plasma parameters. *Journal of Applied Physics*, 44(5):2275–2283, 1973.
- [153] N. Sinenian, M. J. Rosenberg, M. Manuel, S. C. McDuffee, D. T. Casey, A. B. Zylstra, H. G. Rinderknecht, M. G. Johnson, F. H. Séguin, J. A. Frenje, C. K. Li, and R. D. Petrasso. The response of CR-39 nuclear track detector to 1-9 MeV protons. *Review of Scientific Instruments*, 82(10):103303, 2011.
- [154] J. F. Ziegler, M. D. Ziegler, and J. P. Biersack. SRIM - the stopping and range of ions in matter (2010). *Nuclear Instruments and Methods in Physics Research Section B: Beam Interactions with Materials and Atoms*, 268(11):1818–1823, 2010.
- [155] R. Prasad, D. Doria, S. Ter-Avetisyan, P. S. Foster, K. E. Quinn, L. Romagnani, C. M. Brenner, J. S. Green, P. Gallegos, M. J. V. Streeter, D. C. Carroll, O. Tresca, N. Dover, C. A. J. Palmer, J. Schreiber, D. Neely, Z. Najmudin, P. McKenna, M. Zepf, and M. Borghesi. Calibration of Thomson parabola-MCP assembly for multi-MeV ion spectroscopy. *Nuclear Instruments and Methods in Physics Research Section A: Accelerators, Spectrometers, Detectors and Associated Equipment*, 623(2):712–715, 2010. 1rs International Conference on Frontiers in Diagnostics Technologies.
- [156] T. W. Jeong, P. K. Singh, C. Scullion, H. Ahmed, K. F. Kakolee, P. Hadjisolomou, A. Alejo, S. Kar, M. Borghesi, and S. Ter-Avetisyan. Experimental evaluation of the response of micro-channel plate detector to ions with 10s of MeV energies. *Review of Scientific Instruments*, 87(8):083301, 2016.

-
- [157] D. L. Smith, R. G. Polk, and T. G. Miller. Measurement of the response of several organic scintillators to electrons, protons and deuterons. *Nuclear Instruments and Methods*, 64(2):157–166, 1968.
- [158] N. P. Dover, M. Nishiuchi, H. Sakaki, M. A. Alkhimova, A. Y. Faenov, Y. Fukuda, H. Kiriyaama, A. Kon, K. Kondo, K. Nishitani, K. Ogura, T. A. Pikuz, A. S. Pirozhkov, A. Sagisaka, M. Kando, and K. Kondo. Scintillator-based transverse proton beam profiler for laser-plasma ion sources. *Review of Scientific Instruments*, 88(7):073304, 2017.
- [159] J. Metzkes, L. Karsch, S. D. Kraft, J. Pawelke, C. Richter, M. Schürer, M. Sobiella, N. Stiller, K. Zeil, and U. Schramm. A scintillator-based online detector for the angularly resolved measurement of laser-accelerated proton spectra. *Review of Scientific Instruments*, 83(12):123301, 2012.
- [160] J. Reislöhner. *Laser-basierte Protonenbeschleunigung mit ultradünnen Folien und ultrahochem Kontrast*. Master’s thesis, Friedrich-Schiller-Universität Jena, 2015.
- [161] F. Wagner, O. Deppert, C. Brabetz, P. Fiala, A. Kleinschmidt, P. Poth, V. A. Schanz, A. Tebartz, B. Zielbauer, M. Roth, T. Stöhlker, and V. Bagnoud. Maximum proton energy above 85 MeV from the relativistic interaction of laser pulses with micrometer thick CH₂ targets. *Physical Review Letters*, 116(20):205002, 2016.
- [162] N. P. Dover, C. A. J. Palmer, M. J. V. Streeter, H. Ahmed, B. Albertazzi, M. Borghesi, D. C. Carroll, J. Fuchs, R. Heathcote, P. Hilz, K. F. Kakolee, S. Kar, R. Kodama, A. Kon, D. A. MacLellan, P. McKenna, S. R. Nagel, D. Neely, M. M. Notley, M. Nakatsutsumi, R. Prasad, G. Scott, M. Tampo, M. Zepf, J. Schreiber, and Z. Najmudin. Buffered high charge spectrally-peaked proton beams in the relativistic-transparency regime. *New Journal of Physics*, 18(1):013038, 2016.
- [163] F. Dollar, C. Zулick, A. G. R. Thomas, V. Chvykov, J. Davis, G. Kalinchenko, T. Matsuoka, C. McGuffey, G. M. Petrov, L. Willingale, V. Yanovsky, A. Maksimchuk, and K. Krushelnick. Finite spot effects on radiation pressure acceleration from intense high-contrast laser interactions with thin targets. *Physical Review Letters*, 108(17):175005, 2012.
- [164] M. Nolte. *Charakterisierung expandierter ultradünner DLC-Folien für die Laser-Protonenbeschleunigung*. Bachelor’s thesis, Friedrich-Schiller-Universität Jena, 2020.
- [165] S. Keppler. *Private Communication*, 2020.
- [166] M. Zepf, E. L. Clark, K. Krushelnick, F. N. Beg, C. Escoda, A. E. Dangor, M. I. K. Santala, M. Tatarakis, I. F. Watts, P. A. Norreys, R. J. Clarke, J. R. Davies, M. A. Sinclair, R. D. Edwards, T. J. Goldsack, I. Spencer, and K. W. D. Ledingham. Fast particle generation and energy transport in laser-solid interactions. *Physics of Plasmas*, 8(5):2323–2330, 2001.
- [167] M. Zepf, E. L. Clark, F. N. Beg, R. J. Clarke, A. E. Dangor, A. Gopal,

- K. Krushelnick, P. A. Norreys, M. Tatarakis, U. Wagner, and M. S. Wei. Proton acceleration from high-intensity laser interactions with thin foil targets. *Physical Review Letters*, 90(6):064801, 2003.
- [168] Y. Murakami, Y. Kitagawa, Y. Sentoku, M. Mori, R. Kodama, K. A. Tanaka, K. Mima, and T. Yamanaka. Observation of proton rear emission and possible gigagauss scale magnetic fields from ultra-intense laser illuminated plastic target. *Physics of Plasmas*, 8(9):4138–4143, 2001.
- [169] J. Badziak, S. Jabłoński, P. Parys, M. Rosiński, J. Wołowski, A. Szydłowski, P. Antici, J. Fuchs, and A. Mancic. Ultraintense proton beams from laser-induced skin-layer ponderomotive acceleration. *Journal of Applied Physics*, 104(6):063310, 2008.
- [170] S. Gaillard, J. Fuchs, N. R.-L. Galloudec, and T. E. Cowan. Study of saturation of CR-39 nuclear track detectors at high ion fluence and of associated artifact patterns. *Review of Scientific Instruments*, 78(1):013304, 2007.
- [171] D. Jung, B. J. Albright, L. Yin, D. C. Gautier, R. Shah, S. Palaniyappan, S. Letzring, B. Dromey, H.-C. Wu, T. Shimada, R. P. Johnson, M. Roth, J. C. Fernandez, D. Habs, and B. M. Hegelich. Beam profiles of proton and carbon ions in the relativistic transparency regime. *New Journal of Physics*, 15(12):123035, 2013.
- [172] H. W. Powell, M. King, R. J. Gray, D. A. MacLellan, B. Gonzalez-Izquierdo, L. C. Stockhausen, G. Hicks, N. P. Dover, D. R. Rusby, D. C. Carroll, H. Padda, R. Torres, S. Kar, R. J. Clarke, I. O. Musgrave, Z. Najmudin, M. Borghesi, D. Neely, and P. McKenna. Proton acceleration enhanced by a plasma jet in expanding foils undergoing relativistic transparency. *New Journal of Physics*, 17(10):103033, 2015.
- [173] H. Padda, M. King, R. J. Gray, H. W. Powell, B. Gonzalez-Izquierdo, L. C. Stockhausen, R. Wilson, D. C. Carroll, R. J. Dance, D. A. MacLellan, X. H. Yuan, N. M. H. Butler, R. Capdessus, M. Borghesi, D. Neely, and P. McKenna. Intra-pulse transition between ion acceleration mechanisms in intense laser-foil interactions. *Physics of Plasmas*, 23(6):063116, 2016.
- [174] S. Kuschel, A. Blinne, S. Tietze, M. Yeung, A. Huebl, D. Hollatz, and G. Wittig. The open-source particle in cell postprocessor. 2018.
- [175] J. D. Hunter. Matplotlib: A 2D graphics environment. *Computing In Science & Engineering*, 9(3):90–95, 2007.
- [176] S. v. d. Walt, S. C. Colbert, and G. Varoquaux. The NumPy array: A structure for efficient numerical computation. *Computing in Science & Engineering*, 13(2):22–30, 2011.
- [177] F. Perez and B. E. Granger. IPython: A system for interactive scientific computing. *Computing in Science & Engineering*, 9(3):21–29, 2007.
- [178] A. Sgattoni, P. Londrillo, A. Macchi, and M. Passoni. Laser ion acceleration using a solid target coupled with a low-density layer. *Physical Review E*, 85(3):036405, 2012.

- [179] A. P. L. Robinson, P. Gibbon, S. M. Pfotenhauer, O. Jäckel, and J. Polz. Scaling of the proton density reduction scheme for the laser acceleration of proton beams with a narrow energy spread. *Plasma Physics and Controlled Fusion*, 51(2):024001, 2009.
- [180] A. P. L. Robinson and P. Gibbon. Production of proton beams with narrow-band energy spectra from laser-irradiated ultrathin foils. *Physical Review E*, 75(1):015401, 2007.
- [181] S. M. Pfotenhauer, O. Jäckel, A. Sachtleben, J. Polz, W. Ziegler, H.-P. Schlenvoigt, K.-U. Amthor, M. C. Kaluza, K. W. D. Ledingham, R. Sauerbrey, P. Gibbon, A. P. L. Robinson, and H. Schwoerer. Spectral shaping of laser generated proton beams. *New Journal of Physics*, 10(3):033034, 2008.
- [182] M. Schollmeier, K. Harres, F. Nürnberg, A. Blažević, P. Audebert, E. Brambrink, J. C. Fernández, K. A. Flippo, D. C. Gautier, M. Geißel, B. M. Hegelich, J. Schreiber, and M. Roth. Laser beam-profile impression and target thickness impact on laser-accelerated protons. *Physics of Plasmas*, 15(5):053101, 2008.
- [183] T. Paasch-Colberg, T. Sokollik, K. Gorling, U. Eichmann, S. Steinke, M. Schnürer, P. V. Nickles, A. Andreev, and W. Sandner. New method for laser driven ion acceleration with isolated, mass-limited targets. *Nuclear Instruments and Methods in Physics Research Section A: Accelerators, Spectrometers, Detectors and Associated Equipment*, 653(1):30–34, 2011.
- [184] T. Sokollik, T. Paasch-Colberg, K. Gorling, U. Eichmann, M. Schnürer, S. Steinke, P. V. Nickles, A. Andreev, and W. Sandner. Laser-driven ion acceleration using isolated mass-limited spheres. *New Journal of Physics*, 12(11):113013, 2010.
- [185] T. M. Ostermayr, D. Haffa, P. Hilz, V. Pauw, K. Allinger, K.-U. Bamberg, P. Böhl, C. Bömer, P. R. Bolton, F. Deutschmann, T. Ditmire, M. E. Donovan, G. Dyer, E. Gaul, J. Gordon, B. M. Hegelich, D. Kiefer, C. Klier, C. Kreuzer, M. Martinez, E. McCary, A. R. Meadows, N. Moschüring, T. Rösch, H. Ruhl, M. Spinks, C. Wagner, and J. Schreiber. Proton acceleration by irradiation of isolated spheres with an intense laser pulse. *Physical Review E*, 94(3):033208, 2016.
- [186] P. Hilz, T. M. Ostermayr, A. Huebl, V. Bagnoud, B. Borm, M. Bussmann, M. Gallei, J. Gebhard, D. Haffa, J. Hartmann, T. Kluge, F. H. Lindner, P. Neumayr, C. G. Schaefer, U. Schramm, P. G. Thirolf, T. F. Rösch, F. Wagner, B. Zielbauer, and J. Schreiber. Isolated proton bunch acceleration by a petawatt laser pulse. *Nature Communications*, 9:423, 2018.
- [187] S. Busch, M. Schnürer, M. Kalashnikov, H. Schönnagel, H. Stiel, P. V. Nickles, W. Sandner, S. Ter-Avetisyan, V. Karpov, and U. Vogt. Ion acceleration with ultrafast lasers. *Applied Physics Letters*, 82(19):3354–3356, 2003.
- [188] M. Schnürer, S. Ter-Avetisyan, S. Busch, E. Risse, M. P. Kalachnikov, W. Sandner, and P. V. Nickles. Ion acceleration with ultrafast laser driven water droplets. *Laser and Particle Beams*, 23(3):337–343, 2005.

- [189] S. Ter-Avetisyan, M. Schnürer, S. Busch, E. Risse, P. V. Nickles, and W. Sandner. Spectral dips in ion emission emerging from ultrashort laser-driven plasmas. *Physical Review Letters*, 93(15):155006, 2004.
- [190] S. Ter-Avetisyan, M. Schnürer, P. V. Nickles, M. Kalashnikov, E. Risse, T. Sokollik, W. Sandner, A. Andreev, and V. Tikhonchuk. Quasimonoeenergetic deuteron bursts produced by ultraintense laser pulses. *Physical Review Letters*, 96(14):145006, 2006.
- [191] J. Polz. *Laser proton acceleration from water micro-droplets and solid hydrogen targets*. PhD thesis, Friedrich-Schiller-Universität Jena, 2017.
- [192] A. Sävert. *Private Communication*, 2019.
- [193] J. Bierbach, C. Rödel, M. Yeung, B. Dromey, T. Hahn, A. G. Pour, S. Fuchs, A. E. Paz, S. Herzer, S. Kuschel, O. Jäckel, M. C. Kaluza, G. Pretzler, M. Zepf, and G. G. Paulus. Generation of 10 μ W relativistic surface high-harmonic radiation at a repetition rate of 10 Hz. *New Journal of Physics*, 14(6):065005, 2012.
- [194] M. Yeung, S. Rykovanov, J. Bierbach, L. Li, E. Eckner, S. Kuschel, A. Woldgeorgis, C. Rödel, A. Sävert, G. G. Paulus, M. Coughlan, B. Dromey, and M. Zepf. Experimental observation of attosecond control over relativistic electron bunches with two-colour fields. *Nature Photonics*, 11:32, 2017.
- [195] S. Kahaly, S. Monchocé, H. Vincenti, T. Dzelzainis, B. Dromey, M. Zepf, P. Martin, and F. Quéré. Direct observation of density-gradient effects in harmonic generation from plasma mirrors. *Physical Review Letters*, 110(17):175001, 2013.
- [196] T. Nakamura, S. Kato, H. Nagatomo, and K. Mima. Surface-magnetic-field and fast-electron current-layer formation by ultraintense laser irradiation. *Physical Review Letters*, 93(26):265002, 2004.
- [197] T. Nakamura, K. Mima, H. Sakagami, and T. Johzaki. Electron surface acceleration on a solid capillary target inner wall irradiated with ultraintense laser pulses. *Physics of Plasmas*, 14(5):053112, 2007.
- [198] Y. T. Li, X. H. Yuan, M. H. Xu, Z. Y. Zheng, Z. M. Sheng, M. Chen, Y. Y. Ma, W. X. Liang, Q. Z. Yu, Y. Zhang, F. Liu, Z. H. Wang, Z. Y. Wei, W. Zhao, Z. Jin, and J. Zhang. Observation of a fast electron beam emitted along the surface of a target irradiated by intense femtosecond laser pulses. *Physical Review Letters*, 96(16):165003, 2006.
- [199] J. Psikal, V. Tikhonchuk, J. Limpouch, and O. Klimo. Lateral hot electron transport and ion acceleration in femtosecond laser pulse interaction with thin foils. *Physics of Plasmas*, 244(1):022057, 2010.
- [200] W. Schumaker, N. Nakanii, C. McGuffey, C. Zulick, V. Chyvkov, F. Dollar, H. Habara, G. Kalintchenko, A. Maksimchuk, K. A. Tanaka, A. G. R. Thomas, V. Yanovsky, and K. Krushelnick. Ultrafast electron radiography of magnetic fields in high-intensity laser-solid interactions. *Physical Review Letters*, 110(1):015003, 2013.

-
- [201] C. A. J. Palmer, J. Schreiber, S. R. Nagel, N. P. Dover, C. Bellei, F. N. Beg, S. Bott, R. J. Clarke, A. E. Dangor, S. M. Hassan, P. Hilz, D. Jung, S. Kneip, S. P. D. Mangles, K. L. Lancaster, A. Rehman, A. P. L. Robinson, C. Spindloe, J. Szerypo, M. Tatarakis, M. Yeung, M. Zepf, and Z. Najmudin. Rayleigh-Taylor instability of an ultrathin foil accelerated by the radiation pressure of an intense laser. *Physical Review Letters*, 108(22):225002, 2012.
- [202] J. Metzkes, T. Kluge, K. Zeil, M. Bussmann, S. D. Kraft, T. E. Cowan, and U. Schramm. Experimental observation of transverse modulations in laser-driven proton beams. *New Journal of Physics*, 16(2):023008, 2014.
- [203] S. Göde, C. Rödel, K. Zeil, R. Mishra, M. Gauthier, F.-E. Brack, T. Kluge, M. J. MacDonald, J. Metzkes, L. Obst, M. Rehwald, C. Ruyer, H.-P. Schlenvoigt, W. Schumaker, P. Sommer, T. E. Cowan, U. Schramm, S. Glenzer, and F. Fiuza. Relativistic electron streaming instabilities modulate proton beams accelerated in laser-plasma interactions. *Physical Review Letters*, 118(19):194801, 2017.
- [204] G. G. Scott, C. M. Brenner, V. Bagnoud, R. J. Clarke, B. Gonzalez-Izquierdo, J. S. Green, R. I. Heathcote, H. W. Powell, D. R. Rusby, B. Zielbauer, P. McKenna, and D. Neely. Diagnosis of Weibel instability evolution in the rear surface density scale lengths of laser solid interactions via proton acceleration. *New Journal of Physics*, 19(4):043010, 2017.
- [205] N. L. Kugland, D. D. Ryutov, C. Plechaty, J. S. Ross, and H.-S. Park. Invited Article: Relation between electric and magnetic field structures and their proton-beam images. *Review of Scientific Instruments*, 83(10):101301, 2012.
- [206] L. Obst-Huebl, T. Ziegler, F.-E. Brack, J. Branco, M. Bussmann, T. E. Cowan, C. B. Curry, F. Fiuza, M. Garten, M. Gauthier, S. Göde, S. H. Glenzer, A. Huebl, A. Irman, J. B. Kim, T. Kluge, S. D. Kraft, F. Kroll, J. Metzkes-Ng, R. Pausch, I. Prencipe, M. Rehwald, C. Roedel, H.-P. Schlenvoigt, U. Schramm, and K. Zeil. All-optical structuring of laser-driven proton beam profiles. *Nature Communications*, 9:5292, 2018.
- [207] J. T. Morrison, S. Feister, K. D. Frische, D. R. Austin, G. K. Ngirmang, N. R. Murphy, C. Orban, E. A. Chowdhury, and W. M. Roquemore. MeV proton acceleration at kHz repetition rate from ultra-intense laser liquid interaction. *New Journal of Physics*, 20(2):022001, 2018.
- [208] F. Ronneberger. *Private Communication*, 2021.
- [209] P. Tournois. Acousto-optic programmable dispersive filter for adaptive compensation of group delay time dispersion in laser systems. *Optics Communications*, 140(3):245–249, 1997.
- [210] F. Verluise, V. Laude, Z. Cheng, Ch. Spielmann, and P. Tournois. Amplitude and phase control of ultrashort pulses by use of an acousto-optic programmable dispersive filter: pulse compression and shaping. *Optics Letters*, 25(8):575–577, 2000.
- [211] F. Druon, G. Chériaux, J. Faure, J. Nees, M. Nantel, A. Maksimchuk,

- G. Mourou, J. C. Chanteloup, and G. Vdovin. Wave-front correction of femtosecond terawatt lasers by deformable mirrors. *Optics Letters*, 23(13):1043–1045, 1998.
- [212] M. P. Kalashnikov, E. Risse, H. Schönnagel, and W. Sandner. Double chirped-pulse-amplification laser: a way to clean pulses temporally. *Optics Letters*, 30(8):923, 2005.
- [213] M. Hornung, R. Bödefeld, M. Siebold, A. Kessler, M. Schnepf, R. Wachs, A. Sävert, S. Podleska, S. Keppler, J. Hein, and M. C. Kaluza. Temporal pulse control of a multi-10 TW diode-pumped Yb:Glass laser. *Applied Physics B*, 101:93–102, 2010.
- [214] H. Liebetrau, M. Hornung, A. Seidel, M. Hellwing, A. Kessler, S. Keppler, F. Schorcht, J. Hein, and M. C. Kaluza. Ultra-high contrast frontend for high peak power fs-lasers at 1030 nm. *Optics Express*, 22(20):24776, 2014.
- [215] H. Liebetrau, M. Hornung, S. Keppler, M. Hellwing, A. Kessler, F. Schorcht, J. Hein, and M. C. Kaluza. High contrast, 86 fs, 35 mJ pulses from a diode-pumped, Yb:glass, double-chirped-pulse amplification laser system. *Optics Letters*, 41(13):3006–3009, 2016.
- [216] H. Liebetrau, M. Hornung, S. Keppler, M. Hellwing, A. Kessler, F. Schorcht, J. Hein, and M. C. Kaluza. Intracavity stretcher for chirped-pulse amplification in high-power laser systems. *Optics Letters*, 42(2):326–329, 2017.
- [217] C. Wandt, S. Klingebiel, S. Keppler, M. Hornung, M. Loeser, M. Siebold, C. Skrobol, A. Kessel, S. A. Trushin, Z. Major, J. Hein, M. C. Kaluza, F. Krausz, and S. Karsch. Development of a Joule-class Yb:YAG amplifier and its implementation in a CPA system generating 1 TW pulses. *Laser & Photonics Reviews*, 8(6):875–881, 2014.
- [218] A. Kessler, M. Hornung, S. Keppler, F. Schorcht, M. Hellwing, H. Liebetrau, J. Körner, A. Sävert, M. Siebold, M. Schnepf, J. Hein, and M. C. Kaluza. 16.6 J chirped femtosecond laser pulses from a diode-pumped Yb : CaF₂ amplifier. *Optics Letters*, 39(6):1333, 2014.
- [219] M. Hornung, R. Bödefeld, M. Siebold, M. Schnepf, J. Hein, R. Sauerbrey, and M. C. Kaluza. Alignment of a tiled-grating compressor in a high-power chirped-pulse amplification laser system. *Applied Optics*, 46(30):7432, 2007.
- [220] O. Jäckel. *Characterization of ion acceleration with relativistic laser-plasma*. PhD thesis, Friedrich-Schiller-Universität Jena, 2009.
- [221] O. Jäckel. *Vermessung von Ionenspektren aus relativistischen laserproduzierten Plasmen*. Diplomarbeit, Friedrich-Schiller-Universität Jena, 2006.

Publications

1. G. A. Becker, S. Tietze, S. Keppler, J. Reislöhner, J. H. Bin, L. Bock, F. E. Brack, J. Hein, M. Hellwing, P. Hinz, M. Hornung, A. Kessler, S. Kraft, S. Kuschel, H. Liebetrau, W. Ma, J. Polz, H.-P. Schlenvoigt, F. Schorcht, M. B. Schwab, A. Seidel, K. Zeil, U. Schramm, M. Zepf, J. Schreiber, S. Rykovanov, and M. C. Kaluza. Ring-like spatial distribution of laser accelerated protons in the ultra-high-contrast TNSA-regime. *Plasma Physics and Controlled Fusion*, 60(5):055010, 2018.
2. G. A. Becker, M. B. Schwab, R. Löttsch, S. Tietze, D. Klöpfel, M. Rehwald, H.-P. Schlenvoigt, A. Sävert, U. Schramm, M. Zepf, and M. C. Kaluza, Characterization of laser-driven proton acceleration from water microdroplets. *Scientific Reports*, 9:17169, 2019.
3. M. Hornung, H. Liebetrau, A. Seidel, S. Keppler, A. Kessler, J. Körner, M. Hellwing, F. Schorcht, D. Klöpfel, A. K. Arunachalam, G. A. Becker, A. Sävert, J. Polz, J. Hein, and M. C. Kaluza. The all-diode-pumped laser system POLARIS – an experimentalist’s tool generating ultra-high contrast pulses with high energy. *High Power Laser Science and Engineering*, 2, 2014.
4. M. Hornung, G. A. Becker, A. Seidel, J. Reislöhner, H. Liebetrau, L. Bock, S. Keppler, A. Kessler, M. Zepf, J. Hein, and M. C. Kaluza. Generation of 25-TW femtosecond laser pulses at 515 nm with extremely high temporal contrast. *Applied Sciences*, 5(4):1970–1979, 2015.
5. M. Hornung, H. Liebetrau, S. Keppler, A. Kessler, M. Hellwing, F. Schorcht, G. A. Becker, M. Reuter, J. Polz, J. Körner, J. Hein, and M. C. Kaluza. 54 J pulses with 18 nm bandwidth from a diode-pumped chirped-pulse amplification laser system. *Optics Letters*, 41(22):5413, 2016.

-
6. J. Polz, A. P. L. Robinson, A. Kalinin, G. A. Becker, R. A. Costa Fraga, M. Hellwing, M. Hornung, S. Keppler, A. Kessler, D. Klöpfel, H. Liebetrau, F. Schorcht, J. Hein, M. Zepf, R. E. Grisenti, and M. C. Kaluza. Efficient laser-driven proton acceleration from a cryogenic solid hydrogen target. *Scientific Reports*, 9:16534, 2019.
 7. S. Keppler, N. Elkina, G. A. Becker, J. Hein, M. Hornung, M. Mäusezahl, C. Rödel, I. Tamer, M. Zepf, and M. C. Kaluza. Intensity scaling limitations of laser-driven proton acceleration in the TNSA-regime. under revision.

Danksagung

Die Umsetzung dieser Arbeit wäre durch die Unterstützung meiner Kollegen, Freunde und meiner Familie nicht möglich gewesen. Besonders bedanken möchte ich mich hier bei:

- Prof. Dr. Malte C. Kaluza für die Vergabe des Themas und die fachliche Unterstützung während meiner Zeit als Doktorand in seiner Arbeitsgruppe. Besonders seine aufmunternde Art hat mir geholfen diese Dissertation fertigzustellen.
- Matt Schwab, der auch seit vielen Jahren mein Bürogenosse ist, und mit dem ich viele fachliche und aufbauende Gespräche geführt habe. Ohne seine Unterstützung und diejenige Robert Lötzschs wäre das Tropfenexperiment nicht möglich gewesen.
- Marco Hornung, Issa Tamer, Sebastian Keppler und Yasmina Azamoum für die entspannte und gute Zusammenarbeit am POLARIS unter anderem beim Experiment mit dem Plasmaspiegel und viele spannende Diskussionen über die Physik und das restliche Leben.
- Diethard Klöpfel für die vielen tiefgründigen Gespräche über die Arbeit und die Welt und besonders für seine schnelle Unterstützung bei technischen Notfällen, besonders beim Tropfenexperiment.
- Stefan Tietze für das Durchführen aller Simulationen, die ich für die Interpretation des Tropfenexperiments und der Erklärung des ringförmigen Strahlprofils benötigte.
- Frank Schorcht, Marco Hellwing, Alexander Kessler für die gute Zusammenarbeit am POLARIS.
- Burgard Beleites und Falk Ronneberger, welche den JETI 40 während des Tröpfchenexperiments betreut haben. Dazu Wolfgang Ziegler für technische Unterstützung am Anfang meiner Promotion und den Mitgliedern der Werkstätten für die Herstellung verschiedener Sonderwünsche.

- Jan Reislöhner und Andreas Seidel für ihre Mitarbeit am Experiment mit SHG am POLARIS.
- Allen anderen aktuellen und ehemaligen Mitgliedern der Arbeitsgruppe, Jens Polz, Joachim Hein, Sophie Schmidt, Hartmut Liebetrau, Carola Zepter, Alexander Sävert, Jörg Körner, Max Mäusezahl, Maria Reuter und allen die ich vergessen habe namentlich zu erwähnen für eine tolle Zeit am Institut.
- Bedanken möchte ich mich auch bei den Kollegen vom HZDR Dresden und der LMU München, die bei dem Tropfenexperiment am JETI 40 und dem Experiment mit SHG am POLARIS mitgearbeitet haben.

Ein besonderer Dank gilt natürlich meiner Familie, insbesondere meiner Mutter und meiner Schwester, die mich immer unterstützt haben. Außerdem wäre die Promotion nicht ohne die moralische Unterstützung meiner Freunde möglich gewesen, deshalb möchte ich mich hier noch besonders bedanken bei Familie (J.Vorpapel)⁴, Jan, Daniel, Dennis, Thomas, Benedikt und Steve.

Außerdem möchte ich allen Danken, die mich unterstützt haben, deren Namen ich beim Schreiben dieser Zeilen aber vergessen habe zu erwähnen.

Ehrenwörtliche Erklärung

Ich erkläre hiermit ehrenwörtlich, dass ich die vorliegende Arbeit selbstständig, ohne unzulässige Hilfe Dritter und ohne Benutzung anderer als der angegebenen Hilfsmittel und Literatur angefertigt habe. Die aus anderen Quellen direkt oder indirekt übernommenen Daten und Konzepte sind unter Angabe der Quelle gekennzeichnet. Bei der Auswahl und Auswertung folgenden Materials haben mir die nachstehend aufgeführten Personen in der jeweils beschriebenen Weise unentgeltlich geholfen:

1. Stefan Tietze – Durchführung der Simulationen mit EPOCH (siehe Abschnitt 3.4.2 und Abschnitt 4.4)

Weitere Personen waren an der inhaltlich-materiellen Erstellung der vorliegenden Arbeit nicht beteiligt. Insbesondere habe ich hierfür nicht die entgeltliche Hilfe von Vermittlungs- bzw. Beratungsdiensten (Promotionsberater oder andere Personen) in Anspruch genommen. Niemand hat von mir unmittelbar oder mittelbar geldwerte Leistungen für Arbeiten erhalten, die im Zusammenhang mit dem Inhalt der vorgelegten Dissertation stehen.

Die Arbeit wurde bisher weder im In- noch im Ausland in gleicher oder ähnlicher Form einer anderen Prüfungsbehörde vorgelegt.

Die geltende Promotionsordnung der Physikalisch-Astronomischen Fakultät ist mir bekannt.

Ich versichere ehrenwörtlich, dass ich nach bestem Wissen die reine Wahrheit gesagt und nichts verschwiegen habe.

Ort, Datum

Unterschrift d. Verfassers